

# Image Cover Sheet

**CLASSIFICATION**

UNCLASSIFIED

**SYSTEM NUMBER**

498485

**TITLE**

Wind Tunnel Investigation and Analysis of the DREV - ISL Reference  
Projectiles

**System Number:****Patron Number:****Requester:****Notes:****DSIS Use only:****Deliver to:** FF



Report Documentation Page			Form Approved OMB No. 0704-0188		
Public reporting burden for the collection of information is estimated to average 1 hour per response, including the time for reviewing instructions, searching existing data sources, gathering and maintaining the data needed, and completing and reviewing the collection of information. Send comments regarding this burden estimate or any other aspect of this collection of information, including suggestions for reducing this burden, to Washington Headquarters Services, Directorate for Information Operations and Reports, 1215 Jefferson Davis Highway, Suite 1204, Arlington VA 22202-4302. Respondents should be aware that notwithstanding any other provision of law, no person shall be subject to a penalty for failing to comply with a collection of information if it does not display a currently valid OMB control number.					
1. REPORT DATE <b>JUN 1996</b>		2. REPORT TYPE		3. DATES COVERED	
4. TITLE AND SUBTITLE <b>Wind Tunnel Investigation and Analysis of the DREV-ISL Reference Projectiles</b>			5a. CONTRACT NUMBER		
			5b. GRANT NUMBER		
			5c. PROGRAM ELEMENT NUMBER		
6. AUTHOR(S)			5d. PROJECT NUMBER		
			5e. TASK NUMBER		
			5f. WORK UNIT NUMBER		
7. PERFORMING ORGANIZATION NAME(S) AND ADDRESS(ES) <b>Defence R&amp;D Canada - Valcartier, 2459 Pie-XI Blvd North, Quebec (Quebec) G3J 1X5 Canada, ,</b>			8. PERFORMING ORGANIZATION REPORT NUMBER		
9. SPONSORING/MONITORING AGENCY NAME(S) AND ADDRESS(ES)			10. SPONSOR/MONITOR'S ACRONYM(S)		
			11. SPONSOR/MONITOR'S REPORT NUMBER(S)		
12. DISTRIBUTION/AVAILABILITY STATEMENT <b>Approved for public release; distribution unlimited.</b>					
13. SUPPLEMENTARY NOTES					
14. ABSTRACT <b>A comprehensive wind tunnel investigation on a cone-cylinder body with and without fins was conducted over a Mach number range of 2 to 4. The tests were conducted as a function of angle of attack varying from -5° to +15° at different roll orientations. The experimental programme consisted of flow visualization, aerodynamic force and moments, static pressure and flow velocity measurements taken in the DREV indraft wind tunnel. The wind tunnel had an up stream sting support system to conduct interference-free base pressure measurements. The surface and base pressure results are compared with similar tests that were conducted at the French-German Research Institute 'of Saint Louis (ISL), and the reduced aerodynamic coefficients are compared with estimated values from Projectile Design and Analysis System (PRODAS). Some differences were noticed between the results from the two wind tunnels and most of these were accounted for from the different boundary layer thicknesses.</b>					
15. SUBJECT TERMS					
16. SECURITY CLASSIFICATION OF:			17. LIMITATION OF ABSTRACT	18. NUMBER OF PAGES <b>102</b>	19a. NAME OF RESPONSIBLE PERSON
a. REPORT <b>unclassified</b>	b. ABSTRACT <b>unclassified</b>	c. THIS PAGE <b>unclassified</b>			

UNCLASSIFIED

DEFENCE RESEARCH ESTABLISHMENT  
CENTRE DE RECHERCHES POUR LA DÉFENSE  
VALCARTIER, QUÉBEC

DREV - R - 9520

Unlimited Distribution/Distribution illimitée

WIND TUNNEL INVESTIGATION AND ANALYSIS  
OF THE DREV - ISL REFERENCE PROJECTILES

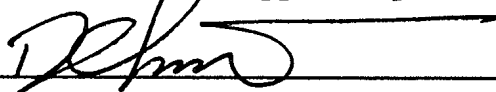
by

C. Berner\* and A. D. Dupuis

June/juin 1996

\* Institut franco-allemand de recherches de St- Louis (ISL)

Approved by / approuvé par



Chief Scientist / Scientifique en chef

22 Apr '96

Date

SANS CLASSIFICATION



## UNCLASSIFIED

i

ABSTRACT

A comprehensive wind tunnel investigation on a cone-cylinder body with and without fins was conducted over a Mach number range of 2 to 4. The tests were conducted as a function of angle of attack varying from  $-5^\circ$  to  $+15^\circ$  at different roll orientations. The experimental programme consisted of flow visualization, aerodynamic force and moments, static pressure and flow velocity measurements taken in the DREV indraft wind tunnel. The wind tunnel had an up stream sting support system to conduct interference-free base pressure measurements. The surface and base pressure results are compared with similar tests that were conducted at the French-German Research Institute of Saint Louis (ISL), and the reduced aerodynamic coefficients are compared with estimated values from Projectile Design and Analysis System (PRODAS). Some differences were noticed between the results from the two wind tunnels and most of these were accounted for from the different boundary layer thicknesses.

RÉSUMÉ

Des essais en soufflerie ont été menés autour d'un projectile cône-cylindre avec et sans empennages. Les essais ont été effectués dans une plage de Mach 2 à 4 pour des angles d'attaque compris entre  $-5^\circ$  et  $15^\circ$  et pour différentes positions en roulis des ailettes. Les résultats expérimentaux consistent en des visualisations, des mesures de pression statique, de vitesse et de force et moment. Pour éviter toute perturbation par des supports latéraux, un montage type "dard-amont" a été utilisé pour l'étude des écoulements de culot. Les résultats obtenus ont été comparés à ceux obtenus pour des configurations et dans des conditions similaires à l'Institut franco-allemand de recherches de Saint-Louis (ISL). Les coefficients aérodynamiques sont comparés à des valeurs obtenues empiriquement au moyen du code PRODAS (Projectile Design and Analysis System). Les écarts entre les deux souffleries peuvent être imputés à la différence d'épaisseur physique de la couche limite.



UNCLASSIFIED  
iii

TABLE OF CONTENTS

ABSTRACT/RÉSUMÉ .....i

EXECUTIVE SUMMARY.....v

NOMENCLATURE.....vii

1.0 INTRODUCTION .....1

2.0 EXPERIMENTAL METHOD .....2

    2.1 Wind Tunnel.....2

    2.2 DREV/ISL Reference Configurations.....3

    2.3 Experimental Technique .....3

    2.4 Instrumentation .....5

    2.5 Data Acquisition and Data Reduction.....5

3.0 RESULTS.....9

    3.1 Boundary Layer Profiles .....10

    3.2 Reference Projectile A (without Fins).....11

    3.3 Reference Projectile B (with Fins).....16

4.0 CONCLUSIONS .....22

5.0 ACKNOWLEDGMENTS.....24

6.0 REFERENCES .....25

TABLES I to V

FIGURES 1 to 42





## UNCLASSIFIED

v

EXECUTIVE SUMMARY

Many options are being examined to improve the performance of existing weapon systems. For example, increasing the range of artillery shells by reducing the base drag with novel passive means and the possibility of giving them some maneuverability on the battlefield to enhance the hit probability on selected high threat targets could be a great advantage to the Canadian Forces. The use of lateral jets on missiles could increase their performance over classical aerodynamic control surfaces and could be used to provide mid-course trajectory corrections for direct-fire weapons. Novel systems, for example tandem kinetic energy projectiles, to defeat active armour of future tanks are being studied actively. The available information on how such modifications would improve the aerodynamic performance over the classical projectile or missile shapes is rather limited.

However, before characterizing the interactions between two or more projectiles or the effect of lateral jets, or cavity shapes to house these jets and novel means to reduce the drag of artillery-type shells, it is necessary to provide detailed and reliable information on reference test cases so as to be able to quantify any improvements over the classical projectile.

The objective of the present investigation was to determine, by careful experiments in wind tunnel facilities, the full aerodynamic characteristics of two reference projectiles in order to establish a well-documented and reliable data base. These test cases could then be used for the validation of three-dimensional Navier-Stokes codes, empirical predictions for future studies of novel projectile configurations or ones with lateral jets as a controlling option.

The experiments consisted of flow visualization, static surface and base pressure measurements, aerodynamic force and moment coefficients, as well as velocity measurements on the reference models. The reference projectiles consisted of a simple cone-cylinder with and without fins with a length-to-diameter ratio of 6. Surface and base pressure measurements were compared with the results obtained with the ISL supersonic wind tunnel. Empirical predictions from PRODAS (Projectile Design and Analysis System) were also compared with the reduced experimental aerodynamic coefficients.

With this comprehensive aerodynamic data base of classical projectile shapes, many studies can be conducted to test new technologies, methodologies or applications to improve the performance and capability of many weapon systems. It has been demonstrated that future efforts can be concentrated on testing and evaluating the weapons themselves without the need for more measurements of test cases.



## UNCLASSIFIED

vii

NOMENCLATURE

A	Axial force
$A_i$	Polynomial coefficient
a	Distance between the point of application of the balance forward normal force $N_1$ and BRC, m
BRC	Balance reference center, m
b	Distance between the point of application of the balance aft normal force $N_2$ and BRC, m
CA	Axial force coefficient
CA0	Axial force coefficient slope (at $\alpha = 0^\circ$ )
CDF	Forebody drag coefficient
CDT	Total drag coefficient
CL	Lift coefficient
CM	Pitching moment coefficient about MRC
CMA	Pitching moment coefficient slope (at $\alpha = 0^\circ$ ), $\text{rad}^{-1}$
CN	Normal force coefficient
CNA	Normal force coefficient slope (at $\alpha = 0^\circ$ ), $\text{rad}^{-1}$
$C_r$	Crocco number
CY	Side force coefficient
CYM	Yawing moment coefficient about MRC
D, d	Diameter of maximum cross section or caliber
$D_b, d_b$	Base diameter, m
H	Boundary layer shape factor
l	Projectile length, m
M	Nominal free stream Mach number
$M_i$	Measured Mach number at the $i^{\text{th}}$ balance reading
MRC	Moment reference center, located at the model base
N	Total normal force, N
$P_\infty$	Free stream static pressure ( $= P_{\text{inf}}$ ), Pa
$P_b$	Base pressure measured with the $i^{\text{th}}$ transducer, Pa
$P_{\text{base}}$	Base pressure with respect to wall pressure
$P_i$	Pressure measured with the $i^{\text{th}}$ transducer, Pa
$P_a$	Static pressure in the test section, Pa
$P_t$	Average total pressure, Pa

## UNCLASSIFIED

viii

$P_{ti}$	Total pressure measured in the settling chamber at the time of the $i^{th}$ balance reading, Pa
$P_{vi}$	Test section static pressure measured on wall at the time of the $i^{th}$ balance reading, Pa
$Q$	Test section dynamic pressure, Pa
$r$	Base radius, m
$Re$	Reynolds number per unit length, $m^{-1}$
$Re_d$	Reynolds number based on model diameter
$Re_l$	Reynolds number based on model length
$S$	Body cross-sectional area, $= \pi d^2 / 4$ , $m^2$
$S_b$	Body base area, $= \pi d_b^2 / 4$ , $m^2$
$T_a$	Reservoir air temperature, $^{\circ}K$
$T_v$	Test section temperature, $^{\circ}K$
$\bar{u}$	Mean stream wise velocity component (bar can be omitted), m/s
$U_{\infty}$	Free stream velocity ( $= U_{inf}$ ), m/s
$x$	Distance along the afterbody axis, m
XCP	Position of center of pressure aft of MRC, in calibres
XCP0	Position of center of pressure aft of MRC at $\alpha = 0$ , in calibres
$y$	Distance from center of model axis, m
$Y$	Total side force, N
$\alpha$	Angle of attack, deg
$\delta$	Initial turbulent boundary layer thickness, m
$\delta_1$	Boundary layer displacement thickness, m
$\delta_2$	Boundary layer displacement thickness, m
$\gamma$	Specific heat ratio
$\mu$	Air viscosity in test section, Pa·s
$\rho$	Air density in test section, $kg/m^3$
$\rho_{\infty}$	Free stream density, $kg/m^3$
$\varphi$	Roll angle of top fin away from the vertical, positive clockwise looking from the rear, deg
$\phi$	Circumferential static pressure tap position from the top fin, positive clockwise looking from the rear, deg

UNCLASSIFIED

1

## 1.0 INTRODUCTION

DREV (Defence Research Establishment Valcartier (DREV) in Quebec, Canada, and the French-German Research Institute (ISL), in Saint-Louis, France, agreed, under the auspices of Theme 25 of the Franco-Canadian Accord, to conduct an extensive experimental and computational investigation on two reference projectiles. Both research establishments have wind tunnels, aeroballistic range facilities and computational fluid dynamic (CFD) means to determine the aerodynamic characteristics and the stability of any projectile configuration. The aim was to use a triangular exploration (wind tunnel, free-flight and computational) to evaluate each of the different methodologies and compare them in order to try and reduce as much as possible the number of required aerodynamic tests, which tend to be quite expensive. Also, once this initial study is completed, any further collaborative projects between the two establishments would be more complementary rather than duplicative.

Many options are being examined by both research establishments to improve the performance of existing weapon systems. For example, increasing the range of artillery shells by reducing the base drag with novel passive means and the possibility of giving them some maneuverability on the battlefield to enhance the hit probability on selected high threat targets could be a great advantage. The use of lateral jets on missiles could increase their performance over classical aerodynamic control surfaces and could be used to provide mid-course trajectory corrections for direct-fire weapons. Novel systems, for example tandem kinetic energy projectiles, to defeat the active armour of future tanks are being studied actively. The available information on how such modifications would ameliorate the aerodynamic performance over the classical projectile or missile shapes is rather limited. Before characterizing the interactions between two or more projectiles or the effect of lateral jets, or cavity shapes to house these jets and novel means to reduce the drag of artillery-type shells, it is necessary to provide detailed and reliable information on reference test cases so as to be able to quantify any improvements over the classical projectile.

The objective of the present investigation was to determine, by careful experiments in the DREV and ISL wind tunnel facilities, the full aerodynamic

UNCLASSIFIED

2

characteristics of two reference projectiles in order to establish a well-documented data base. These test cases could then be used for the validation of three-dimensional Navier-Stokes codes and empirical predictions tools.

The wind tunnel experiments consisted of flow visualization, static surface and base pressure measurements, aerodynamic force and moment coefficients, as well as velocity measurements on the reference models. The reference projectiles consisted of a simple cone-cylinder with and without fins with a length-to-diameter ratio of 6. Surface and base pressure measurements were compared with results obtained with the ISL supersonic wind tunnel. Empirical predictions from PRODAS (Projectile Design and Analysis System) were also compared with the reduced experimental aerodynamic coefficients.

Details of the ISL wind tunnel tests, free-flight experiments and numerical simulation results are provided respectively in Refs. 1 - 4 for the same configurations tested in this report.

This study was conducted as part of a cooperative research program between DREV and ISL under the auspices of Theme 25 - Aeroballistics of the French-Canadian Accord. This work was performed at DREV between 1990 and 1994 under PSC 31D, Weapon Systems.

## 2.0 EXPERIMENTAL METHOD

### 2.1 Wind Tunnel

Experiments were conducted in the DREV trisonic wind tunnel (Fig. 1). It is an indraft-type wind tunnel with a test section of 60 x 60 cm with a useful run time of about 6 s. Supersonic flow is achieved by using seven interchangeable nozzle blocks for  $M=1.5$ , 1.75, 2.0, 2.5, 3.0, 3.5 and 4.0. The Reynolds numbers for the tested Mach numbers are listed in Table I. The corresponding Reynolds numbers in the ISL supersonic wind tunnel and those that would be obtained in flight under standard sea level conditions are also given for comparison. The Reynolds numbers given are based on the length and on the diameter of the tested model.

UNCLASSIFIED

3

## 2.2 DREV/ISL Reference Configurations

The reference configurations chosen for this investigation were based on Ref. 5 and consisted of a cone-cylinder projectile without fins (Model A) and a cone-cylinder finned body (Model B). Photographs of the wind tunnel models are shown in Figs. 2a and 2b. The dimensions and characteristics of the models are presented in Figs. 3a and 3b. The models consisted of a two-calibre nose length followed by a four-calibre cylindrical length for a total  $l/d$  of 6. The finned model had the same cone-body as the previous configuration but four clipped delta fins were added to the base, as shown in Fig. 3b. The fin height was 0.5 cal with a length of 1.5 cal at the base. The fin had a conical leading edge of  $30^\circ$  and a thickness at the base of 0.085 cal. The nominal diameter of the wind tunnel models was 40 mm.

## 2.3 Experimental Technique

The experiments were divided into two test series:

- a) for the characterization of the flow around the forebody
  - with static pressure and aerodynamic force moment measurements on models mounted on a standard down stream sting (Fig. 4a)
- b) for the characterization of the afterbody flows
  - with static pressure and boundary layer profile measurements on models mounted on an up stream sting afterbody setup (Fig. 4b). This system was used to avoid disturbances over the base from usual support systems, i.e. down stream stings or struts. However, this type of setup can only be used at Mach numbers up to 2.5, since the dimensions of the nozzle throat become too small to accommodate the sting at the higher Mach numbers. Therefore measurements were only performed at Mach 2 and at  $0^\circ$  angle of attack. Special care, described in 3.1, was taken in



## UNCLASSIFIED

4

order to ensure that the boundary layers were turbulent and that their thicknesses were not too high.

The up stream system was designed with a boundary layer suction capability in an attempt to control the height, profile and type of boundary layer, i. e. laminar or turbulent.

Static pressure taps were located along the models and over the corresponding bases, as shown in Figs. 5a to 5e for both the up stream and down stream models. Various modules of the reference configurations were manufactured so as to measure specific details of the flow. The cone-cylinder model for the down stream sting had 32 taps located along its length, as shown in Fig. 5a. The exact location of the taps are given in body diameters from the nose of the projectile and these are also given in the figure. The taps were spaced more closely at the nose-cylinder junction to measure the expected pressure rise in that region.

All the other static pressure tests were conducted on the up stream sting for both the cone-cylinder (Model A) and the finned configuration (Model B). Pressure taps on Model A were installed along the top of the base (Fig. 5b) and on the base itself as shown in Fig. 5c. Again, the exact locations of these taps are given in the appropriate figure. The maximum use of the channels from the pressure transducer were utilized so as to obtain the maximum capacity in a given test run.

Figures 5d and 5e show the locations of the pressure taps along the surface and in-between the fins and on the base, respectively, on the fin model (Model B) on the up stream sting support. In-between the fins, the pressure taps were located at roll orientations angles  $\phi$ , of  $22.5^\circ$ ,  $45.0^\circ$  and  $62.5^\circ$  with respect to the top fin, as shown in Fig. 5d. Eleven taps were allocated for each circumferential position. On the base (Fig. 5e), they were located from the top fin to the bottom of the lower fin. Some surface pressure results obtained on the down stream sting in the ISL wind tunnel will be presented in this report for this configuration. The surface locations of the taps for that case were in front of the top fin, and at roll orientations  $\phi$ , of  $22.5^\circ$  and  $45^\circ$  in-between the fins.

## UNCLASSIFIED

5

2.4 Instrumentation

Standard instrumentation (Pitot tubes, wall pressure taps and temperature probes) located in the plenum chamber and in the test section were used to monitor the tunnel free stream conditions. Static pressures were measured by means of Rosemount pressure transducers.

Pressure measurements on the models and over the base were obtained by means of electronically scanned ESP pressure modules (Pressure Systems Inc.).

Forces and moments were measured with six component strain gauge balances. Two types of balances were used in these tests, a 12.7 mm ABLE 0.5 MK-X-B and a 19.05 mm ABLE 0.75 MK-XIX-C. The balance that was used for each tests series is given in Table II. The dimensions and characteristics of the balances are given in Figs. 6a and 6b for the 12.5 mm and 19.05 mm balances, respectively.

The boundary layer profiles on the up stream sting were obtained up stream of the base by means of a "duck beak" Pitot tube as shown in Fig. 7.

2.5 Data Acquisition and Data Reduction

For each run, the analog output signals from both the balance and the pressure transducers were digitized and then fed into an HP-375 microcomputer for storage and later analysis. A separate tare run was done at  $M = 0.0$  to allow for correction of the balance outputs due to model weight. Resulting data were reduced and processed according to the following equations:

$$M_i = \left[ \left( \left( \frac{P_{ti}}{P_{vi}} \right)^{\frac{\gamma-1}{\gamma}} - 1 \right) \frac{2}{\gamma-1} \right]^{\frac{1}{2}}$$

UNCLASSIFIED

6

$$P_t = \frac{\sum P_{ti}}{n} \quad n = \text{number of readings}$$

The free stream Mach number ( $M_\infty$ ), used in the following formulations in the data reduction and reported later on, was based on the average of Tap 7 located on the side wall of the wind tunnel (Refs. 6-7). Therefore,

$$M_\infty = \overline{M}_7$$

The other parameters are given as:

$$P_s = P_t \left[ 1 + \frac{\gamma - 1}{\gamma} M_\infty^2 \right]^{\frac{-\gamma}{\gamma - 1}}$$

$$Q = \frac{\gamma}{2} M_\infty^2 P_s$$

$$S = \frac{\pi d^2}{4}$$

$$CN = \frac{N}{QS}$$

$$CY = \frac{Y}{QS}$$

$$XCP = - \frac{CM}{CN}$$

$$CA = \frac{A}{QS}$$

$$CDT = CA \cos \alpha + CN \sin \alpha$$

## UNCLASSIFIED

7

The sting to model diameter ratio for Models A and B was 0.40 and 0.51 when used with the 12.5 mm and 19.05 mm balances, respectively. These are based on a model body diameter of 40 mm. The presence of the sting disturbs the flow around the base, causing an error in the base drag component. Therefore, the forebody drag coefficient CDF was obtained by subtracting the base drag CDB (deduced from pressure measurements at the base) from total drag CDT.

$$CDF = CDT - CDB \cos \alpha$$

$$CDB = - \frac{P_b S_b}{QS}$$

where  $P_b$  is the base pressure with respect to the wall pressure,  $P_b = P_{base} - P_{\infty}$

$$T_v = T_a \left( 1 + 0.2 M_{\infty}^2 \right)^{-1}$$

$$\mu = 1.458 \times 10^{-6} \frac{\sqrt{T_v}}{T_v + 110.4}$$

$$\rho = \frac{P_t}{287.05 T_a} \left( \frac{T_v}{T_a} \right)^{2.5}$$

$$Re = \frac{\rho U_{\infty}}{\mu}, \quad (m^{-1})$$

$$Re_d = \frac{\rho U_{\infty} d}{\mu}$$

$$Re_l = \frac{\rho U_{\infty} l}{\mu}$$

## UNCLASSIFIED

8

Aerodynamic coefficients (CN, CM, CA, CY, etc....) were obtained by best least-square fitted polynomials through the measured experimental data as follows:

Parameter	Polynomial
CN	$A_0 + A_1\alpha + A_3\alpha^3 + A_5\alpha^5 + A_7\alpha^7$
CM	$A_0 + A_1\alpha + A_3\alpha^3 + A_5\alpha^5 + A_7\alpha^7$
CA	$A_0 + A_2\alpha^2 + A_4\alpha^4 + A_6\alpha^6 + A_8\alpha^8$
CY	$A_0 + A_1\alpha + A_2\alpha^2 + A_3\alpha^3 + A_4\alpha^4$
CYM	$A_0 + A_1\alpha + A_2\alpha^2 + A_3\alpha^3 + A_4\alpha^4$

The variation of CNA and CMA at zero angle of attack was calculated as the slopes of a best least-square straight line fitted to the data over the range of  $-5^\circ$  to  $+5^\circ$ .

$$CNA = A_1 \text{ of polynomial } "A_0 + A_1\alpha"$$

$$CMA = A_1 \text{ of polynomial } "A_0 + A_1\alpha"$$

The axial force coefficient  $CA_0$  is given by the first coefficient of a polynomial fitted to the CA data ( $A_0$  above).

The center of pressure location  $XCP_0$  is the ratio of CMA to CNA.

Further details about the experimental program and experimental uncertainties are provided in Refs. 6 - 7.

## UNCLASSIFIED

9

3.0 RESULTS

Experimental results were obtained for different Mach numbers, angles of attack and roll angle orientations. The results available and the tests that were conducted on each configuration are summarized in Table III. Due to the different experimental setups, measurements could not be achieved for each configuration at the same Mach numbers, angles of attack and roll angle combinations. For the reasons mentioned previously (Section 2.3), base pressure measurements and boundary layer profiles could only be undertaken at  $M = 2.0$  and  $\alpha = 0^\circ$  on the up stream sting.

Static pressure distributions were conducted only on the model without fins on the down stream sting at Mach 2.0 and 4.0. Force and moment measurements to obtain aerodynamic coefficients were conducted on both models at Mach 2.0, 2.5, 3.0, 3.5 and 4.0 and only on the down stream sting support. The static pressure distributions along the model and over the base were normalized by the measured free stream static pressure. The complete set of the data available from this investigation can be found in Refs. 6 - 7.

Where appropriate, the experimentally measured non-dimensional aerodynamic force and moment coefficients were compared with predicted values obtained using an empirical method used in PRODAS (PROjectile Design and Analysis System). PRODAS (Ref. 8) is a tool utilized to design and analyze various aspects of a weapon system efficiently and quickly. Some of its capabilities include projectile (spin and fin stabilized) modeling, mass properties, aerodynamic coefficient estimation, stability analysis, internal ballistics, trajectory simulation, etc. PRODAS is an integrated system with a common data base and it has been developed using proven methodologies and techniques so that the predicted performance estimates are based in part on prior experimental testing. The projectile model and the aerodynamic coefficient predictions were computed by empirical equations contained in the Finner code of PRODAS.

UNCLASSIFIED

10

### 3.1 Boundary Layer Profiles

The boundary layer was characterized by a duck beak Pitot-type system, as mentioned previously (Section 2.4). The boundary layer profiles were only measured along the up stream sting mounted afterbody at a station  $x/D = -1.75$  up stream from the base. Due to the very low Reynolds number in the DREV wind tunnel and because of the long cylindrical body of the up stream support system, it would be expected that the boundary layer profile be laminar and thick. Indeed, preliminary boundary layer measurements showed that the profile was laminar and about 30 mm thick. The flow was therefore tripped by a sand paper collar located at 4 calibres from the base to make the profile turbulent and the boundary layer thickness was reduced by the use of an adjustable up stream-sting suction system (Fig. 4b). Extensions were utilized on the down stream support system to make sure that the base of both models were both in the test cone, or Mach rhombus, at Mach 2.0. This is important since the flow had to be fully developed, uniform and parallel where the measurements were taken.

A power law of the form:

$$\frac{\bar{u}}{U_{\infty}} = \left( \frac{y}{\delta} \right)^{\frac{1}{N}}$$

was used to fit the best curve to the normalized velocity data. The boundary layer thickness,  $\delta$ , was defined as the point at which  $\frac{\bar{u}}{U_{\infty}}$  was equal to 0.995.

Figure 8 compares the experimental boundary layer profile and the power law that best fitted the data. The displacement thickness ( $\delta_1$ ), momentum thickness ( $\delta_2$ ) and shape factor ( $H$ ) were subsequently calculated by numerical integration of the following equations:

$$\delta_1 = \int_0^{\delta} \left( 1 - \frac{\rho}{\rho_{\infty}} \frac{\bar{u}}{U_{\infty}} \right) \left( 1 + \frac{y}{R} \right) dy$$

UNCLASSIFIED

11

$$\delta_2 = \int_0^\delta \frac{\rho}{\rho_\infty} \frac{\bar{u}}{U_\infty} \left(1 - \frac{\bar{u}}{U_\infty}\right) \left(1 + \frac{y}{R}\right) dy$$

$$H = \frac{\delta_1}{\delta_2}$$

where

$$\frac{\rho}{\rho_\infty} = \frac{1 - C_r^2}{1 - C_r^2 \left(\frac{\bar{u}}{U_\infty}\right)^2}$$

$$C_r^2 = \frac{M_\infty^2}{\frac{2}{\gamma - 1} + M_\infty^2} \quad \text{Crocco Number}$$

The resulting boundary layer parameters were:

boundary layer thickness: $\delta$	19.3 mm
power law exponent: N	7.47
displacement thickness: $\delta_1$	5.618 mm
momentum thickness: $\delta_2$	1.882 mm
shape factor: H	2.986

The value of the shape factor is that for which the power law corresponds to a fully developed turbulent flow from Ref. 9.

### 3.2 Reference Projectile A (without Fins)

#### 3.2.1 Pressure Distributions along the Forebody

Static pressure measurements were conducted at  $M = 2.0$  and  $4.0$  for  $\alpha = 0^\circ, \pm 5^\circ, \pm 10^\circ, \pm 15^\circ$  and for  $\varphi = 0^\circ, 22.5^\circ, 45^\circ$  and  $67.5^\circ$  on the down stream



UNCLASSIFIED

12

sting. Figure 9 shows the angle-of-attack effects on the surface pressure distribution along the cone-cylinder forebody for  $M = 2.0$  and a roll angle of  $0^\circ$ . The results were also compared with the experimental data obtained at ISL (Ref. 2). For  $\alpha = 0^\circ$  and, as expected, the pressure increases very rapidly behind the attached nose shock to reach a constant value all over the cone, it then drops very quickly across the expansion fan produced by the discontinuity between the cone and the cylinder and then finally increases towards the free stream pressure. The average value of  $P/P_\infty$  over the cone is equal to 1.53, which agrees well with the results obtained in the ISL wind tunnel ( $P/P_\infty = 1.49$ ), as shown in Fig. 9. At angles of attack, the trend of the curves were identical to the zero angle-of-attack case, but the magnitudes of  $P/P_\infty$  were, as expected, respectively higher and lower for positive and negative angles of attack. For  $\alpha = \pm 5^\circ$ , good agreement is again observed with the ISL results from Ref. 2.

The same pressure distributions are shown in Fig. 10 for  $M = 4.0$  and at higher angles of attack. Curve trends are similar to Mach 2 (Fig. 9), but the magnitudes of the constant value over the cone are higher by approximately 35% than those for  $M = 2.0$ . For  $\alpha = 0^\circ$ ,  $P/P_\infty = 1.53$  for  $M=2.0$  and 2.37 for  $M = 4.0$ .

The surface pressure distributions at Mach 4 and at angles of attack of  $0^\circ$  and  $\pm 5^\circ$  are compared with those measured from ISL in Fig. 11. There is a difference in the results along the cone between the two facilities. In all the cases, the DREV results are lower than those from ISL. It should be mentioned that the static pressure in the DREV indraft wind tunnel at Mach 4 is approximately 1/1000 of the ambient static pressure and precise instruments are required to measure the reference static pressure. It is possible in this case that the instruments were not well calibrated or that their resolution was not sufficient.

UNCLASSIFIED

13

### 3.2.2 Circumferential Surface Pressure Distributions

The normalized surface pressure as a function of the circumferential station at angles of  $5^\circ$ ,  $10^\circ$  and  $15^\circ$  for three locations along the model for  $M = 2.0$  and  $4.0$  are presented in Figs. 12a to 12c and 13a to 13b, respectively. In the region of the cone ( $x/D = 1.4$ ), the pressure is higher on the windward surface than the averaged  $P/P_\infty$ , while lower on the leeward surface. At the farthest down stream station ( $x/D = 4.2$ ), the pressure on the windward surface is equal to the leeward surface with a minimum at  $\phi = 90^\circ$ . The results at the other stations are quite similar for all circumferential positions.

### 3.2.3 Afterbody Pressure Distributions

Afterbody pressure measurements were only conducted at  $M = 2.0$  and for  $\alpha = 0^\circ$  for the reasons given in Section 2.3. Figure 14 compares the normalized pressure distributions along the afterbody on the up stream sting support that were measured at DREV and ISL. Between  $x/D = -3.0$  and  $x/D = -0.4$  the pressure is constant and almost equal to  $P_\infty$  since the boundary layer is fully developed along the sting. Close to the base edge, the pressure decreases slightly. Good agreement is seen with ISL wind tunnel results.

The normalized base pressure measurements from DREV and ISL are shown in Fig. 15 as a function of the normalized radial distance  $y/R$ . As for the ISL results, one can note that  $P_b/P_\infty$  is almost constant over the base despite a slight increase close to the base edge. However, the DREV wind tunnel values of  $P_b/P_\infty$  are slightly higher. This is due to the difference of boundary layer thicknesses between the two wind tunnels. Indeed, previous results (Ref. 9) have shown that the base pressures are slightly higher with thicker initial boundary layers than with thinner boundary layers. This effect can be seen in Figs. 15b and 15c, which shows the base pressure evolution as a function of the suction rate. A suction valve setting of  $90^\circ$  corresponds to the maximum suction available from the system. Figure 15b corresponds to the up stream sting with no sand paper collar to trip the boundary layer, while Fig. 15c does. In both cases, the base pressure decreases with the increasing suction rate along the afterbody sting. The effect is less pronounced when the boundary

UNCLASSIFIED

14

layer is fully turbulent (Fig. 15c). In our case, the averaged base pressure for a boundary layer thickness of 19.4 mm (DREV case) is equal to 0.658, whereas for  $\delta = 5$  mm (ISL case)  $P_b / P_\infty = 0.615$ . Figure 16 shows a comparison of the averaged pressure over the base as a function of Mach number with the previous published results. Despite the different experimental conditions (model supports, boundary layer effects, etc.) and the measurement uncertainties, good agreement and trends on similar afterbody configurations were observed.

### 3.2.4 Aerodynamic Coefficients

Aerodynamic forces and moments reduced to non-dimensionalized coefficients were obtained at  $M = 2.0, 2.5, 3.0, 3.5$  and  $4.0$  for angles of attack  $\alpha$  ranging between  $-6^\circ$  and  $+15^\circ$ . The aerodynamic coefficients were plotted for each run as a function of angle of attack. Where appropriate, the wind tunnel measurements were compared with predicted values obtained by using an empirical method used in PRODAS as explained previously.

Table IV summarizes the experimentally determined coefficients for CNA, CMA, CA0 and XCP0 for the 8 runs undertaken for the reference projectile A.

#### 3.2.4.1 Axial Force Coefficient

The Mach number effects on the axial force coefficient as a function of angle of attack are shown in Fig. 17a. As expected the axial force coefficient decreases as the Mach number increases and the trend with angle of attack is of a parabolic profile about  $0^\circ$  for all the tested Mach numbers. The PRODAS predictions for the axial force coefficient at  $0^\circ$  angle of attack, CA0, are compared with the wind tunnel values in Fig. 17b as a function of the Mach number. The main trend as well as the magnitudes of CA0 versus Mach number are in very good agreement.

## UNCLASSIFIED

15

#### 3.2.4.2 Normal Force Coefficient

The Mach number effects on the normal force coefficient as a function of the angle of attack is shown in Fig. 18a. The normal force coefficient, at the lower values of angle of attack, is not greatly influenced by the Mach number. Small differences can be noticed at the higher angles of attack. The normal force coefficient slope, CNA, estimated from PRODAS, are compared with the experimental values in Fig. 18b as a function of the Mach number. One can note that the wind tunnel CNA increases with Mach number. This is rather unusual, as one would expect a slight decrease in CNA, or at most a constant value, as the Mach number increases, as with the PRODAS estimates. No explanation for this behavior is apparent for the moment. CFD simulations should be conducted to investigate the CNA trends for this configuration.

#### 3.2.4.3 Pitching Moment Coefficient

The Mach number effects on the pitching moment coefficient as a function of the angle of attack is shown in Fig. 19a. The pitching moment coefficient, CM, is given with respect to the projectile base. As for the CN results, the pitching moment coefficient is not greatly influenced by the Mach number for all the angles of attack. The PRODAS estimates for the pitching moment coefficient slope, CMA, are again compared with the experimental results in Fig. 19b and good agreement is obtained.

#### 3.2.4.4 Center of Pressure Location

The location of the center of pressure, XCP, versus the angle of attack and Mach number is given in Figs. 20a and 20b. It is defined in calibres and the zero value corresponds to the model base. The center of pressure is located at the cone-cylinder junction at Mach 2 and progresses slightly towards the model base as the Mach number increases. The PRODAS estimates are in quite good agreement with the wind tunnel results.

UNCLASSIFIED

16

#### 3.2.4.5 Yawing Moment Coefficient

The Mach number effects on the yawing moment coefficient, CYM, as a function of angle of attack is shown in Fig. 21. CYM remains fairly constant at near zero in the range of the measured angle of attack and shows no definite trends. A high scatter in the experimental results was also observed due to the small magnitude of the measured moment.

### 3.3 Reference Projectile B (with Fins)

#### 3.3.1 Pressure Distributions along the Forebody

The pressure distributions along the forebody of the reference projectile B (model with fins) on the down stream sting were only conducted at ISL. The results have not yet been published and are included in this report for completeness. ISL had pressure taps in front of one fin,  $\phi = 0.0^\circ$ , and in-between the fins at  $\phi = 22.5^\circ$  and  $45.0^\circ$  with respect the top fin in the up position ( $\phi = 0.0^\circ$ ) when looking from the rear.

The normalized pressure distribution,  $P/P_\infty$ , along the projectile for circumferential fin positions,  $\phi$ , of  $0^\circ$  and  $45^\circ$  and for angles of attack of  $0^\circ$ ,  $5^\circ$  and  $-5^\circ$  for  $M = 2.0$  are shown in Figs. 22a to 22e. For  $x/D < -1.5$  (not plotted here), the pressure distributions behave the same way as for projectile A. In-between the fins ( $-1.5 < x/D < 0.0$ ), the pressure distributions are affected by the interaction of the recompression shocks originating from the fin leading edges. Peaks indicate the location of the shock-boundary layer interaction along the body as shown in Fig. 25b. As expected, maximum pressure values are obtained for  $\alpha = +5^\circ$  and for  $\phi = 45^\circ$  (Fig 22c).

DREV conducted a series of tests at Mach 2 on the up stream sting similar to the ones mentioned above. These were conducted at  $0^\circ$  angle of attack at  $\phi = 0^\circ$  and the results are given in Fig. 22f. The equivalent test at ISL on the down stream sting is given in Fig. 22a. Since the DREV tests were conducted on the up stream sting, the normalized pressure  $P/P_\infty$  just ahead of the fins is 1.0. These results would be more representative of a very high length

UNCLASSIFIED

17

to diameter ratio flechette projectile, since the pressure  $P$  would have sufficient length to reach  $P_\infty$  ahead of the fins. The pressure distributions at  $\phi = 22.5^\circ$  and  $67.5^\circ$  give the same results, as expected. Due to the short length of the model on the down stream sting at ISL,  $P/P_\infty$  did not attain the free stream pressure just ahead of the fins, as expected (Fig. 22a). The trends in the  $P/P_\infty$  results from both sting supports are similar for  $\phi = 22.5$  and  $45^\circ$ . At the leading edge of the fins there is a slight pressure rise due to a recompression shock and the values remain slightly higher than the free stream values at the trailing edge of the fins. The relative maximum pressure peaks are higher with the ISL measurements than those obtained at DREV. The ISL maximum pressure rise in  $P/P_\infty$  is 0.17, while the DREV one is 0.1. These are probably due to the different boundary layer thicknesses.

At Mach 4, the normalized pressure distributions ( $P/P_\infty$ ) obtained at ISL along the projectile for circumferential fin positions,  $\phi = 0^\circ$  and for angles of attack of  $0^\circ$ ,  $5^\circ$  and  $-5^\circ$  are presented in Figs. 23a to 23c. Again, as for the reference projectile A, curve trends in Fig. 23a are similar but magnitudes of the pressure values over the cone are, as expected, higher by about 40% than for  $M = 2.0$ . In-between the fins, Fig. 23b to 23c, one can note that there is no significant difference in the trends of the pressure distributions obtained at  $M = 2.0$ .

### 3.3.2 Afterbody Pressure Distributions

Pressure measurements over the base were only conducted at  $M = 2.0$  and for  $\alpha = 0^\circ$ . The base pressure distribution  $P_b$ , normalized by the free stream static pressure  $P_\infty$  obtained from both wind tunnel facilities are compared in Fig. 24. In contrast to the case of an afterbody without fins (Model A), the magnitude of the base pressures is lower and the pressure distribution profile is not constant. Magnitude shifts in the DREV and ISL values are again due to differences in the thickness of the boundary layers in the two wind tunnels.

In general, pressure values over the base are lower for the cylindrical afterbody (Model A). The maximum value located at the center of the base

UNCLASSIFIED

18

indicates the existence of a stagnation point. The minimum value is obtained next to the base edge and fin junction. There are also high pressure gradients in the vicinity of the mixing layers originating from the edge of the base and the fin tips. This could be explained by an increase of the boundary layer thickness at the base edge generated by the interactions of the flow in-between the fins, as mentioned previously for the reference projectile B.

A schematic demonstrating the complexity of the flow at the base of the finned model is shown in Fig. 25a. A shadowgraph obtained from the ISL wind tunnel in Fig. 25b shows many of the features given in the schematic.

### 3.3.3 Aerodynamic Coefficients

The reduced aerodynamic force and moment coefficients were obtained at  $M = 2.0, 2.5, 3.0, 3.5$  and  $4.0$  for angles of attack  $\alpha$  ranging between  $-5^\circ$  and  $+15^\circ$  and for roll angle orientations  $\phi = 0^\circ, 22.5^\circ, 45^\circ$  and  $67.5^\circ$ . Once more, the PRODAS predictions were compared with the experimental results where appropriate.

Table V summarizes the experimentally determined coefficients  $C_{NA}$ ,  $C_{MA}$ ,  $CA_0$  and  $XCP_0$  for the 26 runs that were conducted for the reference projectile B, with fins.

#### 3.3.3.1 Axial Force Coefficient

Figures 26a and 26b and 27a to 27c show the Mach number and roll angle effects on the axial force coefficient as a function of angle of attack, respectively. As for reference projectile A,  $CA$ , in general, increases with incidence. The axial force coefficient should be of a parabolic profile about  $0^\circ$  angle of attack and also should pass through a common point ( $CA_0$ ) irrespective of the roll orientation of the fins. This seems to be quite apparent in all of our cases.

UNCLASSIFIED

19

The PRODAS predictions for the axial force coefficient at zero angle of attack,  $CA_0$ , are compared with the experimental results as a function of Mach number in Fig. 28. There seems to be a measurement discrepancy at Mach 2 or 2.5 since one of these experimental values does not follow the main trend. This matter is under investigation. The PRODAS predictions underestimate slightly the wind tunnel results. The axial force coefficient,  $CA_0$ , of the finned model is approximately 50% higher than the model with no fins (Fig. 17b).

The roll orientation effect on the axial force coefficient,  $CA_0$ , is shown in Fig. 29. For all Mach numbers,  $CA_0$  is relatively constant with respect to the roll orientation. It would be expected, at zero angle of attack, that  $CA_0$  would not vary at all. But since the model is swept during a test, any influence of the angle of attack and the roll orientation on  $CA_0$  (induced axial force coefficient), will show up as small variations in  $CA_0$  in the fitting process.

### 3.3.3.2 Normal Force Coefficient

Figures 30a and 30b and 31a to 31c show the evolution of the normal force coefficient,  $CN$ , as a function of angle of attack for  $M = 2.0, 2.5, 3.0, 3.5$  and  $4.0$ , for a roll angles,  $\phi$ , of  $0^\circ$  and  $45^\circ$ , respectively. As expected, the slope decreases as the Mach increases since the fins lose effectiveness with increasing Mach number (Figs. 30a and 30b).

In Figs. 31a to 31c, one can note that  $CN$  is not influenced by the roll orientation of the fins. At Mach 4 (Fig. 31c), the results below  $\alpha = 3^\circ$  show a small change in the slope of the experimental data with respect to the main trend. This occurs for all the roll orientations and is not apparent at the other tested Mach numbers. This is not seen above an angle of attack of three degrees.

Figure 32 presents the normal force coefficient slope,  $CNA$ , versus Mach number for a roll orientation of  $\phi = 0^\circ$ . It shows, as expected, that  $CNA$  decreases with increasing Mach number as the fins lose effectiveness. The



## UNCLASSIFIED

20

PRODAS estimates were in good agreement with the wind tunnel measurements, but with a slight difference in slope.

The evolution of CNA as a function of the roll angle is shown in Fig. 33 for all of the tested Mach numbers. The results show that the roll angle orientation does not have a great influence on CNA.

CNA of the finned model is 133% higher than the cone-cylinder model (Fig. 18b) at Mach 2 and 60% higher at Mach 4.0

### 3.3.3.3 Pitching Moment Coefficient

Figures 34a and 34b and 35a to 35c show the Mach number and roll angle effects on the pitching moment coefficient,  $CM$ , as a function of angle of attack, respectively.  $CM$  is calculated with respect to the base of the projectile. The results show that  $CM$  is independent of Mach number for the two roll orientations presented (Figs. 34a and 34b). For a given Mach number (Figs. 35a to 35c),  $CM$  is not affected significantly by the roll orientation of the fins at the lower angles of attack,  $-6^\circ < \alpha < 6^\circ$ . However a small change in magnitude is notable at the higher angles of attack,  $\alpha > 6^\circ$ . Again, at Mach 4 (Fig. 35c), as noticed with CN (Fig. 31c), the results below  $\alpha = 3^\circ$  show a small change in the slope of the experimental data with respect to the main trend.

The pitching moment coefficient slope,  $CMA$ , as a function of Mach number is shown in Fig. 36 for a roll orientation of  $0^\circ$  and is compared with the PRODAS estimates. There is some variability in the experimental results but  $CMA$  does not seem to be much affected by the Mach number. PRODAS agrees very well with the wind tunnel results.

The evolution of  $CMA$  as a function of  $\phi$  is presented in Fig. 37. It would be expected that the results at  $\phi = 22.5^\circ$  and  $67.5^\circ$  be of the same order of magnitude. However, all of the experimental results show a higher value of  $CMA$  at  $\phi = 67.5^\circ$ . No reasons are available to explain these measurements.

UNCLASSIFIED

21

#### 3.3.3.4 Center of Pressure Location

The location of center of pressure versus angle of attack for roll angles of  $0^\circ$  and  $45^\circ$  at different Mach numbers are shown in Figs. 38a and 38b, respectively. XCP is defined in calibres and the zero value corresponds to the model base. The center of pressure moves very slightly towards the model nose as the Mach number increases. There is a slight shift towards the nose at  $\phi = 45^\circ$ .

The center of pressure at zero angle of attack, XCP0, as a function of Mach number is shown in Fig. 39. The center of pressure is located 0.5 calibres ahead of the fins at Mach 2 and moves slightly towards the nose of the projectile as the Mach number increases. The fins become less effective with increasing Mach number, as expected. The PRODAS predictions are in very good agreement with the experimental data points.

Figure 40 shows that XCP0 is not affected by the roll orientation of the fins at all the Mach numbers except for Mach 4, where some cyclic variation does exist.

#### 3.3.3.5 Yawing Moment Coefficient

The yawing, or side, moment coefficient, CYM, with respect to the base are given as a function of incidence for different Mach numbers and two roll angles,  $\phi = 0^\circ$  and  $45^\circ$ , in Figs. 41a and 41b, respectively. For  $\phi = 0^\circ$ , CYM shows some scatter but remains fairly constant at zero and with no specific trends over the entire range of incidence. For  $\phi = 45^\circ$ , there is slight negative slope of CYM with angle of attack for all the tested Mach numbers.

The side moment coefficient as a function of angle of attack and roll orientation are given in Figs. 42a to 42c for three Mach numbers. Runs made at roll angles of  $22.5^\circ$  and  $67.5^\circ$  should give identical but symmetrical results as side forces are concerned. This seems to be the case for all the Mach numbers. At Mach 2.0 no definite trends are observed but the scatter in the data increases with angle of attack. At Mach 3, the scatter is less and the  $\phi =$

UNCLASSIFIED

22

45° trend is different from the other three roll orientations. At Mach 4, CYM has a relatively constant slope at 0 angle of attack and for  $\phi = 0^\circ$  and a slightly negative slope for the other roll orientations.

#### 4.0 CONCLUSIONS

As a first phase in an aeroballistic study of two reference projectiles with an  $l/d$  of 6, the surface and base pressure measurements as well as aerodynamic forces and moments were measured in the DREV indraft wind tunnel. The projectiles consisted of a cone-cylinder with and without fins. Tests were conducted with both an up stream and down stream sting support system. Results were obtained for various angles of attack and fin roll orientation at Mach numbers ranging between 2 and 4. Where appropriate, the wind tunnel results were compared with those from the ISL wind tunnel and with predicted values from the PRODAS simulation code.

The aerodynamics of the two reference projectiles were generally as expected except for the trend of CNA versus Mach number for the reference projectile without fins. In that case the trend was opposite to the expected one. No dependence on the roll orientation was noticed on the main aerodynamic coefficients,  $CA_0$ , CNA, CMA and CYM. The PRODAS predicted values compared quite well with the wind tunnel results.

Surface pressure distributions were measured along the forebody on the down stream support system at Mach 2 and 4. The comparisons with the ISL results at Mach 2 and for all angles of attack tested were in excellent agreement, while some slight differences were noticed along the cone at Mach 4.

Various pressure measurements, along the surface of the afterbody and at the base of both reference models were taken with an up stream sting support system. Such a system was designed to eliminate any disturbances from the classical down stream sting or strut support. The boundary layer was characterized as fully turbulent when a sand paper collar was used with the maximum suction capability of the system.

UNCLASSIFIED

23

The surface pressure measurements on the cylindrical afterbody agreed very well between both wind tunnels. The base pressure on both the cylindrical afterbodies, with and without fins, were higher in the DREV tunnel. This was attributed to the different boundary layer thicknesses. Other investigators have shown that the base pressures are slightly higher with thicker initial boundary layers. This was also shown in these tests as a function of the suction rate for both laminar and turbulent boundary layers. The surface pressure distributions between the fins were measured at various angles of attack and roll orientations. As well, the shock-boundary layer interactions between the fins were characterized.

The wind tunnel results presented in this report and those obtained from free-flight trials in an aeroballistic range for the model with fins (Ref. 3) constitute a comprehensive and reliable data base on two classical projectile shapes. These results can readily be used to validate the computational fluid dynamics codes that are being used as an integral tool in aerodynamic research. Free-flight tests should be conducted on the cone-cylinder reference projectile to complete the data base.

With such an experimental data base, wind tunnel tests can be conducted on novel projectile bases in an attempt to reduce the drag and improvements can immediately be quantified. The benefits of using lateral jets over the classical control surfaces can also be investigated, either with experiments or CFD computations, by using these reference projectiles. The aerodynamic interference of projectiles flying in formation, for example in a tandem configuration, can also be quantified by conducting tests simultaneously on the up stream and down stream support systems with these reference projectiles.

With this comprehensive aerodynamic data base of classical projectile shapes, many studies can be conducted to test new technologies, methodologies or applications, as mentioned above, to improve the performance and capability of many weapon systems. It has been demonstrated that future efforts can be concentrated in testing and evaluating

UNCLASSIFIED

24

the weapons themselves without the need for more measurements of test cases.

## 5.0 ACKNOWLEDGMENTS

The authors would like to express their thanks to Messrs. R. Bilodeau and B. Girard from DREV and Messrs. C. Demeautis and P. Duffner from ISL for their logistical and technical support in the design process and in conducting the wind tunnel tests in a very professional manner.

## UNCLASSIFIED

25

6.0 REFERENCES

1. Berner, C., Demeautis, C. and Duffner, P., "Vol de deux projectiles séparés par une faible distance. I.2. Mesures du champ des vitesses autour des projectiles de référence", ISL Report R/94
2. Berner, C., Demeautis, C. and Duffner, P., "Vol de deux projectiles séparés par une faible distance. I.1. Visualisation des écoulements et mesures de pression autour de projectiles de référence", ISL Report R107/92
3. Dupuis, A. D. and Hathaway, W., "Aerodynamic Characteristic of a Finned Projectile at Supersonic and Hypersonic Speeds from Free-Flight Tests", DREV Report DREV-R-9404, October 1994, UNCLASSIFIED
4. Berner, C., "Numerical Investigation of the DREV/ISL Reference Projectiles", ISL Report, to be published in 1996.
5. Hutt, G. R. and East, R. A., "Dynamic Pitch Stability Measurements of Slender Cone-Cylinder Finned Bodies at High Mach Numbers", 9th International Ballistic Symposium, Shrivenham, England, 29 April - 1 May, 1986
6. Girard, B., "Wind Tunnel Tests of DREV-ISL Reference Models at Supersonic Speeds", DREV technical memorandum, in preparation
7. Girard, B., "Wind Tunnel Tests of DREV-ISL Reference Afterbodies at Mach 2.0", DREV technical memorandum, in preparation
8. "Projectile Design Analysis System (PRODAS)", Arrow Tech Associates Inc., DREV Contract No. W7701-0-1227, March 1992, UNCLASSIFIED
9. Délery, J. and Sirieix, M., "Base Flows Behind Missiles", AGARD-LS-98 on Missile Aerodynamics, ONERA TP1979-14E, 1979
10. Tucker, M., "Approximate Calculation of Turbulent Boundary-Layer development in compressible flow." NACA-TN-2337, April 1951

UNCLASSIFIED

26

11. Love, F. S., "Base Pressure at Supersonic Speeds on Two-Dimensional Airfoils and on Bodies of Revolution With and Without Fins Having Turbulent Boundary Layers", NACA TN 3819, 1957

## UNCLASSIFIED

**TABLE I**Comparison of wind tunnel and free-flight Reynolds number

	DREV WIND TUNNEL		ISL WIND TUNNEL		FREE FLIGHT	
Mach Number	Re <sub>l</sub> (10 <sup>6</sup> )	Re <sub>d</sub> (10 <sup>6</sup> )	Re <sub>l</sub> (10 <sup>6</sup> )	Re <sub>d</sub> (10 <sup>6</sup> )	Re <sub>l</sub> (10 <sup>6</sup> )	Re <sub>d</sub> (10 <sup>6</sup> )
2.0	3.07	0.12	12.17	2.03	10.97	1.83
2.5	2.42	0.40	-	-	13.73	2.29
3.0	1.87	0.31	-	-	16.46	2.74
3.5	1.44	0.24	-	-	19.20	3.20
4.0	1.13	0.19	11.67	1.94	21.96	3.66

- model length  $l = 0.240$  m- model diameter  $d = 0.040$  m**TABLE II**Balances used for tests

CONFIGURATION	MACH NUMBER				
	2.0	2.5	3.0	3.5	4.0
MODEL A (without fins)	12.7 mm	12.7 mm	12.7 mm	12.7 mm	12.7 mm
MODEL B (with fins)	19.05 mm	19.05 mm	19.05 mm	12.7 mm	12.7 mm



UNCLASSIFIED

**TABLE III**  
**Summary of available data and tests**

	MODEL A (without fins)										MODEL B (with fins)					
	2.0	2.5	3.0	3.5	4.0	2.0	2.5	3.0	3.5	4.0						
M	0	0	0	0	0	0	0	0	0	0	0	0	0	0	0	
φ	≠ 0	≠ 0	≠ 0	≠ 0	≠ 0	≠ 0	≠ 0	≠ 0	≠ 0	≠ 0	≠ 0	≠ 0	≠ 0	≠ 0	≠ 0	
Static pressure distributions for the downstream model																
α = 0°	X	X <sup>(1)</sup>			X	X										
α = ±5°	X	X <sup>(2)</sup>			X	X <sup>(3)</sup>										
α = ±10°	X	X <sup>(2)</sup>			X	X <sup>(3)</sup>										
α = ±15°	X	X <sup>(2)</sup>			X											
Static pressure distribution for the upstream models at α = 0° only																
- after body	X										X	X <sup>(4)</sup>				
- base pressure	X										X					
Boundary layer profiles																
- streamwise velocity component	X															
Forces and moments																
-5° < α < + 15°	X		X		X					X	X <sup>(5)</sup>	X	X <sup>(5)</sup>	X	X <sup>(5)</sup>	

(1)  $\phi = 45^\circ$  and  $90^\circ$ (2)  $\phi = 22.5^\circ, 45^\circ, 67.5^\circ$  and  $90^\circ$ (3)  $\phi = 45^\circ, 90^\circ$  and  $180^\circ$ (4)  $\phi = 22.5^\circ$  and  $45^\circ$ (5)  $\phi = 22.5, 45^\circ$  and  $67.5^\circ$

UNCLASSIFIED

TABLE IVExperimental aerodynamic coefficients (Model A)

RUN	MACH	$\phi$	CNA	CMA	CA0	XCP0
R3751	3.99	0.0	3.748	12.604	0.207	-3.3630
R3752	3.99	0.0	3.820	12.753	0.213	-3.3385
R3768	3.50	0.0	3.688	13.058	0.225	-3.5407
R3782	2.98	0.0	3.461	12.366	0.249	-3.5732
R3800	2.48	0.0	3.154	11.972	0.287	-3.7959
R3743	1.97	0.0	2.879	12.041	0.373	-4.1822
R3744	1.98	0.0	2.985	12.293	0.367	-4.1176
R3745	1.98	0.0	2.918	12.093	0.367	-4.1439

## UNCLASSIFIED

**TABLE V**  
**Experimental aerodynamic coefficients (Model B)**

RUN	MACH	$\phi$	CNA	CMA	CA0	XCP0
R3753	3.99	0.0	5.851	13.698	.0293	-2.3411
R3754	3.98	22.5	5.791	13.822	0.300	-2.8830
R3755	3.98	45.0	5.678	14.302	0.299	-2.1588
R3756	3.98	67.5	5.736	15.166	0.300	-2.6440
R3757	3.98	67.5	5.451	14.299	0.291	-2.6231
R3770	3.50	0.0	6.039	14.388	0.325	-2.3824
R3771	3.50	22.5	6.175	15.203	0.333	-2.4622
R3772	3.50	45.0	6.088	15.547	0.319	-2.5537
R3773	3.50	67.5	6.109	16.320	0.325	-2.6713
R3787	2.97	0.0	6.311	14.165	0.371	-2.2446
R3788	2.98	22.5	6.383	14.537	0.372	-2.2776
R3789	2.98	45.0	6.302	14.843	0.357	-2.3552
R3790	2.98	67.5	6.470	15.601	0.375	-2.4112
R3791	2.98	67.5	6.470	15.565	0.358	-2.4057
R3792	2.98	67.5	6.370	15.588	0.377	-2.4473
R3793	2.98	67.5	6.414	15.678	0.369	-2.4442
R3794	2.98	0.0	6.298	14.253	0.355	-2.2633
R3795	2.98	45.0	6.359	14.933	0.358	-2.3484
R3796	2.45	0.0	6.278	13.489	0.395	-2.1484
R3797	2.47	22.5	6.360	13.896	0.396	-2.185
R3798	2.48	45.0	6.373	14.338	0.398	-2.2499
R3799	2.48	67.5	6.601	15.266	0.403	-2.3127
R3811	1.99	0.0	7.059	14.597	0.542	-2.0679
R3812	1.99	22.5	7.116	14.963	0.544	-2.1027
R3813	1.99	45.0	6.984	15.145	0.544	-2.1686
R3814	1.99	67.5	6.985	15.653	0.540	-2.2408

UNCLASSIFIED

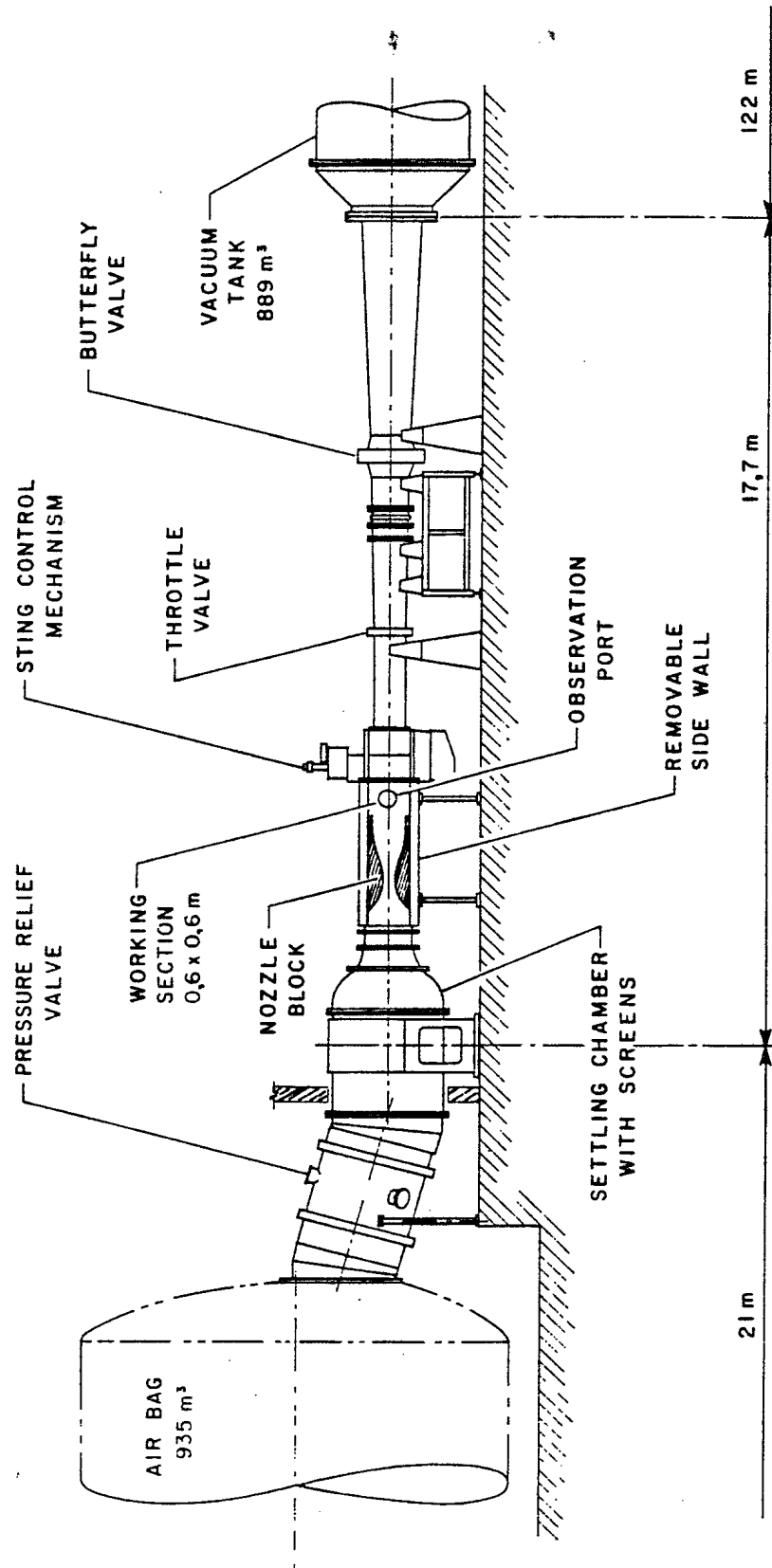


FIGURE 1 - Schematic of the DREV trisonic wind tunnel



UNCLASSIFIED

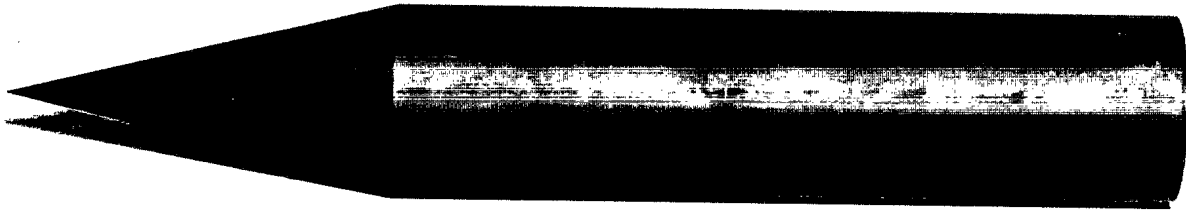
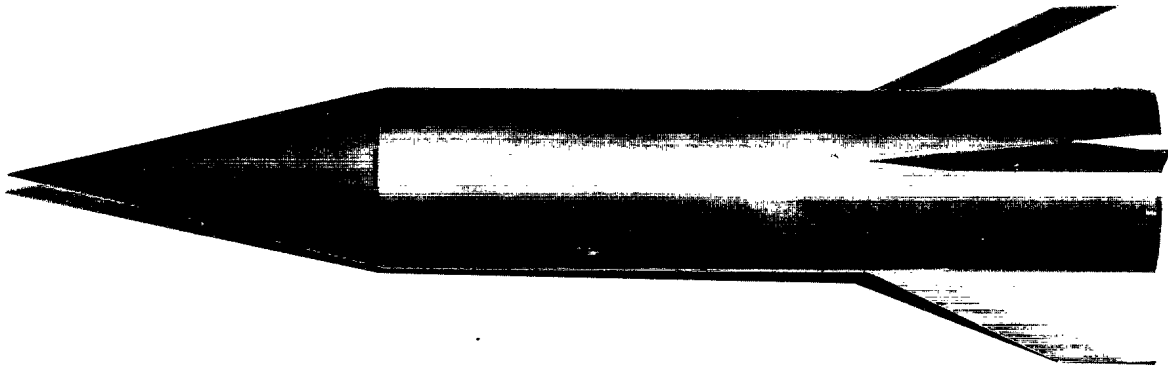


FIGURE 2 - Photographs of reference projectiles

a) Model A - without fins



b) Model B - with fins

UNCLASSIFIED

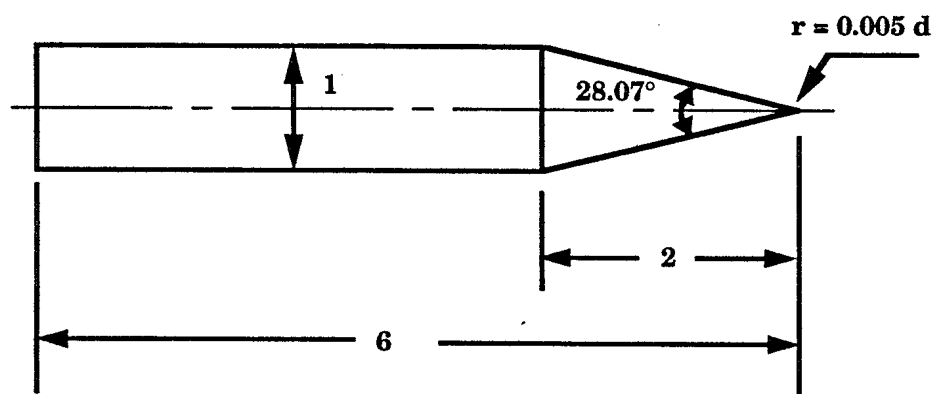
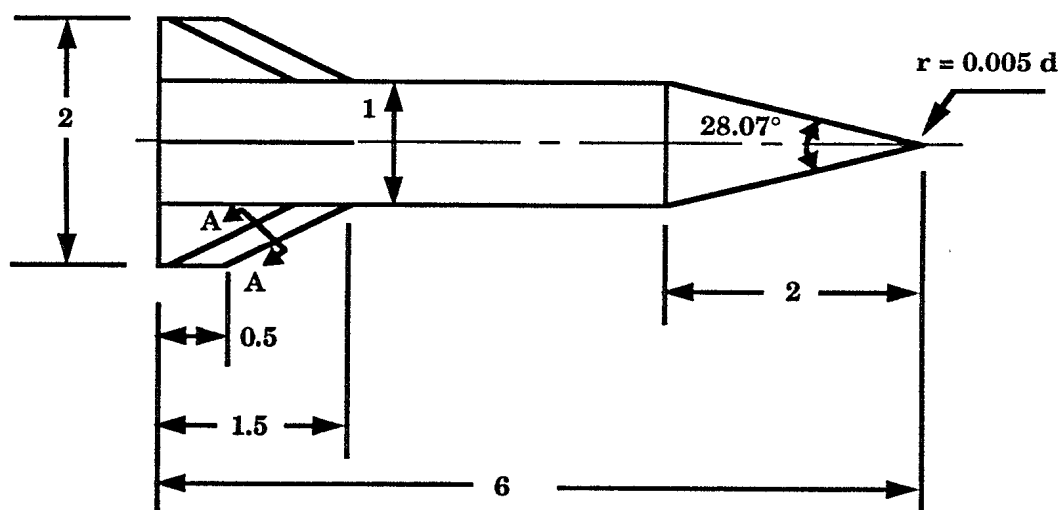


FIGURE 3 - Dimensions and characteristics of the reference projectiles (in cal)

a) Model A - without fins



SECTION A-A

b) Model B - with fins

UNCLASSIFIED

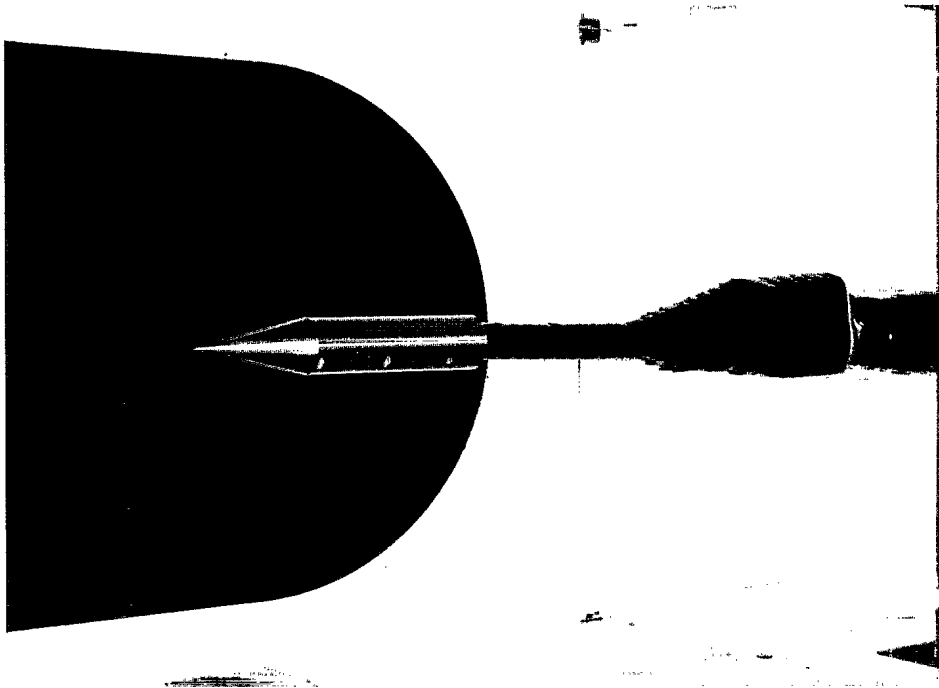
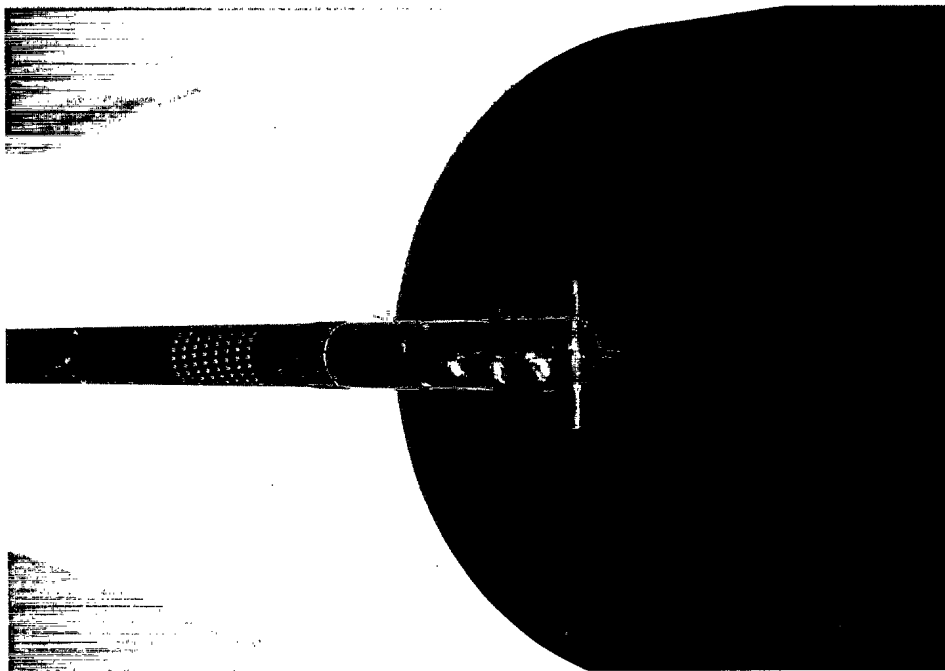


FIGURE 4 - Photographs of experimental setup

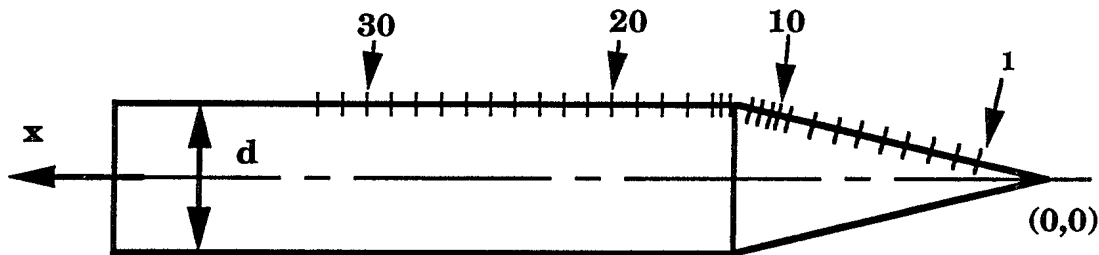
a) Standard down stream sting with Model A



b) Up stream sting with afterbody of Model B



UNCLASSIFIED

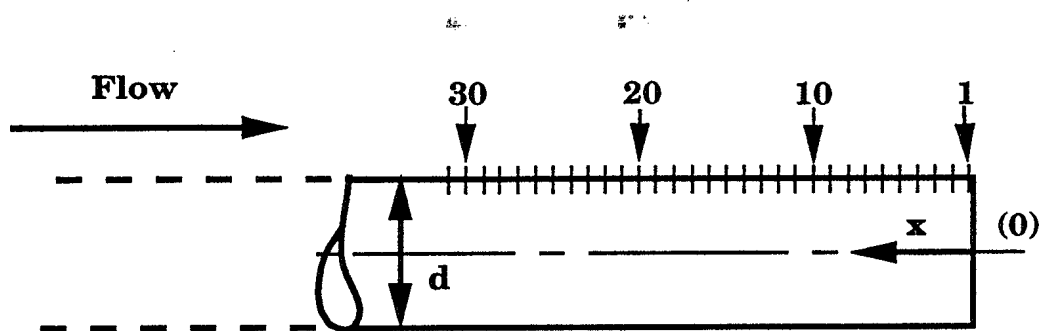


Tap Number	x/d	Tap Number	x/d
1	0.450	17	2.307
2	0.604	18	2.466
3	0.757	19	2.625
4	0.912	20	2.783
5	1.066	21	2.942
6	1.220	22	3.101
7	1.374	23	3.260
8	1.528	24	3.418
9	1.682	25	3.577
10	1.746	26	3.736
11	1.810	27	3.895
12	1.874	28	4.053
13	1.936	29	2.212
14	2.009	30	4.371
15	2.079	31	4.530
16	2.149	32	4.688

FIGURE 5 - Static pressure taps locations (in calibres)

a) Model A - along forebody - down stream sting

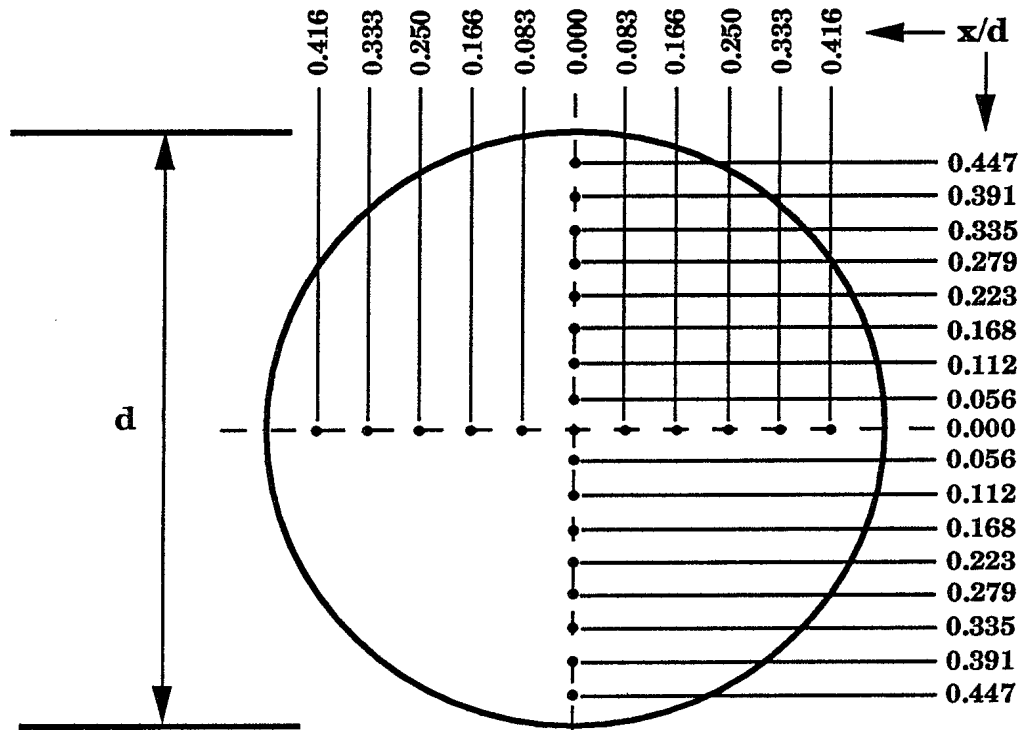
UNCLASSIFIED



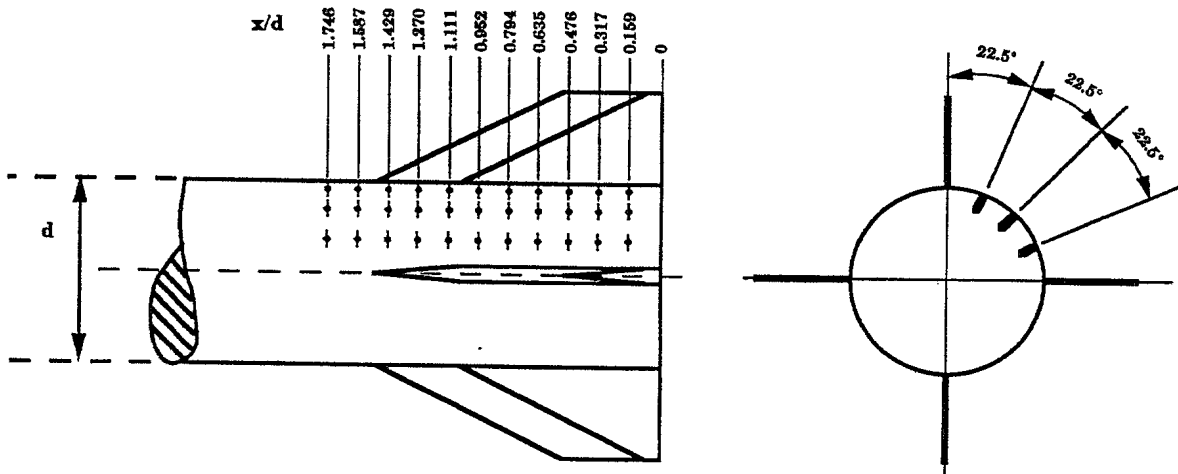
Tap Number	x/d	Tap Number	x/d
1	0.035	17	1.813
2	0.146	18	1.924
3	0.257	19	2.035
4	0.368	20	2.146
5	0.479	21	2.257
6	0.590	22	2.368
7	0.702	23	2.479
8	0.813	24	2.590
9	0.924	25	2.702
10	1.035	26	2.813
11	1.146	27	2.924
12	1.257	28	3.035
13	1.368	29	3.146
14	1.479	30	3.257
15	1.590	31	3.368
16	1.702	-	-

b) Model A - along top of base - up stream sting

UNCLASSIFIED

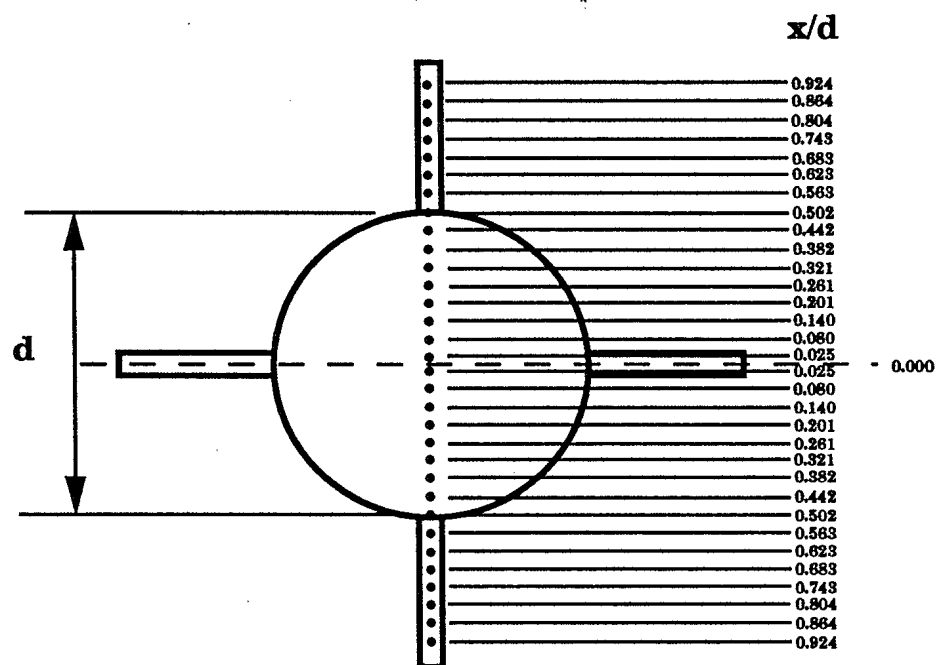


c) Model A - on the base - up stream sting



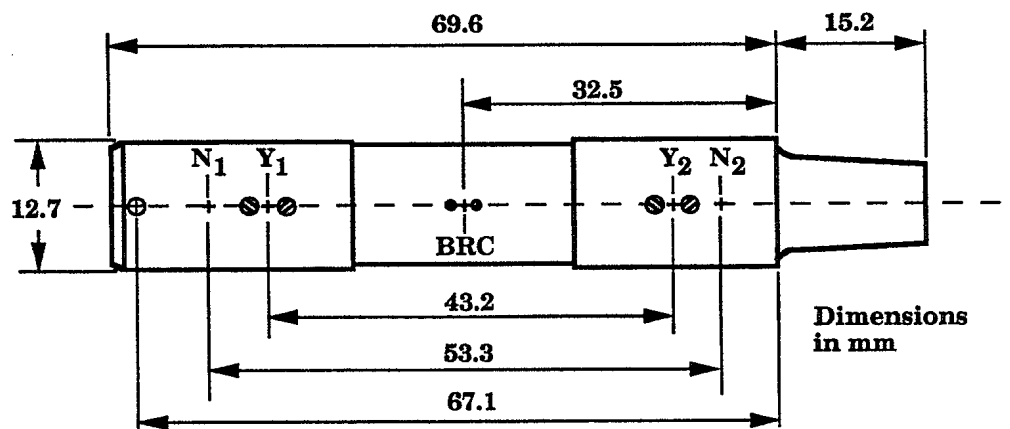
d) Model B - along top of base - up stream sting

UNCLASSIFIED



e) Model B - on the base - up stream sting

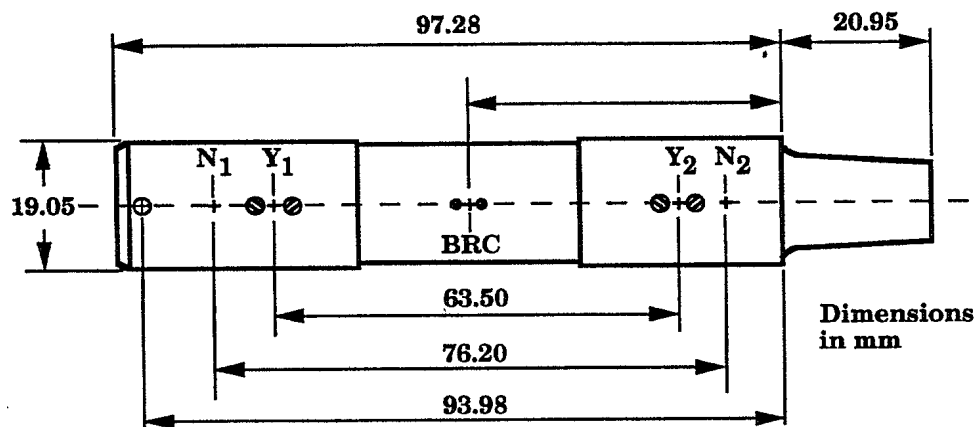
UNCLASSIFIED



Rated loads: Total Normal Force (Pitching Moment = 0) 220 N  
 Total Side Force (Yawing Moment = 0) 220 N  
 Total Axial Force 220 N  
 Rolling Moment 1.69 N•m  
 Pitching Moment (Normal Force = 0) 11.86 N•m  
 Yawing Moment (Side Force = 0) 9.60 N•m

FIGURE 6 - Dimensions and characteristics of the balances

a) 12.7 mm (0.50") balance



Rated loads: Total Normal Force (Pitching Moment = 0) 890 N  
 Total Side Force (Yawing Moment = 0) 445 N  
 Total Axial Force 334 N  
 Rolling Moment 6.78 N•m  
 Pitching Moment (Normal Force = 0) 33.90 N•m  
 Yawing Moment (Side Force = 0) 14.12 N•m

b) 19.05 mm (0.75") balance

UNCLASSIFIED

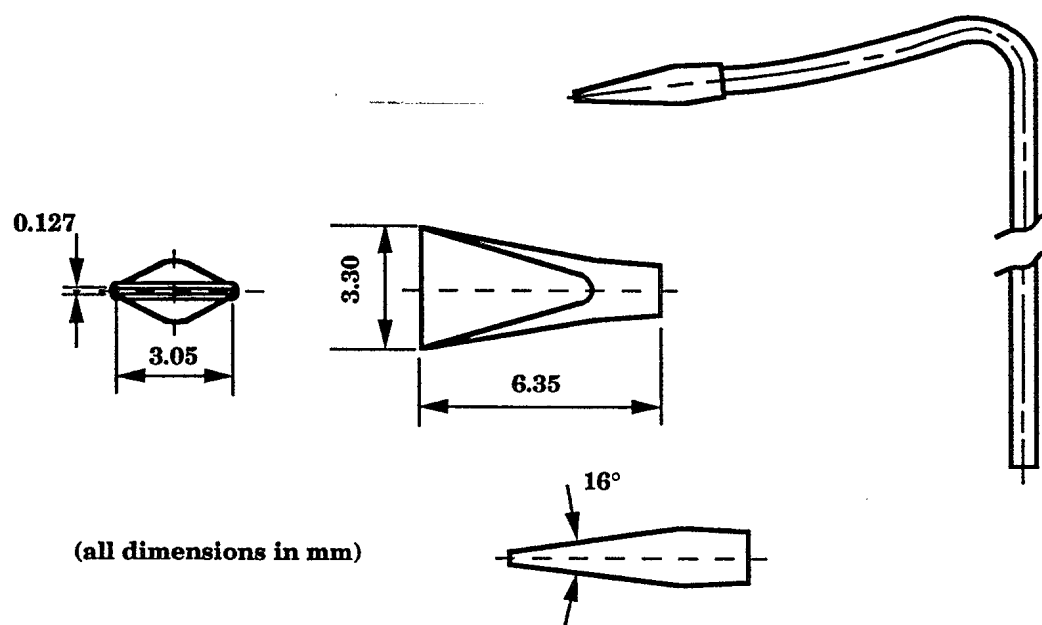


FIGURE 7 - "Duck Beak" Pitot tube used to measure boundary layer profiles

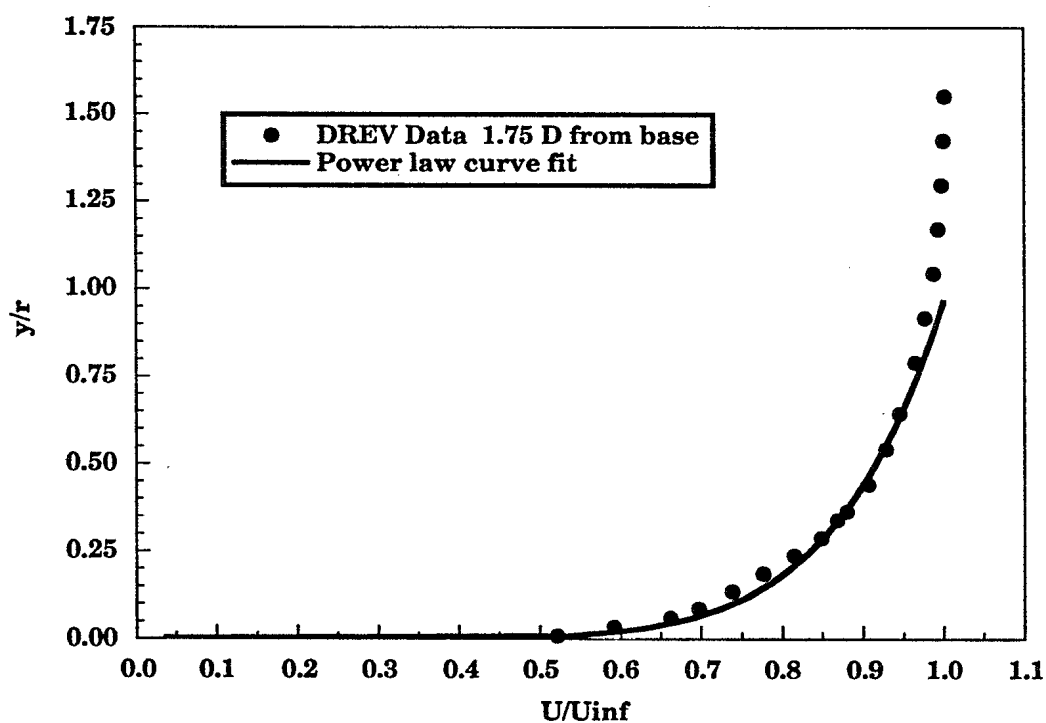


FIGURE 8 - Boundary layer profile on up stream sting

UNCLASSIFIED

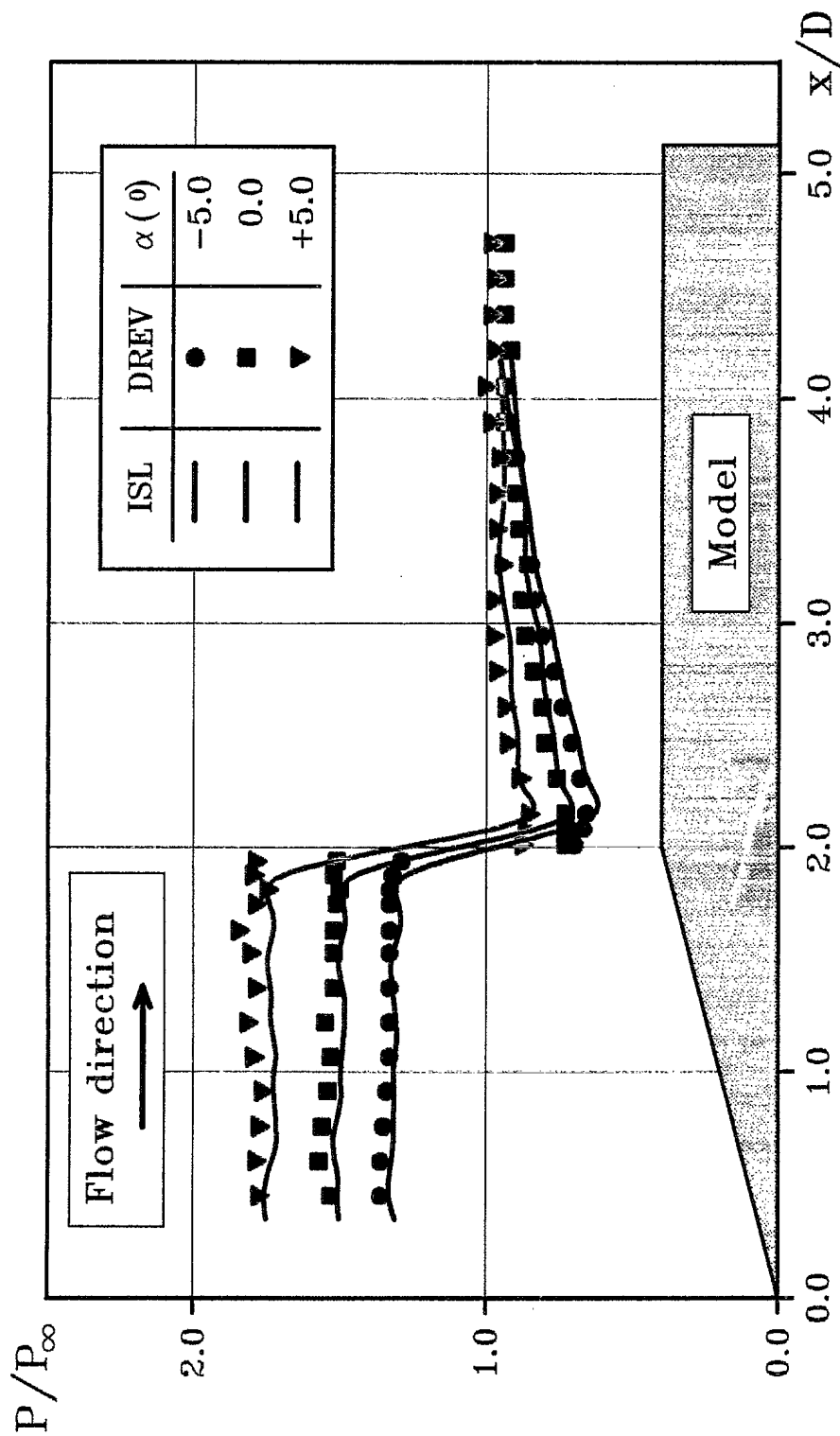
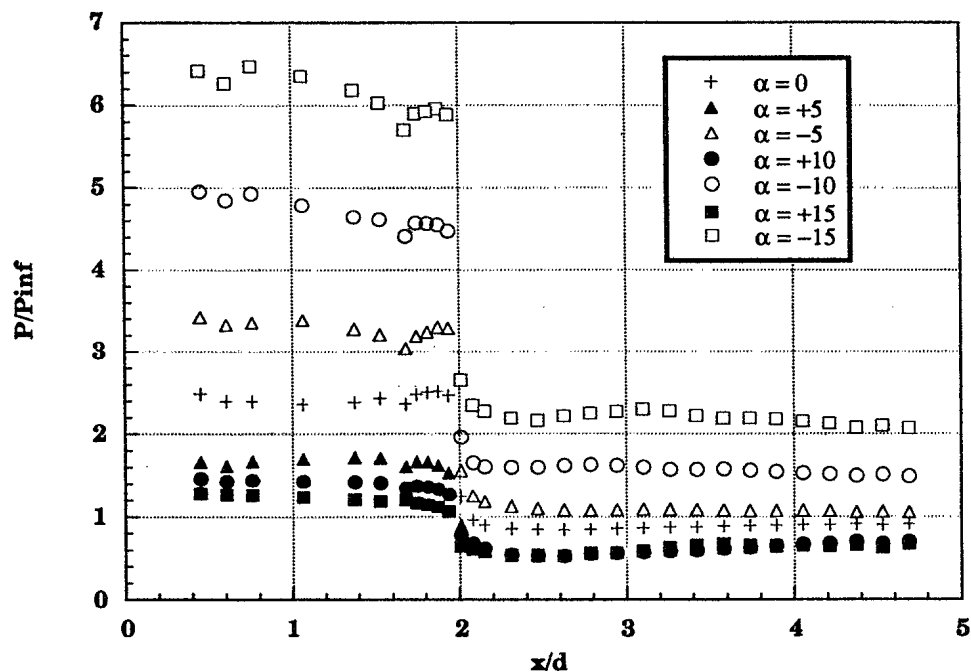
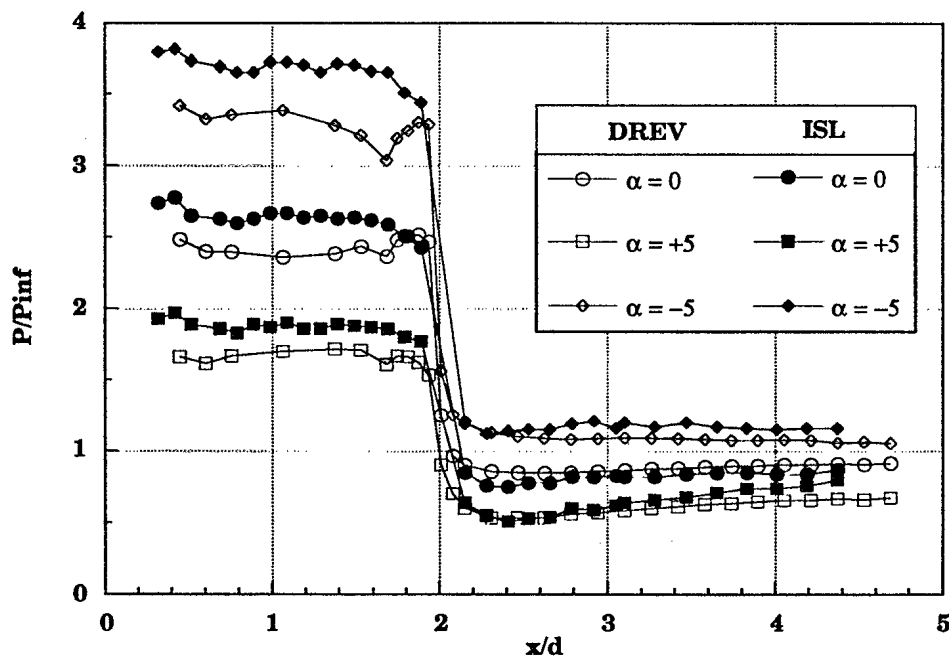


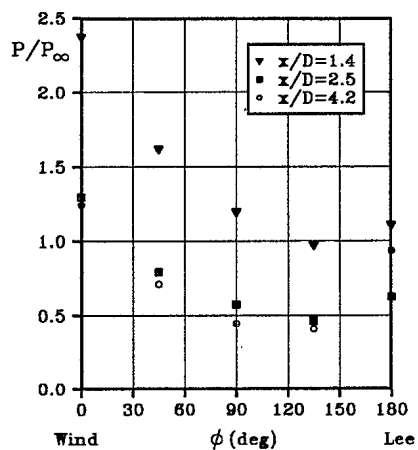
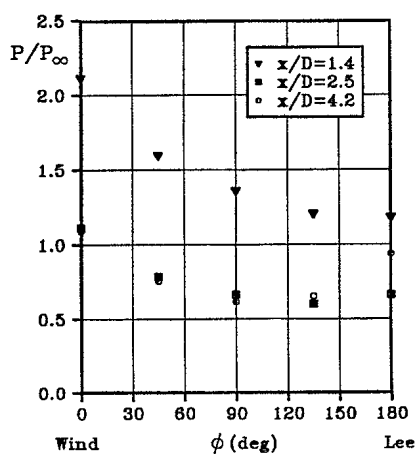
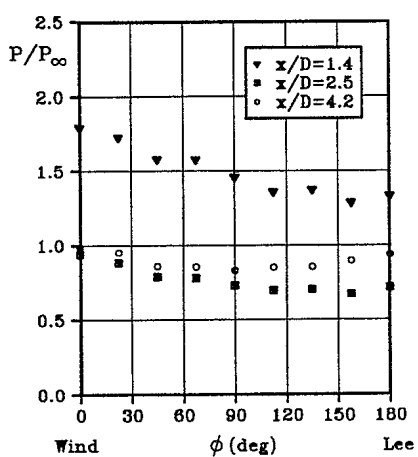
FIGURE 9 - Pressure distributions along the forebody at  $M = 2$   
(Comparison between ISL and DREV)

UNCLASSIFIED

FIGURE 10 - Pressure distributions along the forebody at  $M = 4$ FIGURE 11 - Pressure distributions along the forebody at  $M = 4$   
(Comparison between ISL and DREV)



UNCLASSIFIED

FIGURE 12 - Circumferential surface pressure distributions at  $M = 2$ a)  $\alpha = +5^\circ$ b)  $\alpha = +10^\circ$ c)  $\alpha = +15^\circ$

UNCLASSIFIED

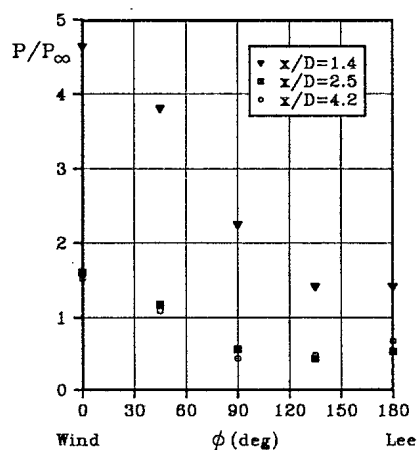
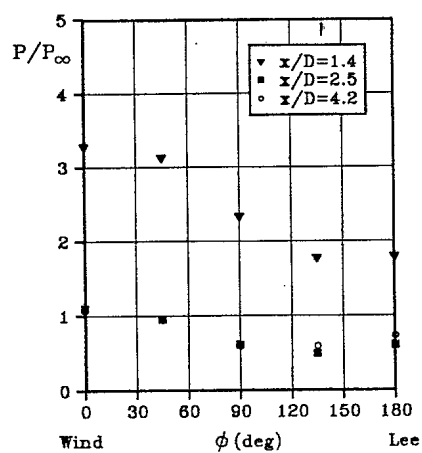
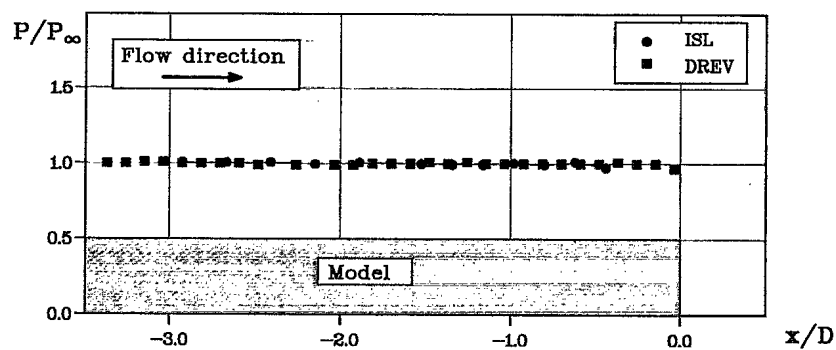
FIGURE 13 - Circumferential surface pressure distributions at  $M = 4$ a)  $\alpha = +5^\circ$ b)  $\alpha = +15^\circ$ 

FIGURE 14 - Pressure distributions along the afterbody (up stream sting)



UNCLASSIFIED

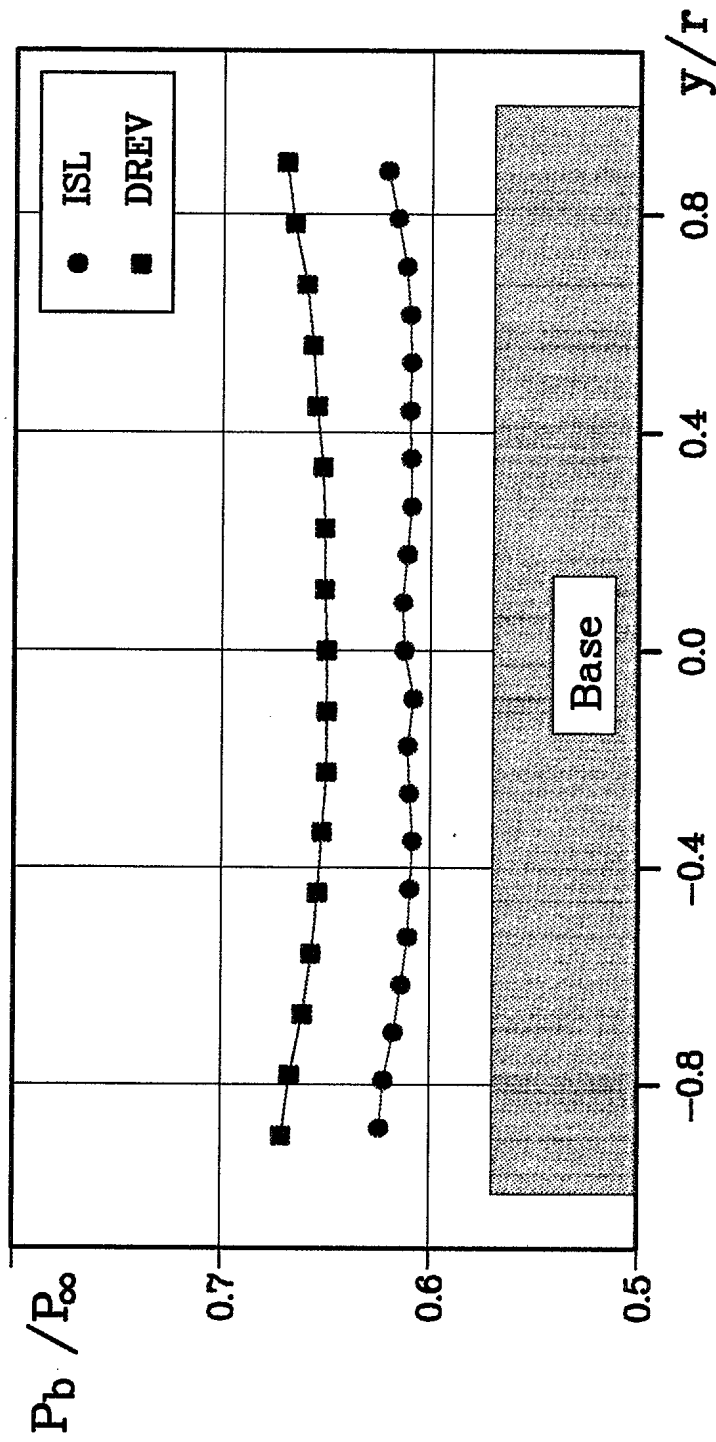
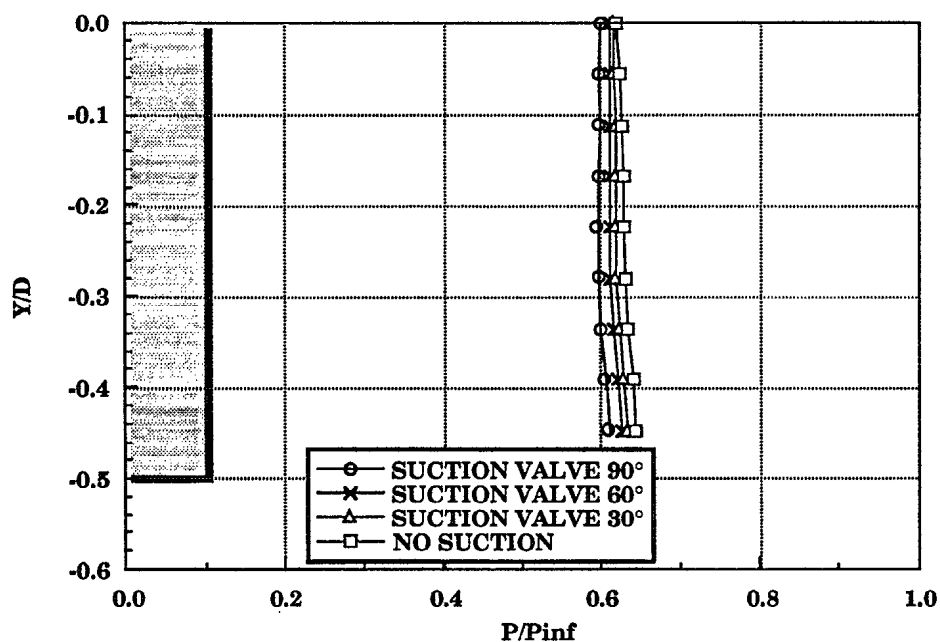


FIGURE 15 - Base pressure distribution

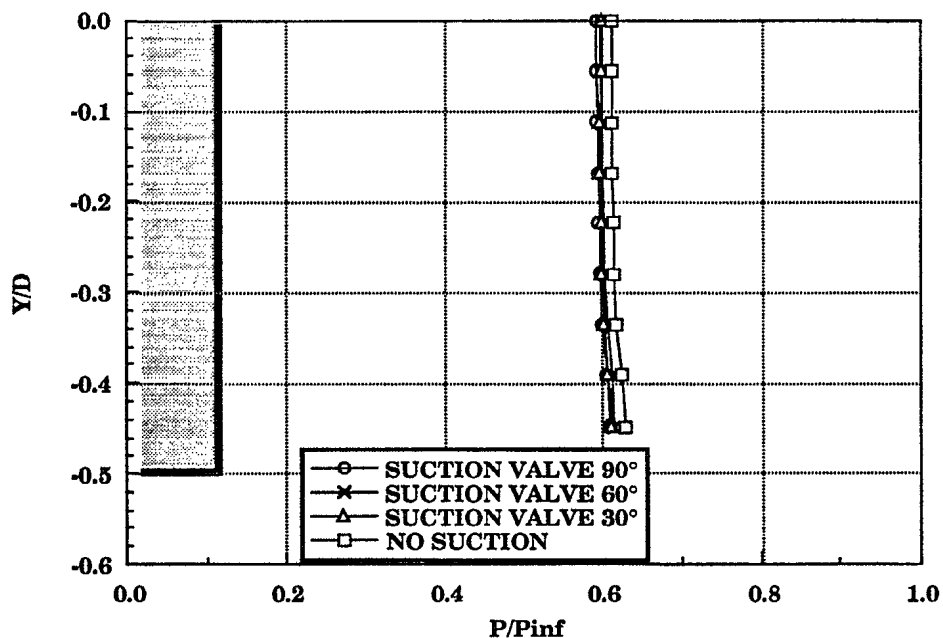
a) Comparison between ISL and DREV



UNCLASSIFIED



b) Effect of boundary layer suction on base pressure distribution  
(Smooth afterbody)



c) Effect of boundary layer suction on base pressure distribution  
(Sand paper collar)

UNCLASSIFIED

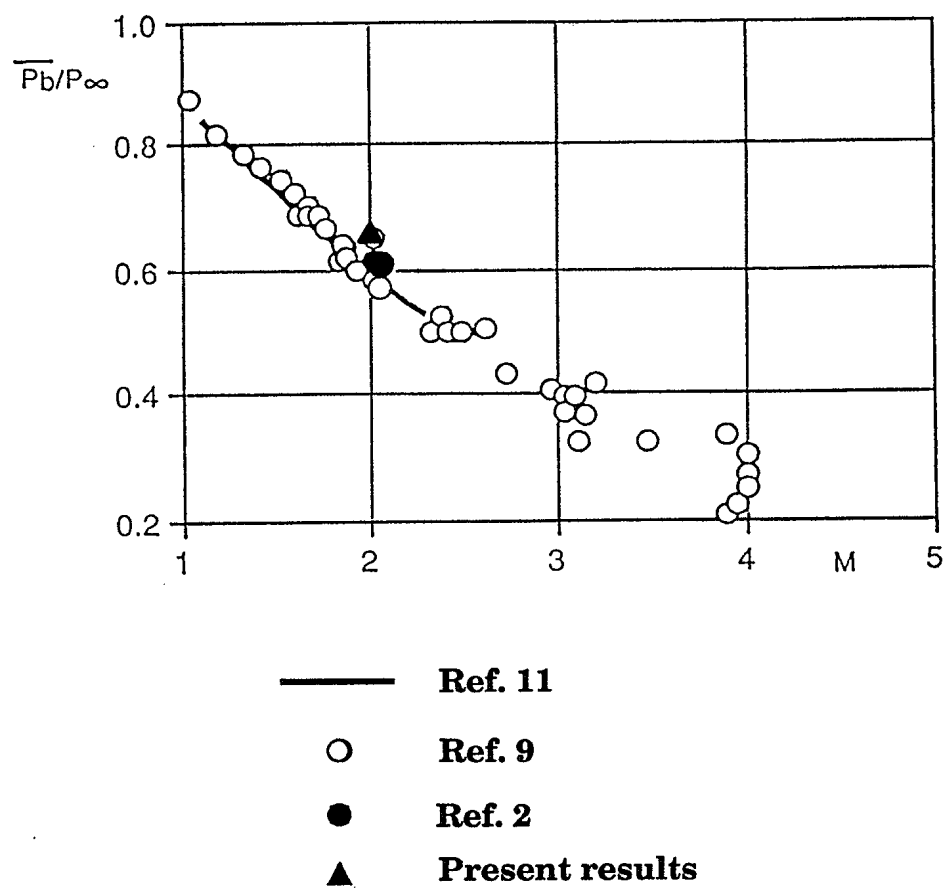


FIGURE 16 - Base pressure vs. Mach number

UNCLASSIFIED

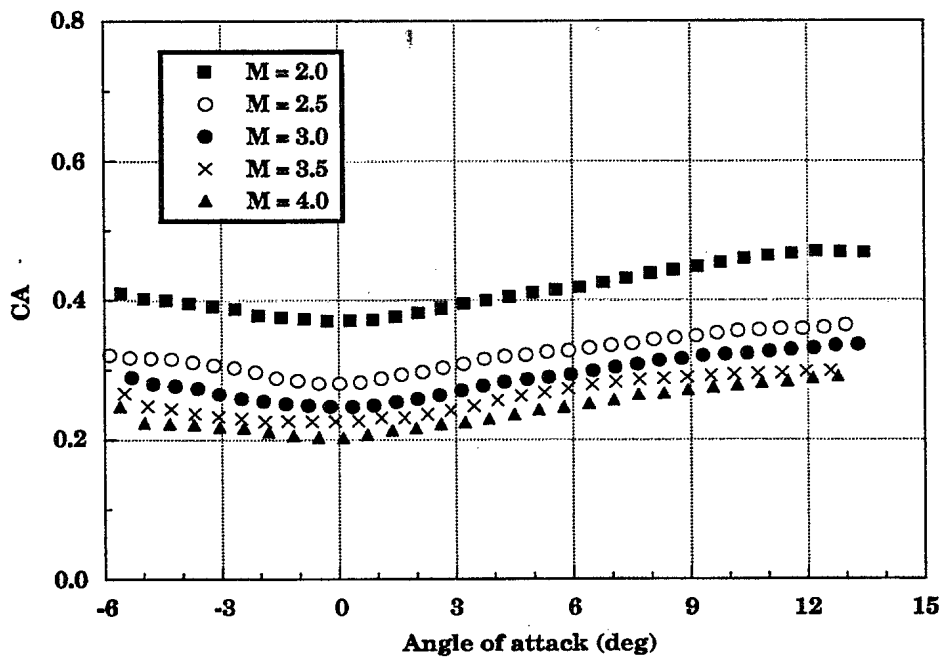
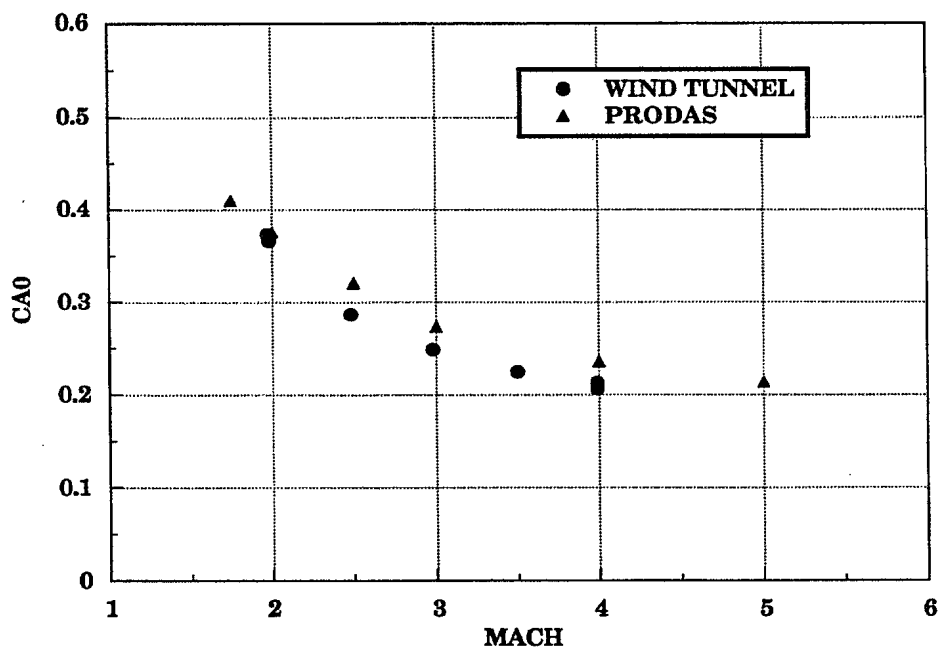


FIGURE 17 - Axial force coefficient (Model A)

a) Versus angle of attack and Mach number



b) CA0 vs. Mach number



UNCLASSIFIED

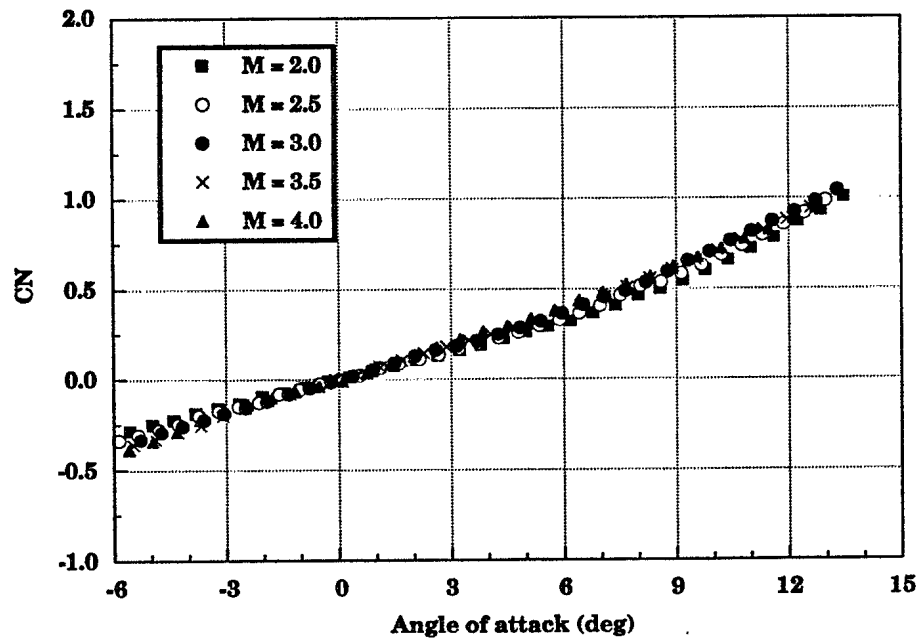
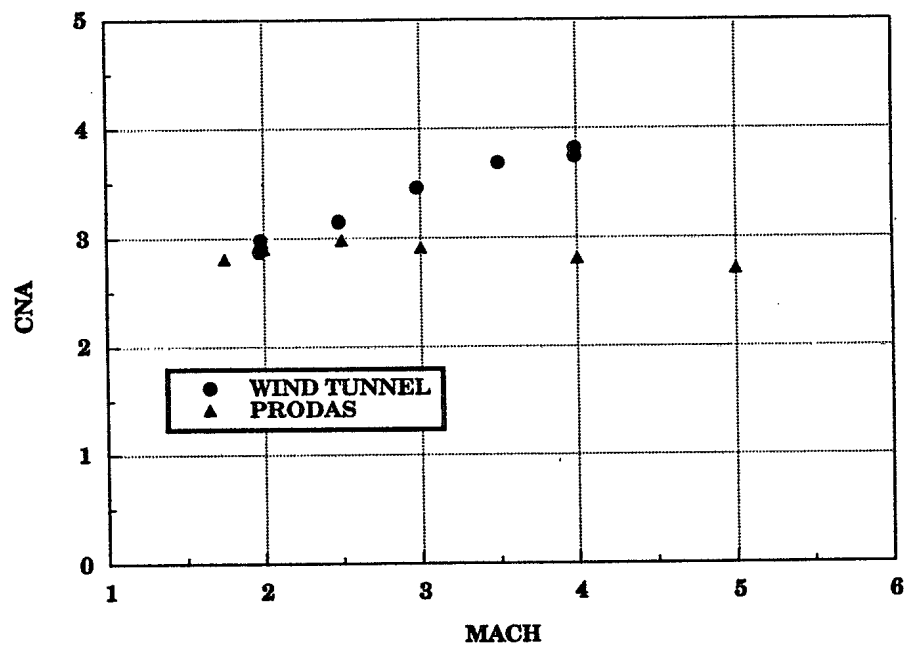


FIGURE 18 - Normal force coefficient (Model A)

a) Versus angle of attack and Mach number



b) Normal force coefficient slope vs. Mach number

UNCLASSIFIED

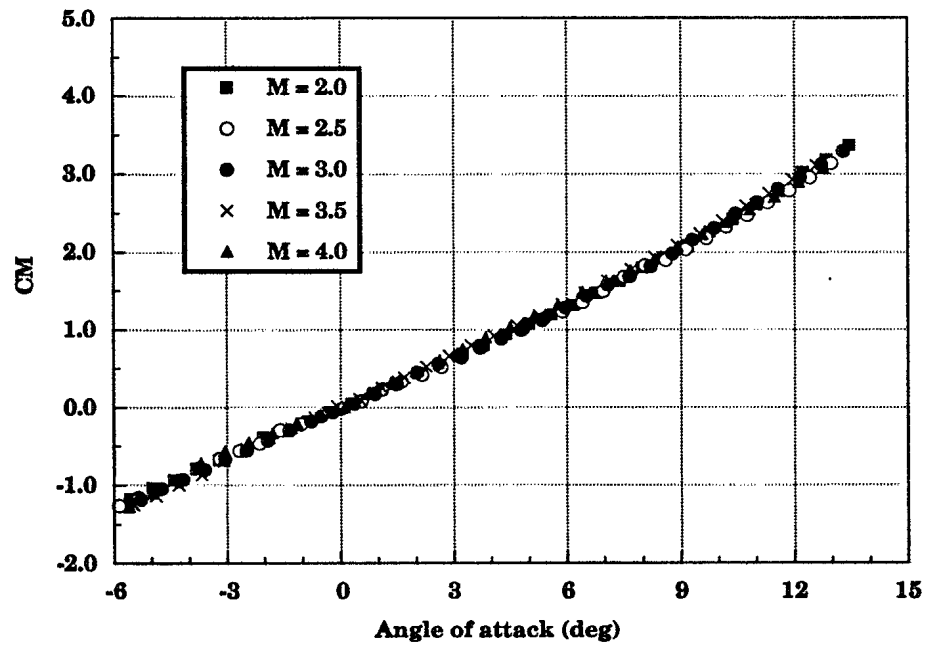
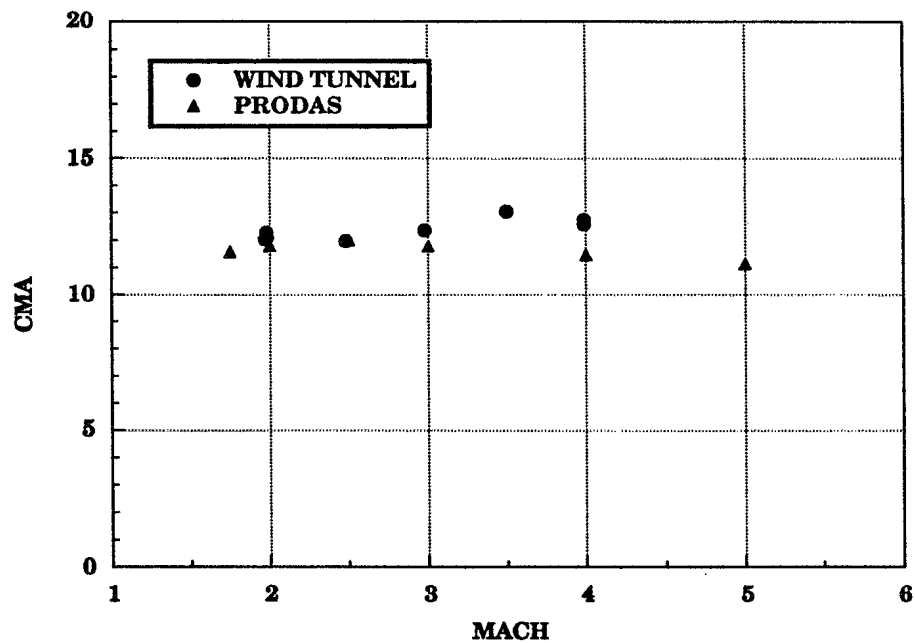


FIGURE 19 - Pitching moment coefficient about the base (Model A)

a) Versus angle of attack and Mach number



b) Pitching moment coefficient slope vs. Mach number

UNCLASSIFIED

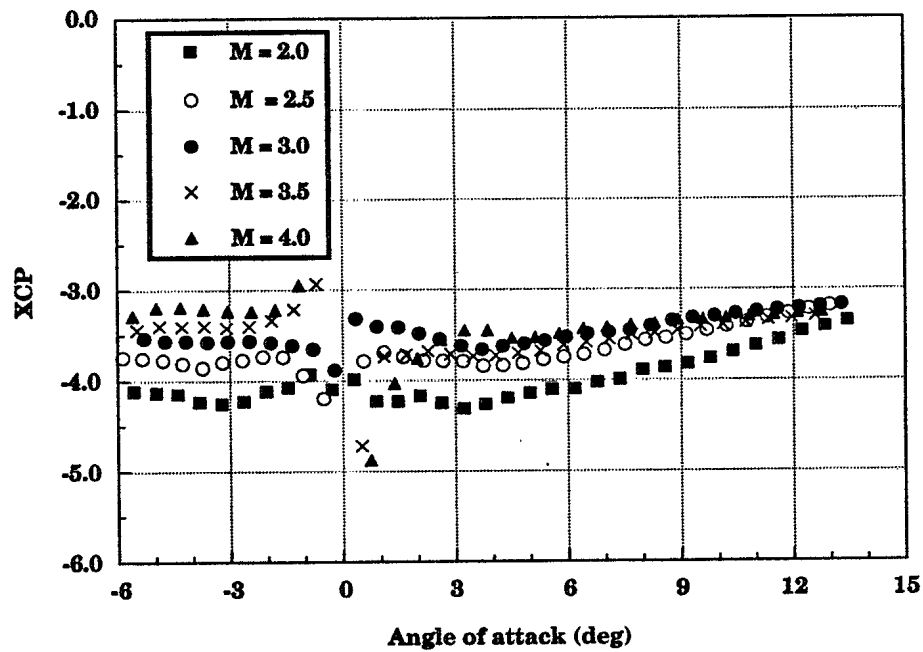
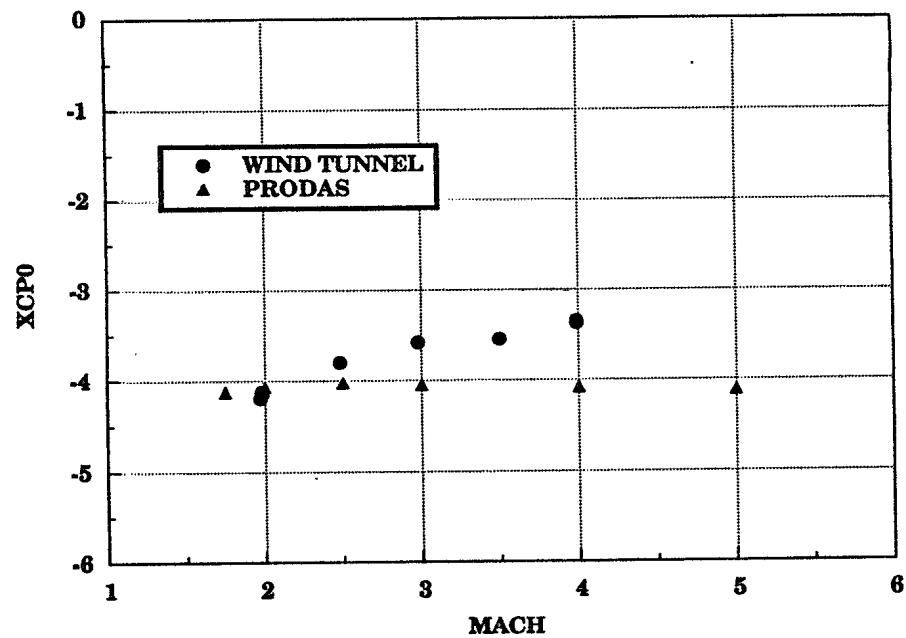


FIGURE 20 - Center of pressure location (Model A)

a) Versus angle of attack and Mach number

b) Center of pressure location at  $\alpha = 0^\circ$  vs. Mach number

UNCLASSIFIED

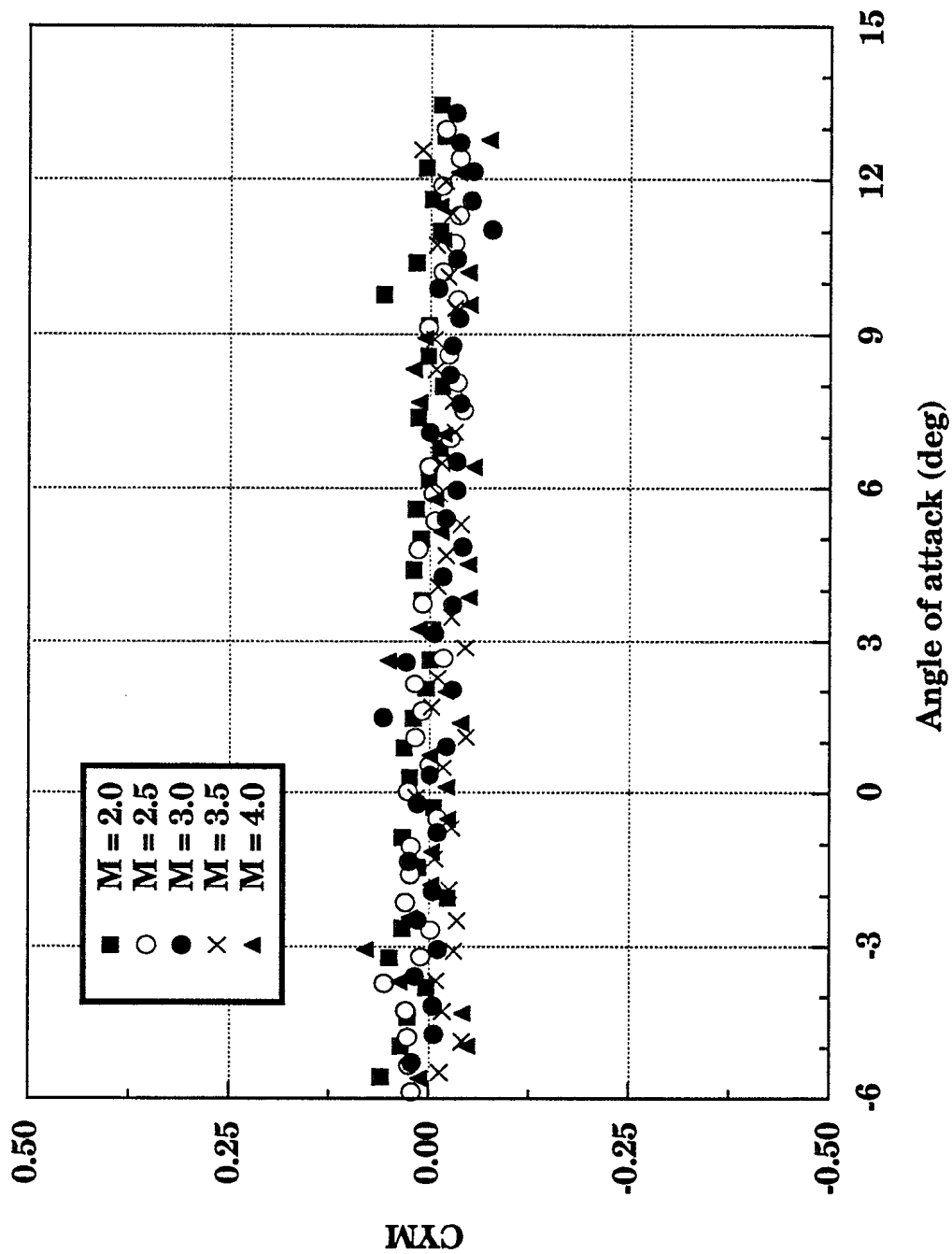
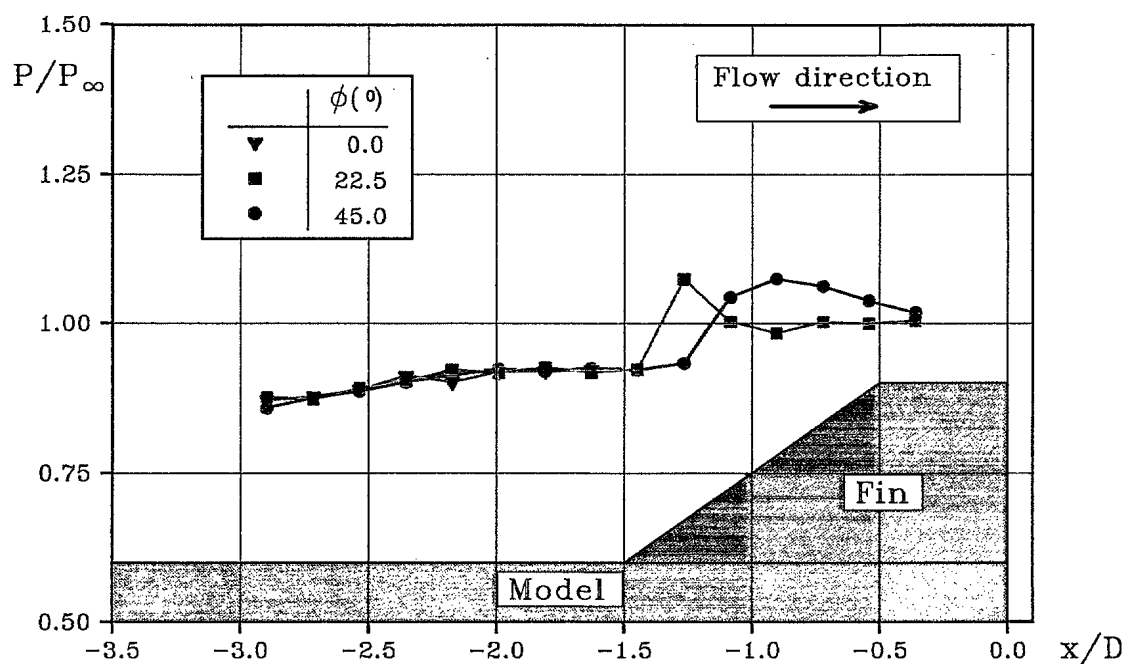
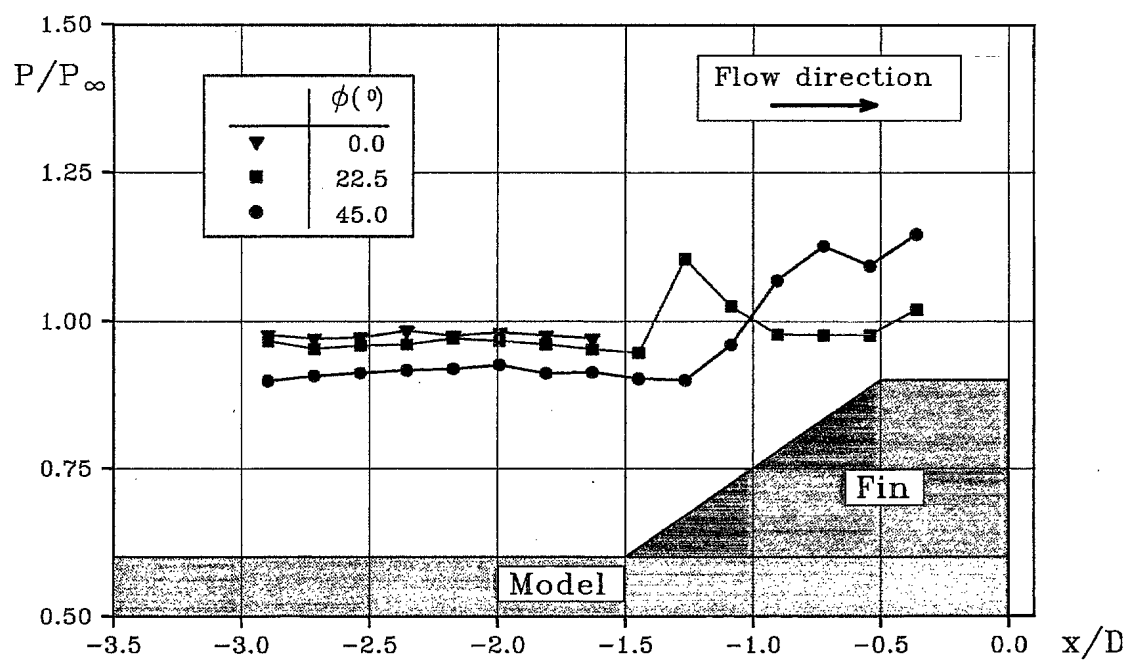
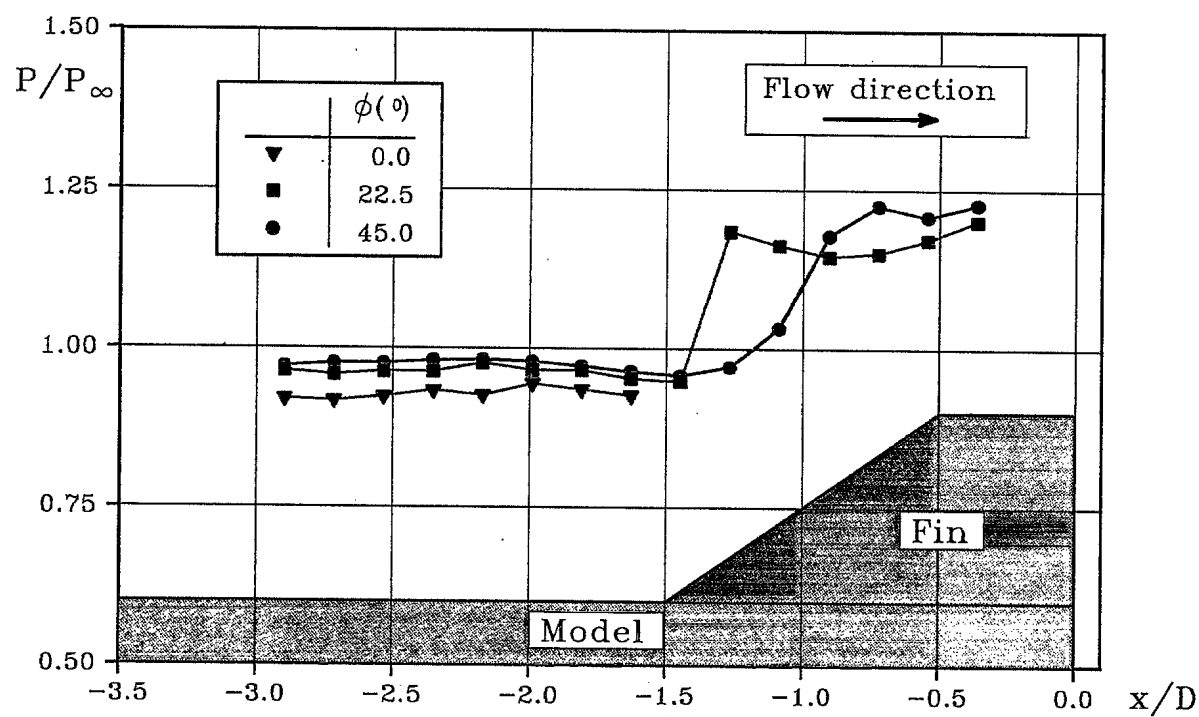
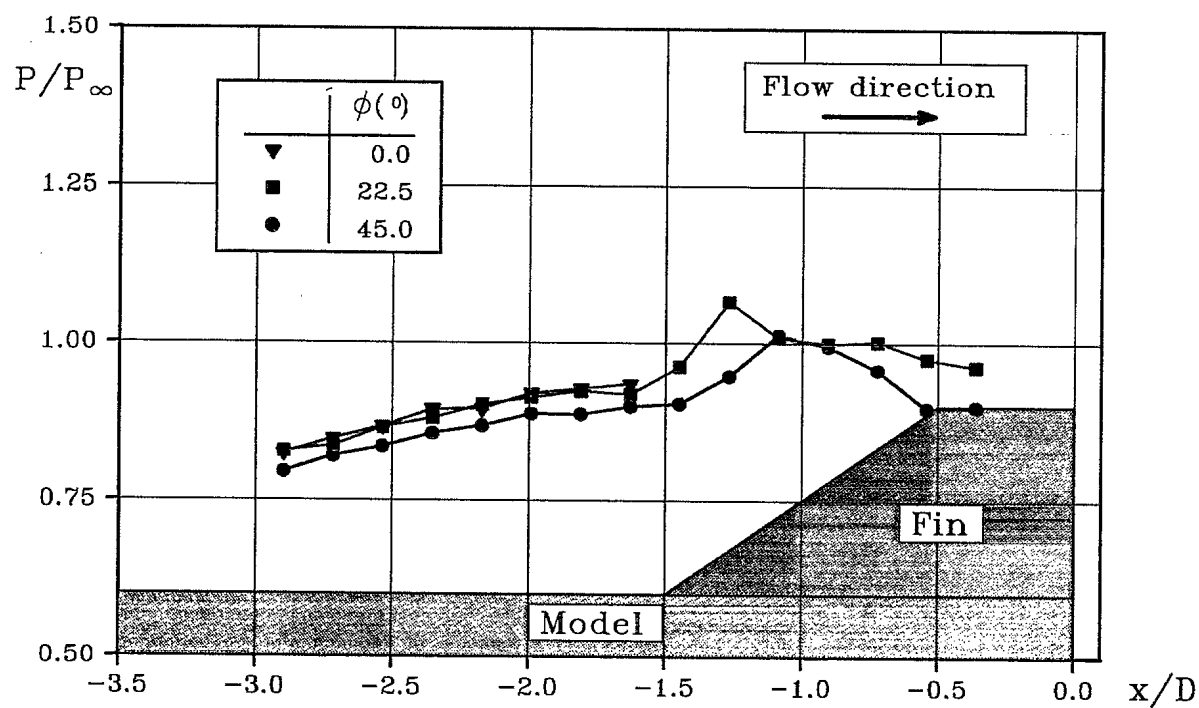


FIGURE 21 - Yawing moment coefficient (Model A) versus angle of attack and Mach number

UNCLASSIFIED

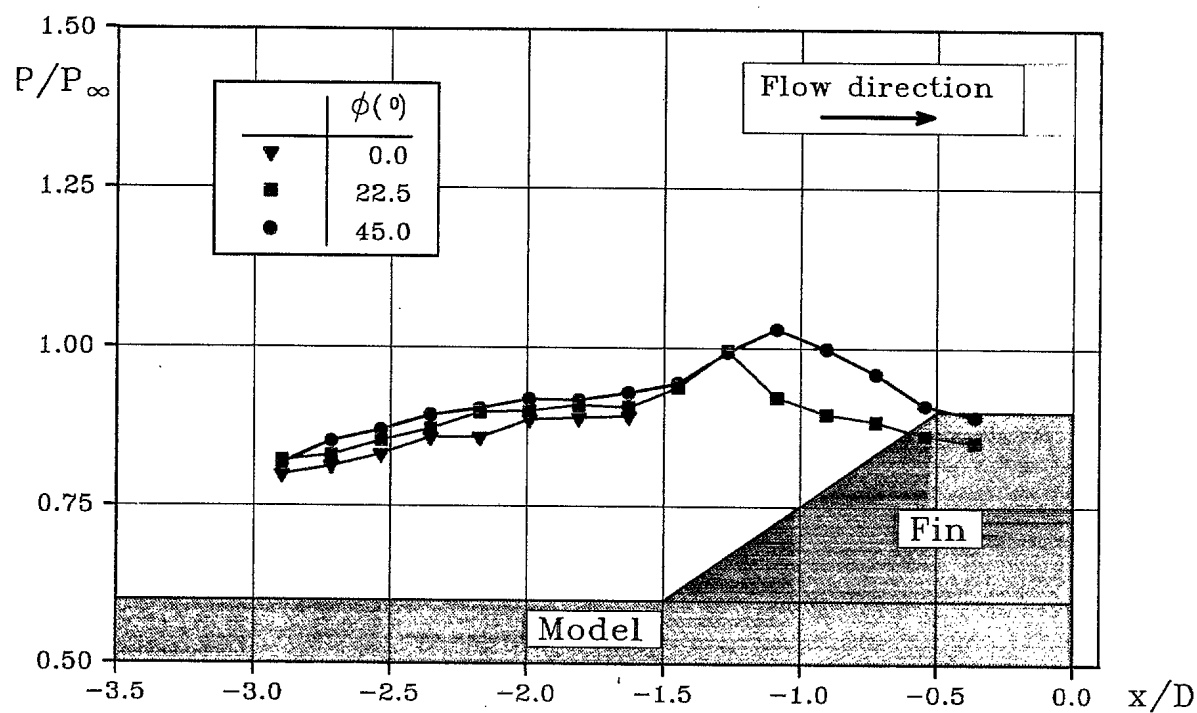
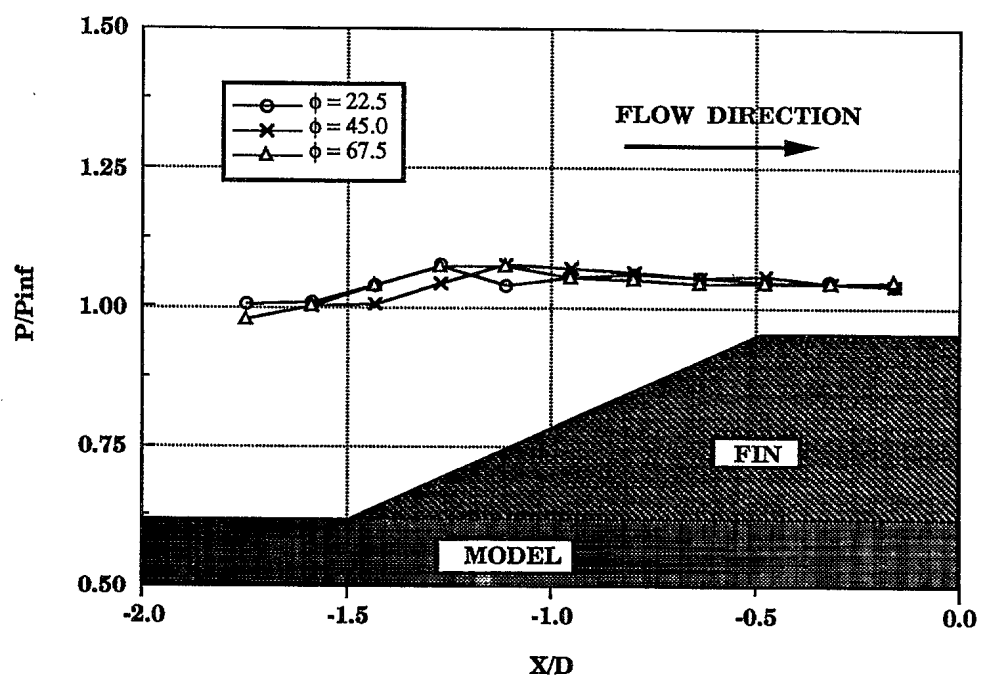
FIGURE 22 - Pressure distribution along afterbody at  $M = 2.0$  (ISL WT)a)  $\alpha = 0^\circ$   $\phi = 0^\circ$ b)  $\alpha = +5^\circ$   $\phi = 0^\circ$

UNCLASSIFIED

c)  $\alpha = +5^\circ$   $\phi = +45^\circ$ d)  $\alpha = -5^\circ$   $\phi = 0^\circ$



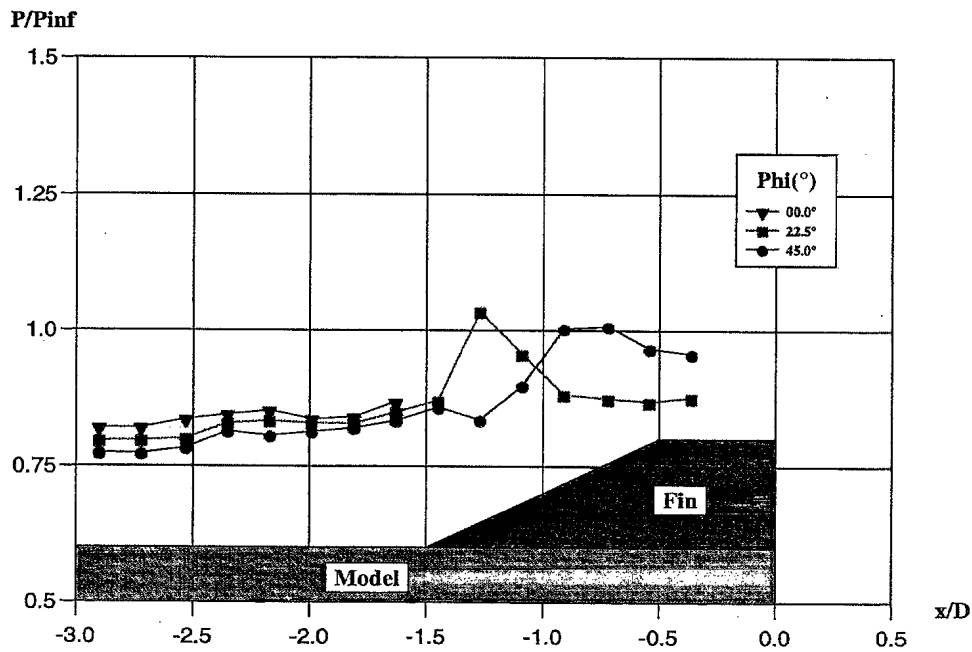
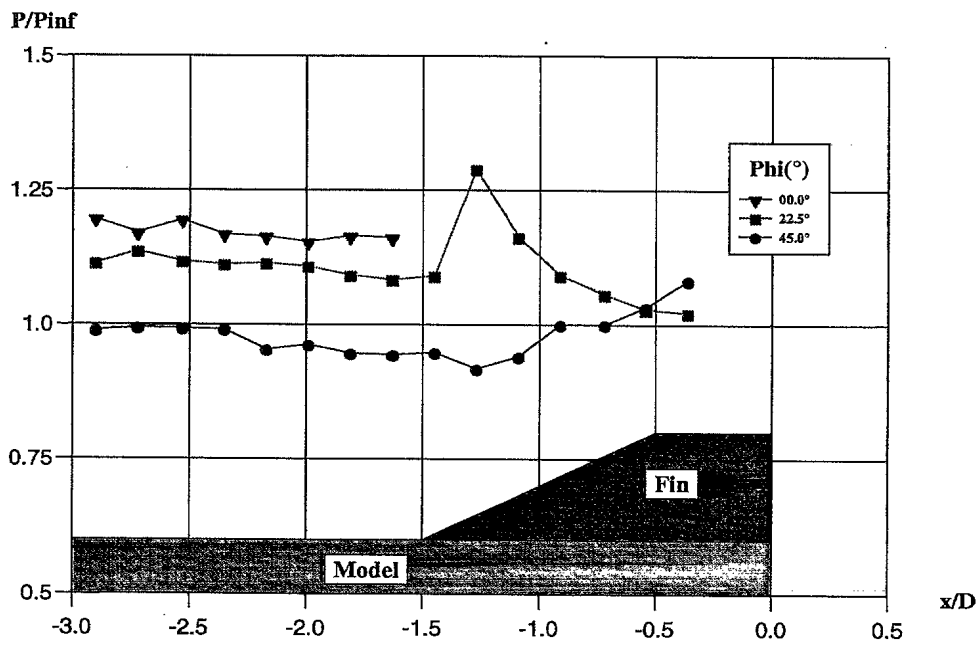
UNCLASSIFIED

e)  $\alpha = -5^\circ$   $\phi = +45^\circ$ f) DREV results on up stream sting for  $\alpha = 0^\circ$  and  $\phi = 0^\circ$



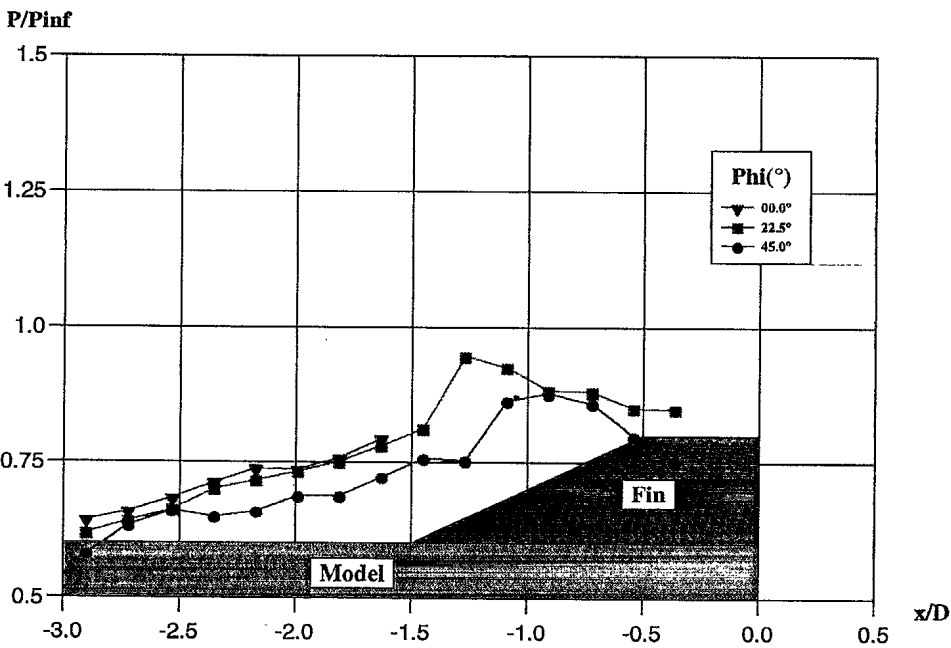


UNCLASSIFIED

FIGURE 23 - Pressure distribution along afterbody at  $M = 4.0$  (ISL WT)a)  $\alpha = 0^\circ$      $\phi = 0^\circ$ b)  $\alpha = -5^\circ$      $\phi = 0^\circ$



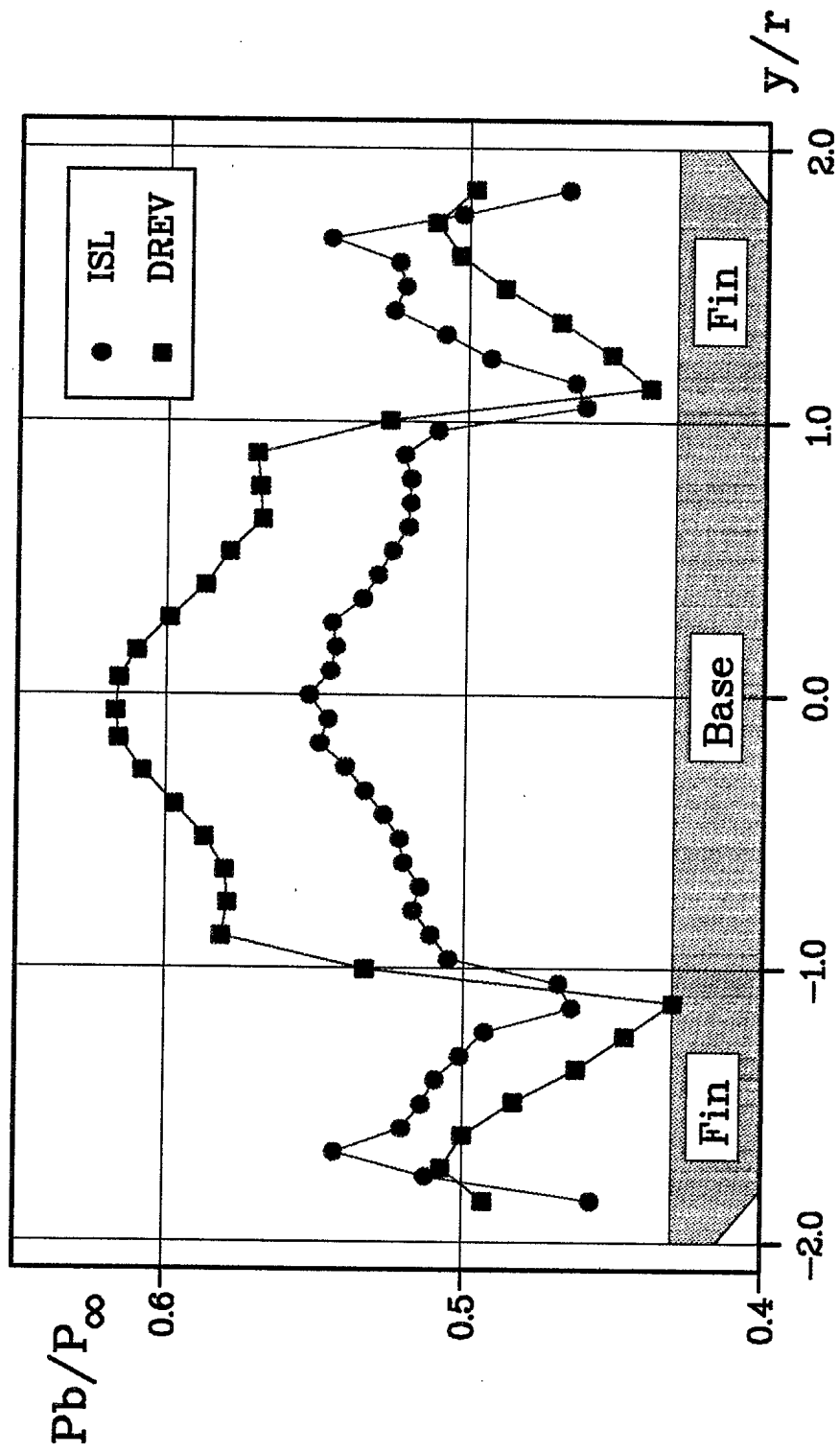
UNCLASSIFIED



c)  $\alpha = +5^\circ$      $\phi = 0^\circ$

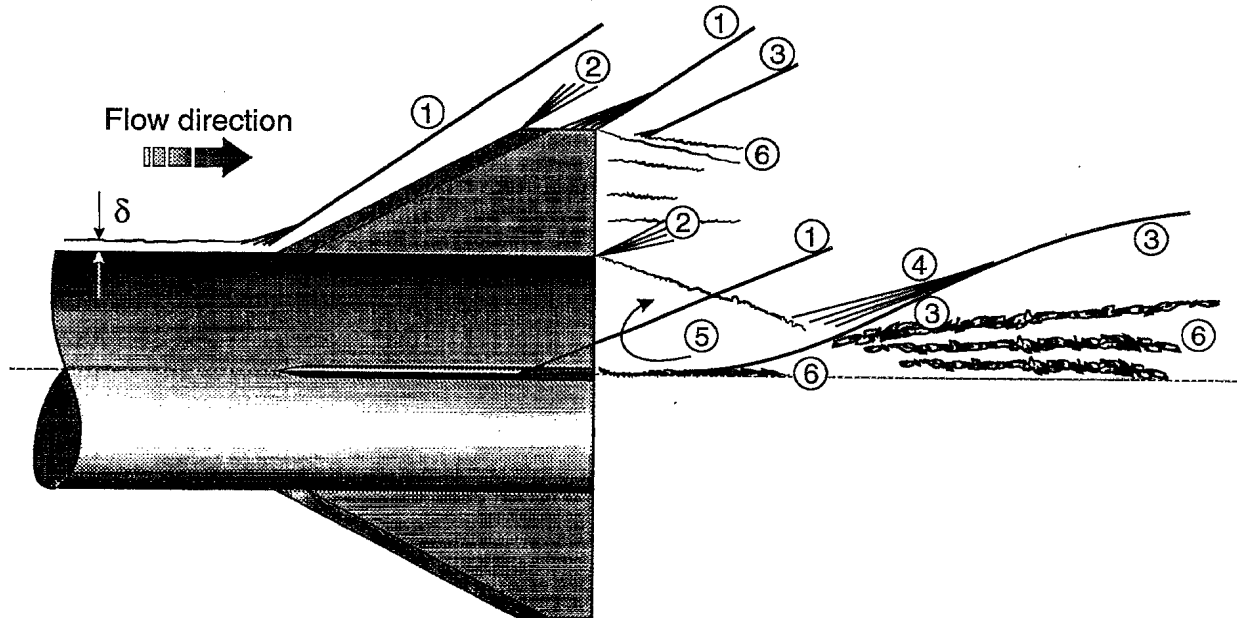


UNCLASSIFIED

FIGURE 24 - Base pressure distribution at  $M = 2$



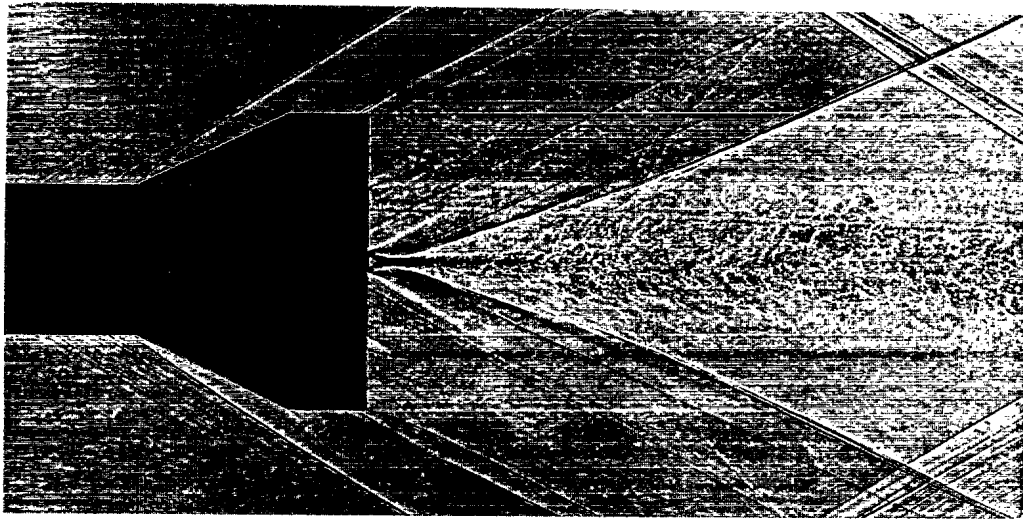
UNCLASSIFIED



- |                            |                                  |
|----------------------------|----------------------------------|
| ① Fin recompression shock  | ④ Compression wavelets           |
| ② Expansion fan            | ⑤ Base flow recirculating region |
| ③ Wake recompression shock | ⑥ Near and far wake flow         |

FIGURE 25 - Afterbody base flow

a) Schematic of flow



b) Shadowgraph of flow



UNCLASSIFIED

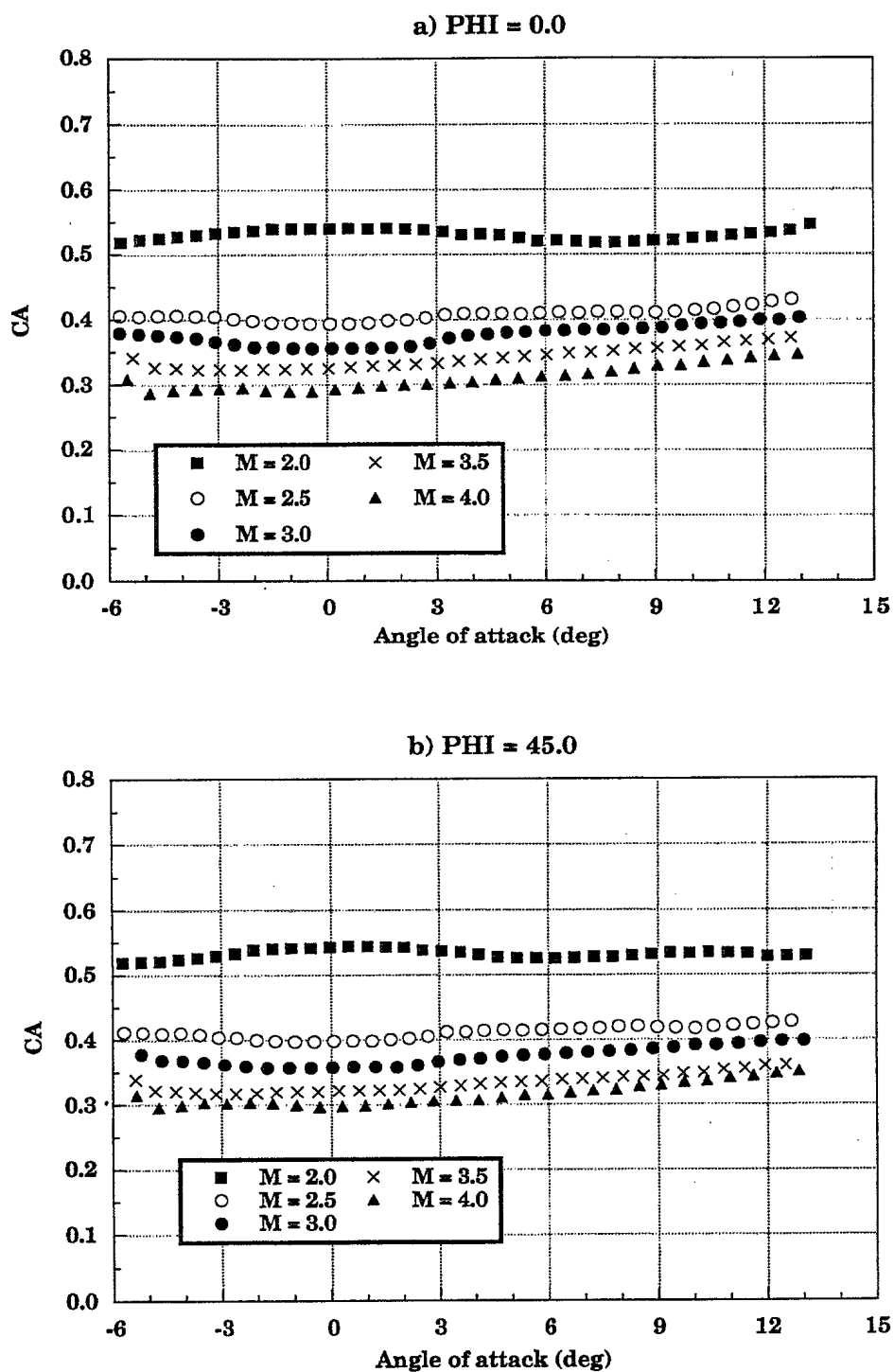
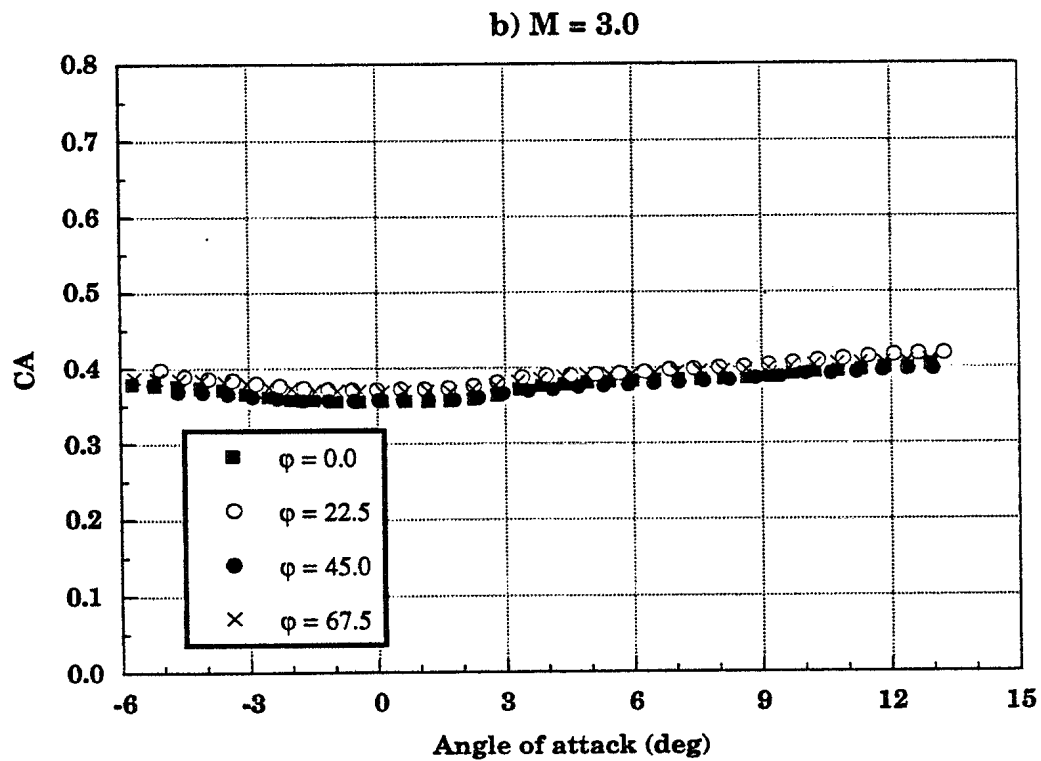
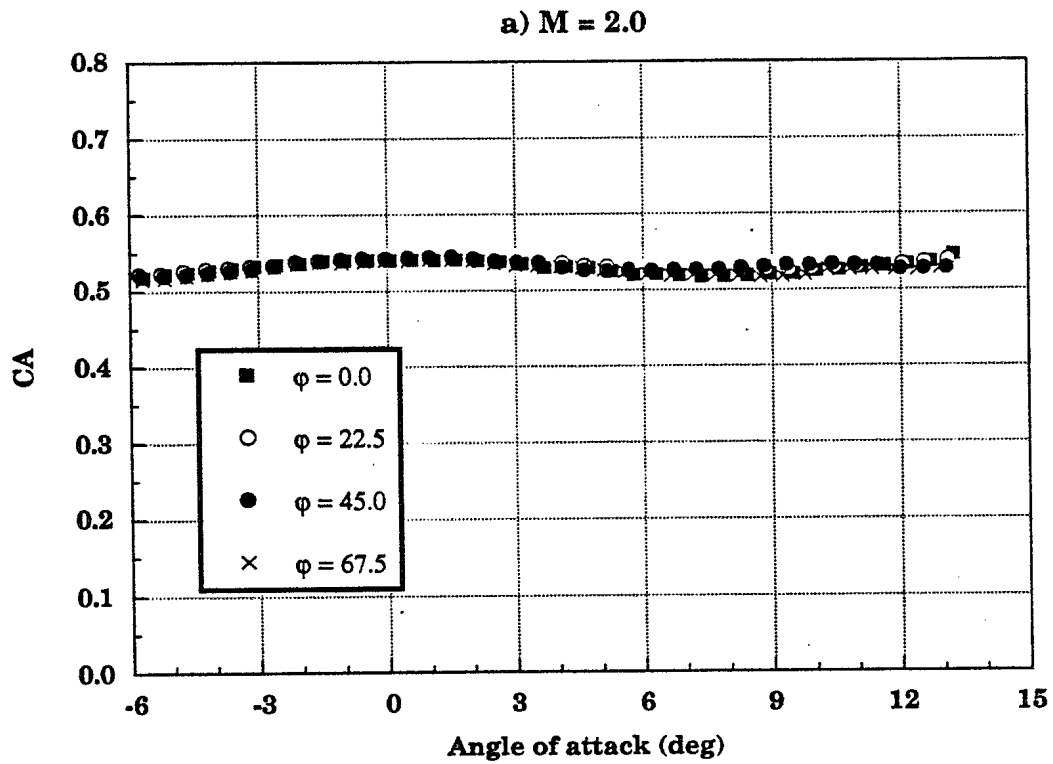


FIGURE 26 - Mach number effects on the axial force coefficient (Model B)

a)  $\phi = 0^\circ$ b)  $\phi = 45^\circ$

UNCLASSIFIED



UNCLASSIFIED

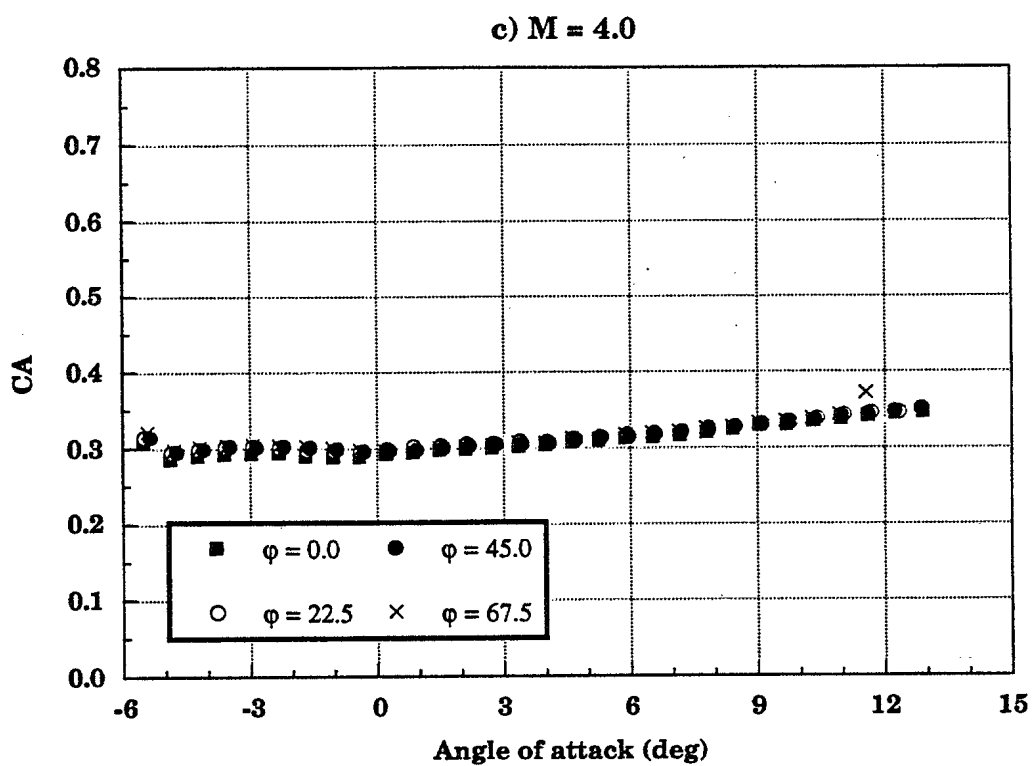


FIGURE 27 - Roll angle effects on the axial force coefficient (Model B)

a)  $M = 2.0$ b)  $M = 3.0$ c)  $M = 4.0$

UNCLASSIFIED

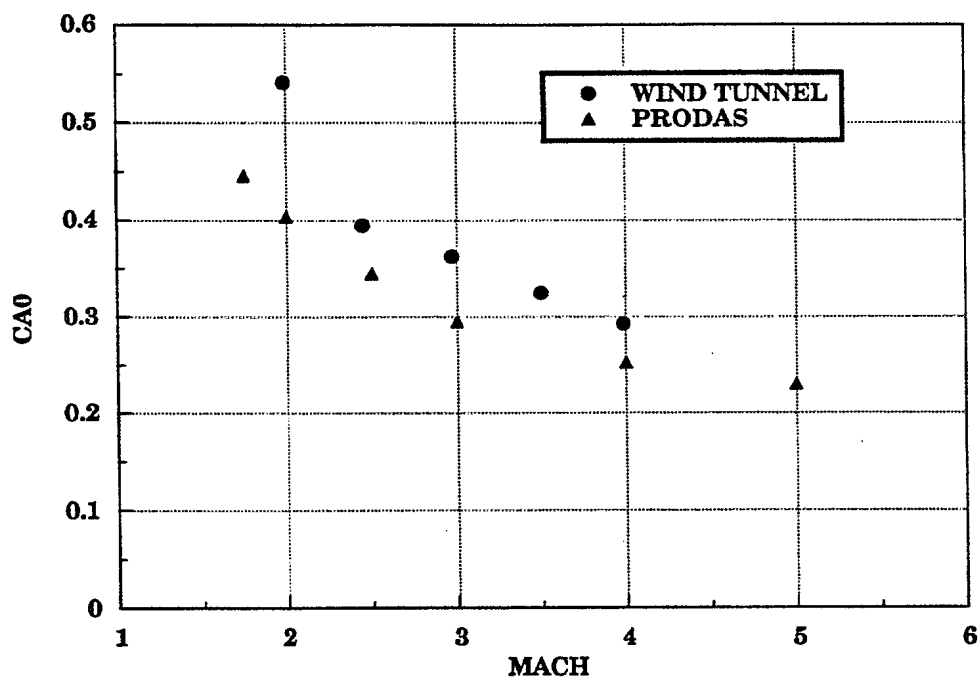


FIGURE 28 - Axial force coefficient vs. Mach number (Model B)

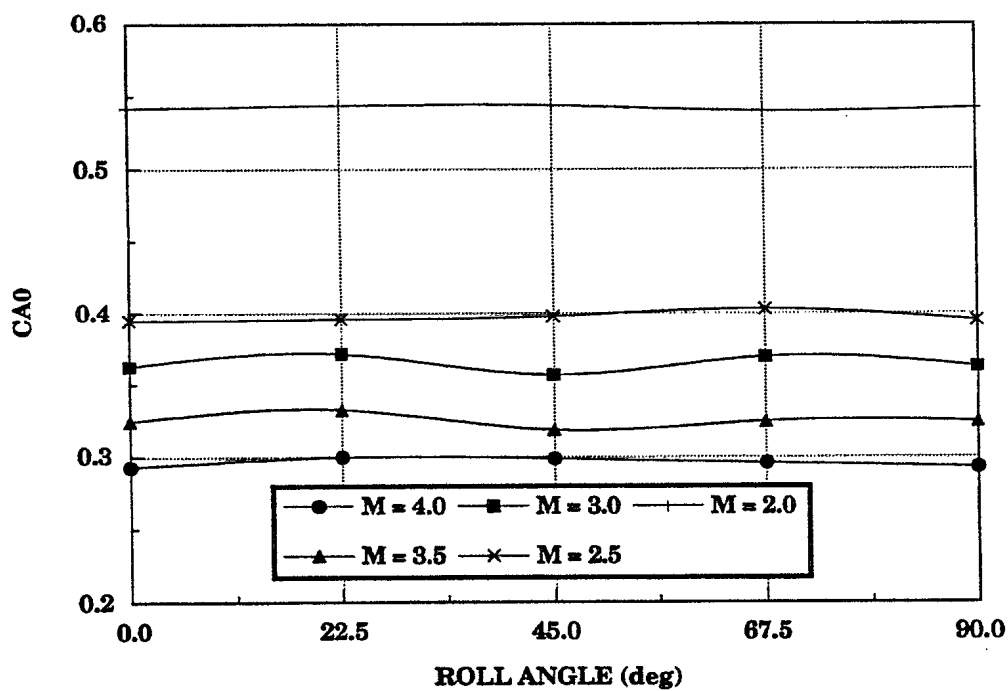


FIGURE 29 - Axial force coefficient vs. roll angle (Model B)

UNCLASSIFIED

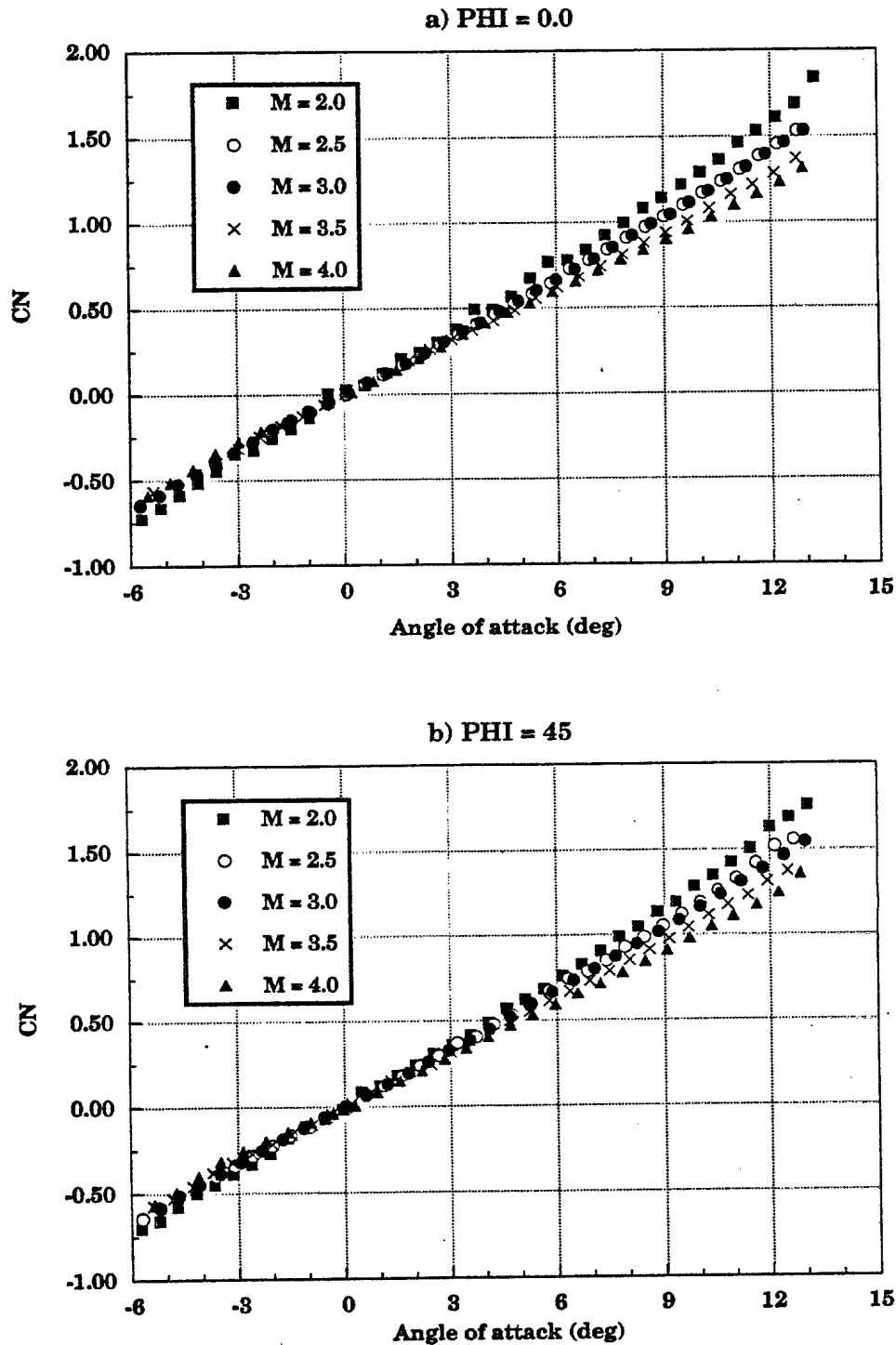
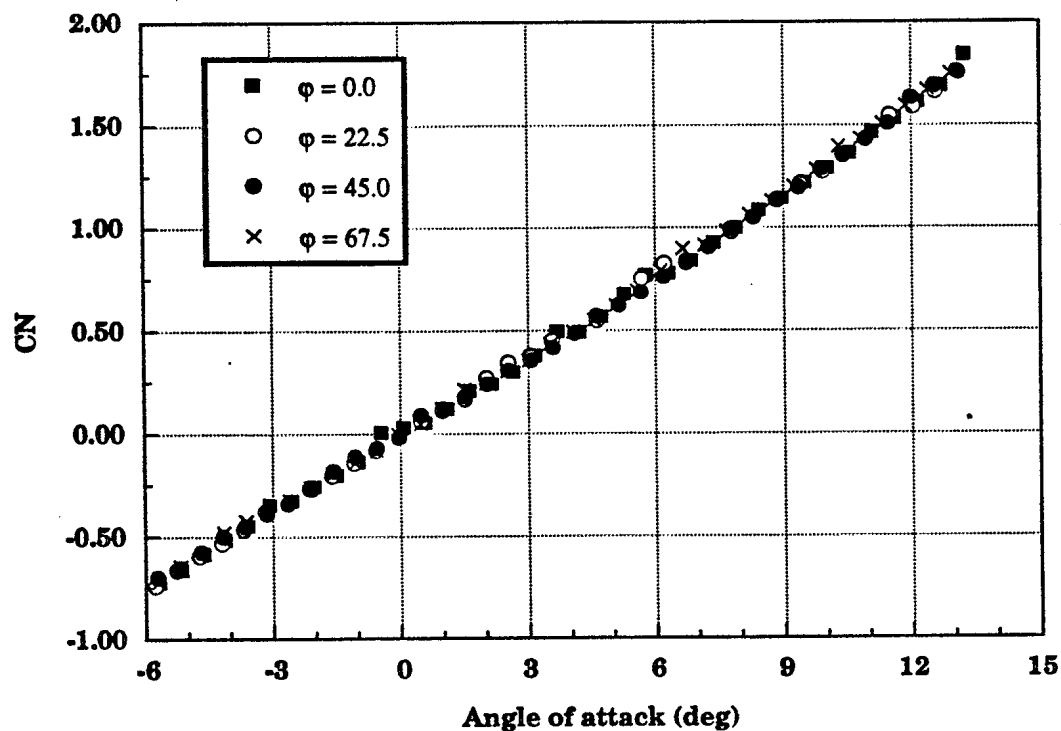
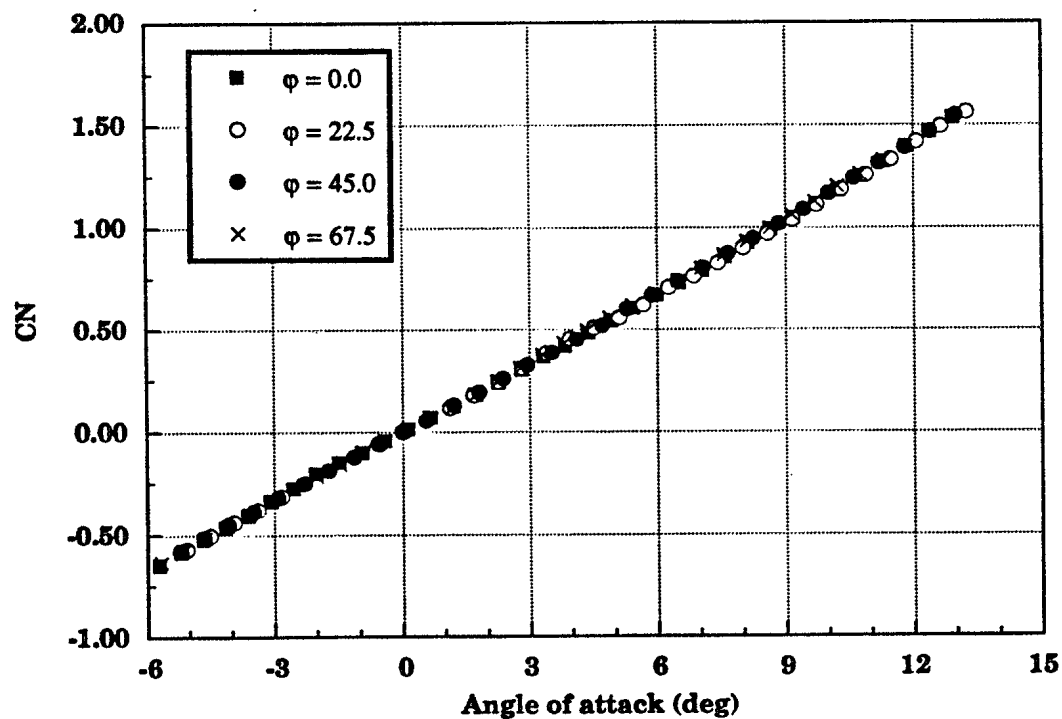


FIGURE 30 - Mach number effects on the normal force coefficient (Model B)

a)  $\phi = 0^\circ$ b)  $\phi = 45^\circ$

UNCLASSIFIED

a)  $M = 2.0$ b)  $M = 3.0$ 

UNCLASSIFIED

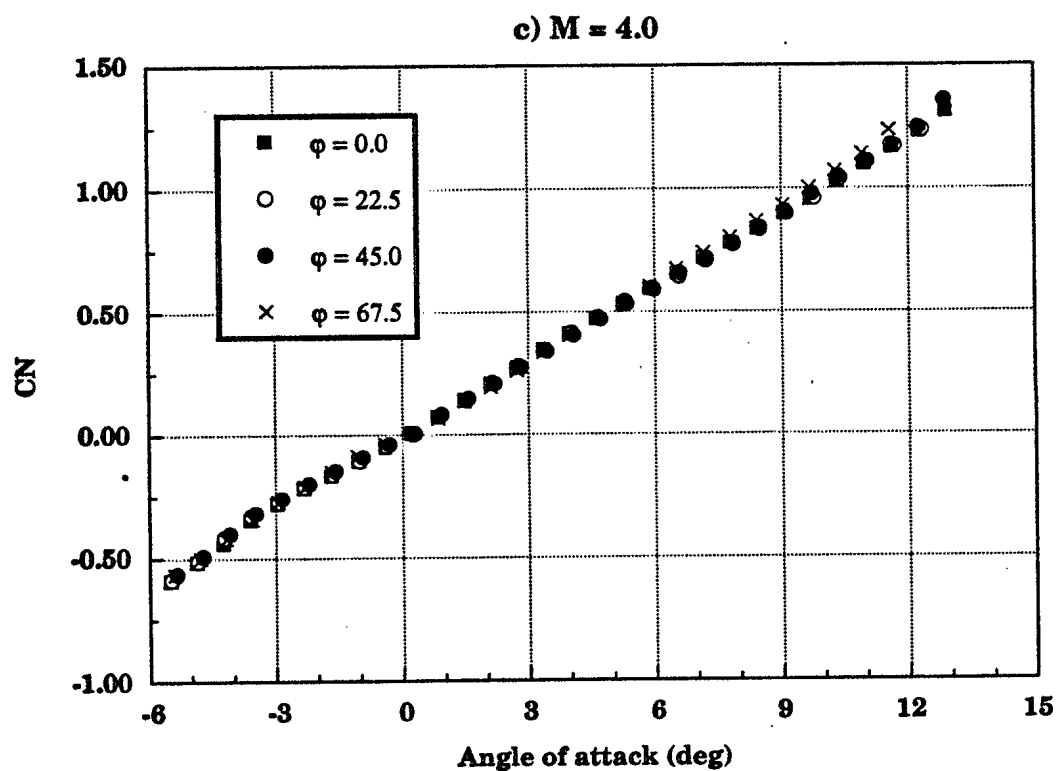


FIGURE 31 - Roll angle effects on the normal force coefficient (Model B)

a)  $M = 2.0$ b)  $M = 3.0$ c)  $M = 4.0$

UNCLASSIFIED

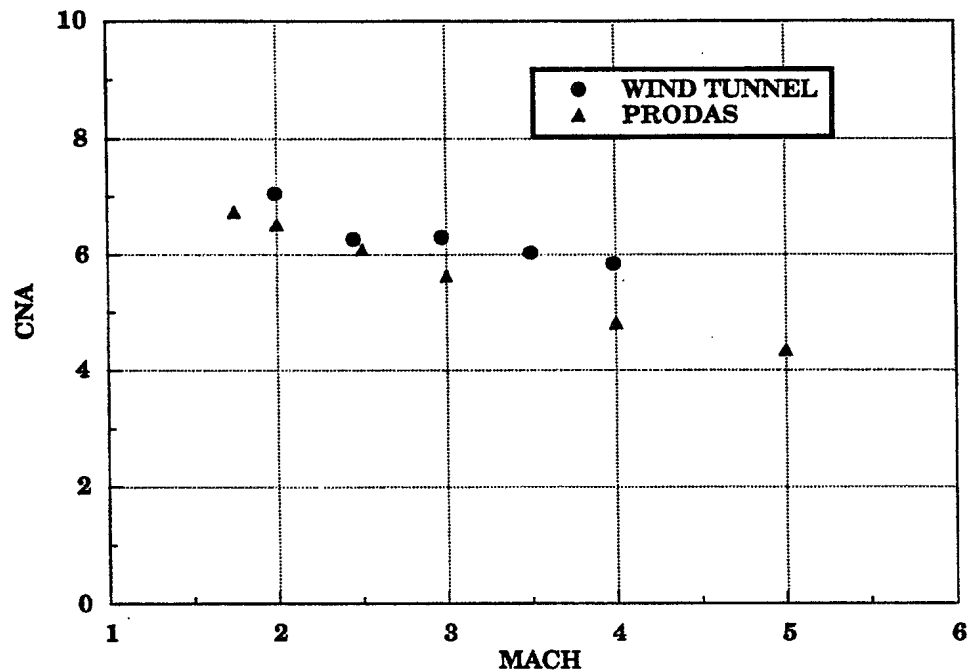


FIGURE 32 - Normal force coefficient slope vs. Mach number (Model B)

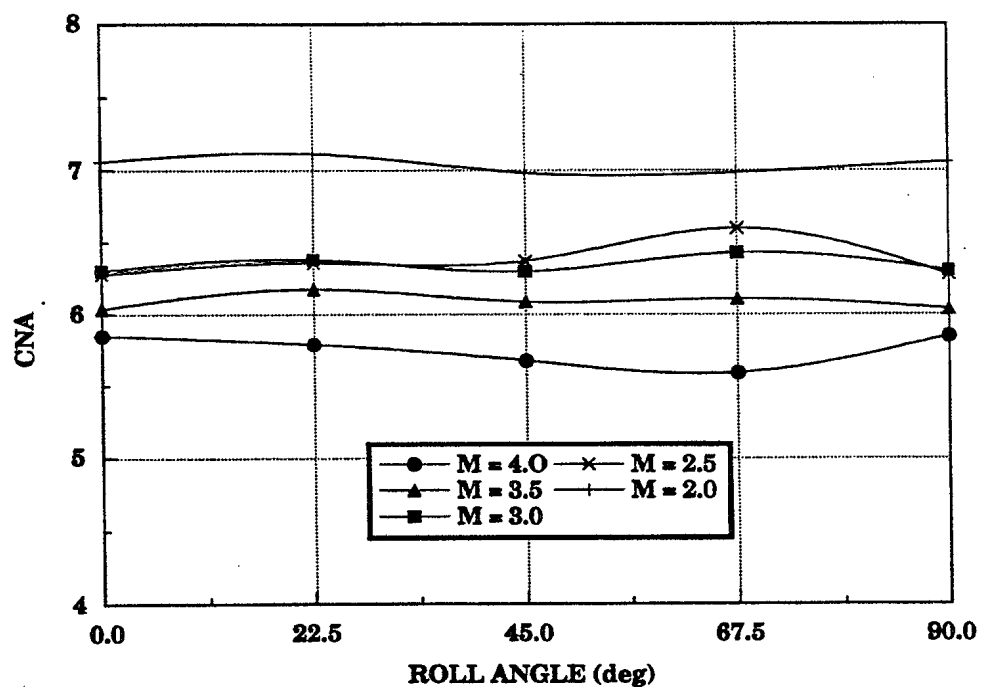


FIGURE 33 - Normal force coefficient slope vs. roll angle (Model B)



UNCLASSIFIED

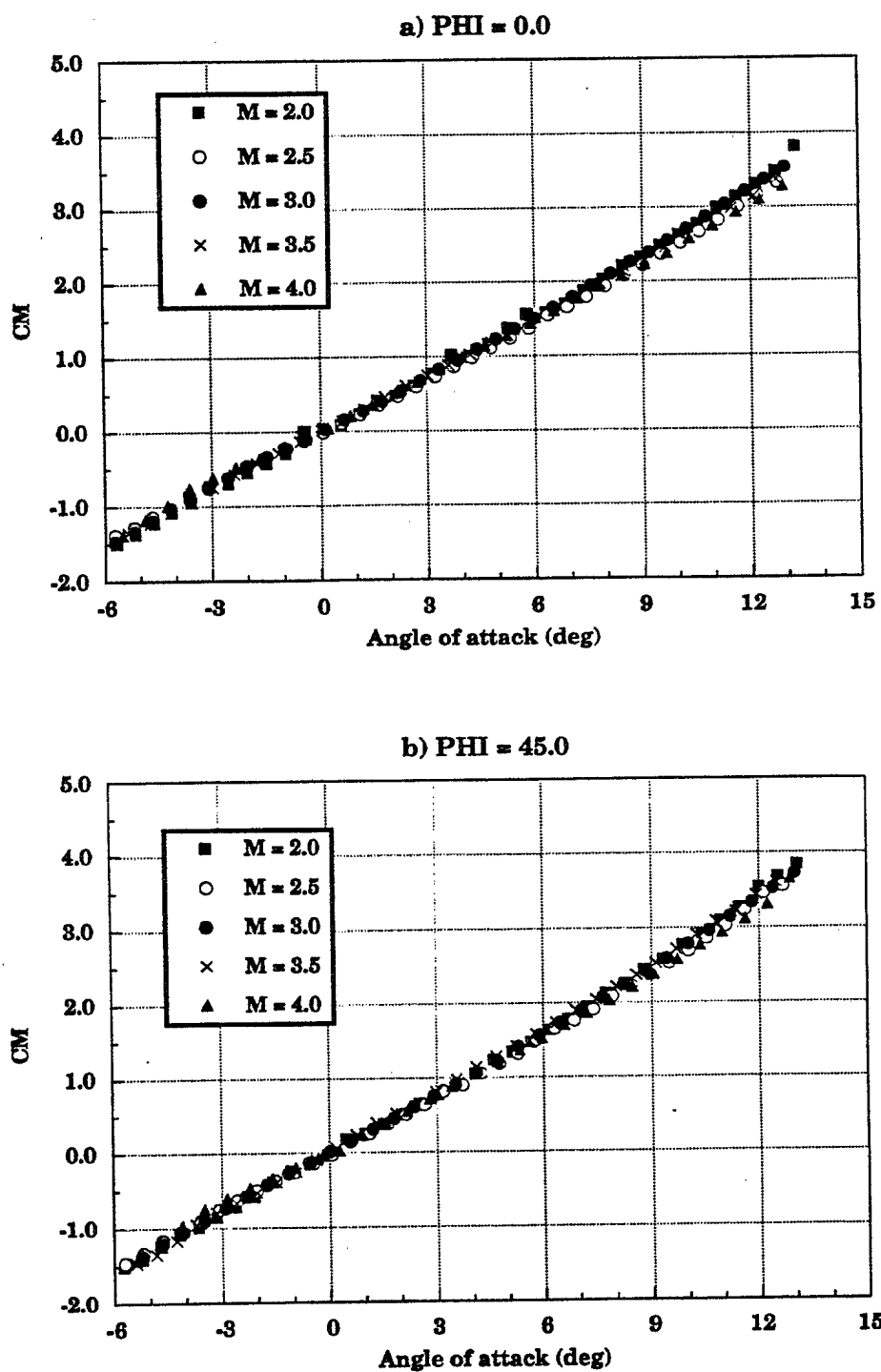
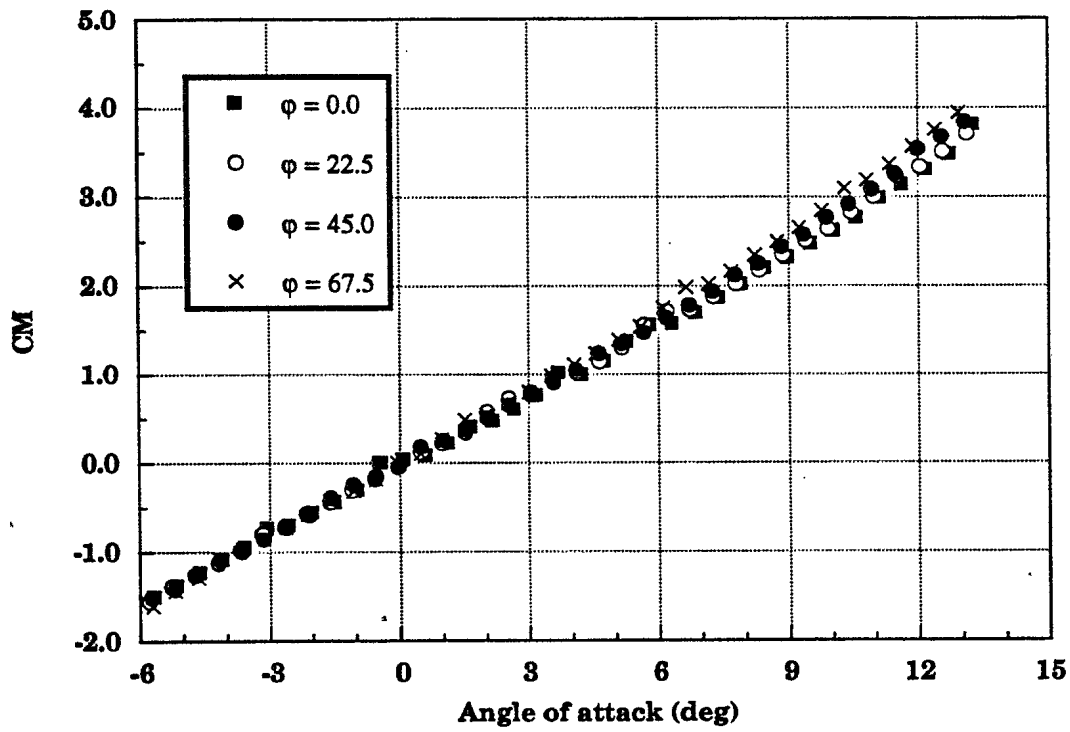
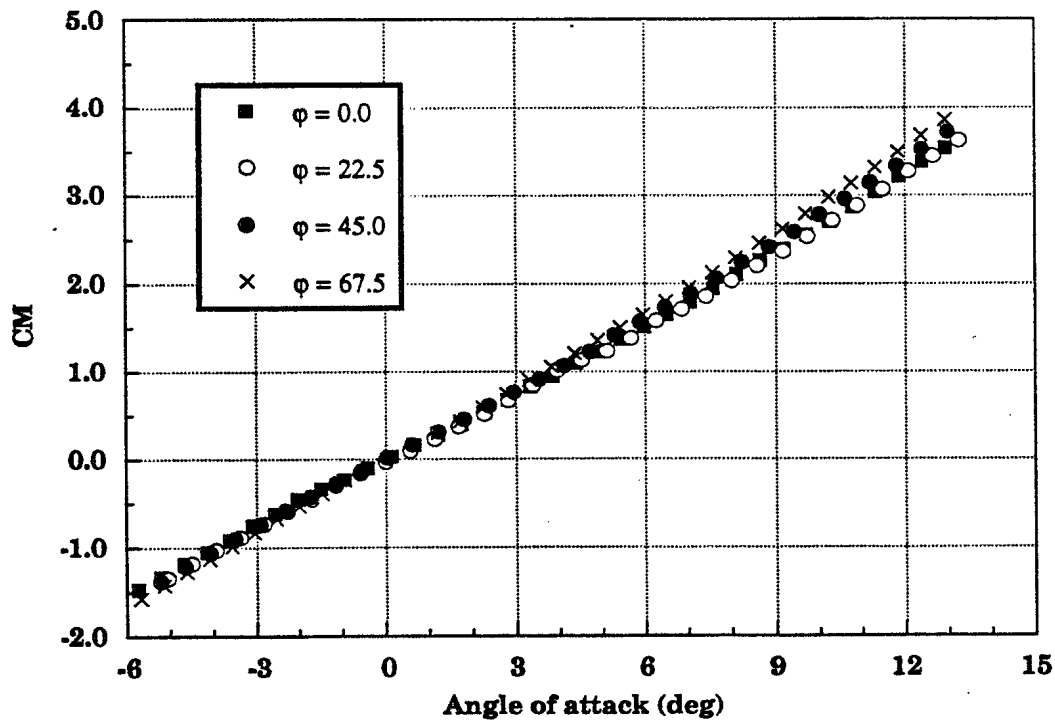


FIGURE 34 - Mach number effects on the pitching moment coefficient  
(Model B)

a)  $\phi = 0^\circ$

b)  $\phi = 45^\circ$

UNCLASSIFIED

a)  $M = 2.0$ b)  $M = 3.0$ 

UNCLASSIFIED

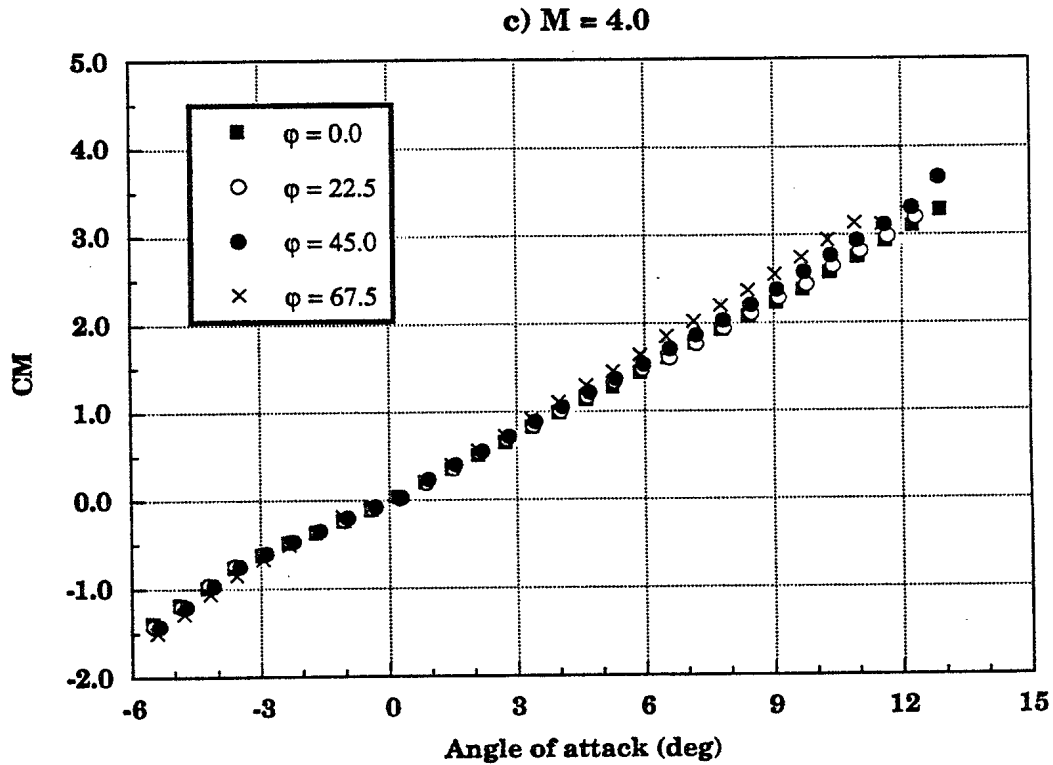


FIGURE 35 - Roll angle effects on the pitching moment coefficient (Model B)

a)  $M = 2.0$ b)  $M = 3.0$ c)  $M = 4.0$

UNCLASSIFIED

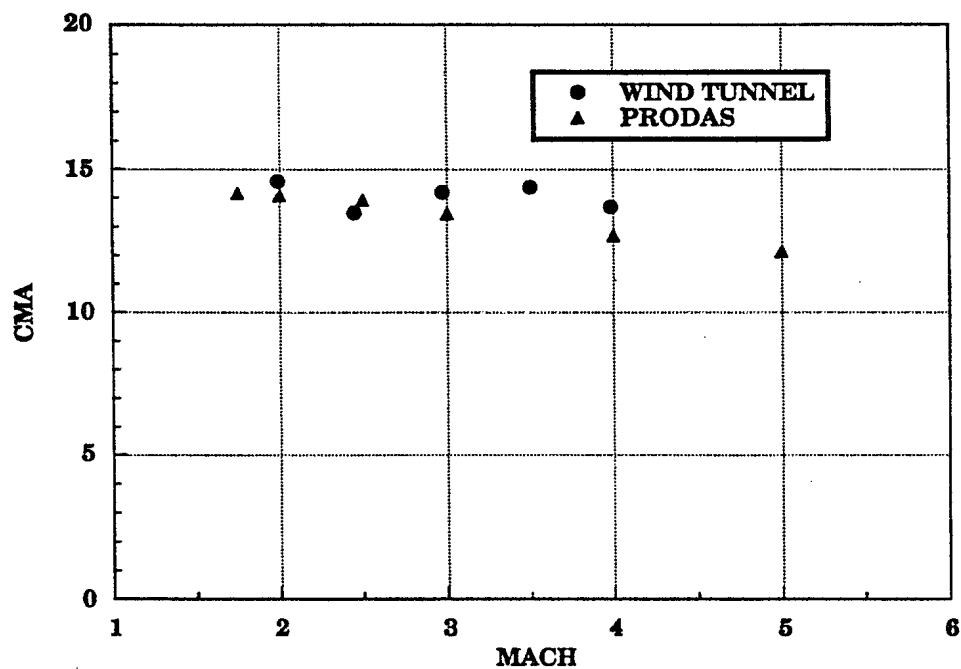


FIGURE 36 - Pitching moment coefficient slope vs. Mach number (Model B)

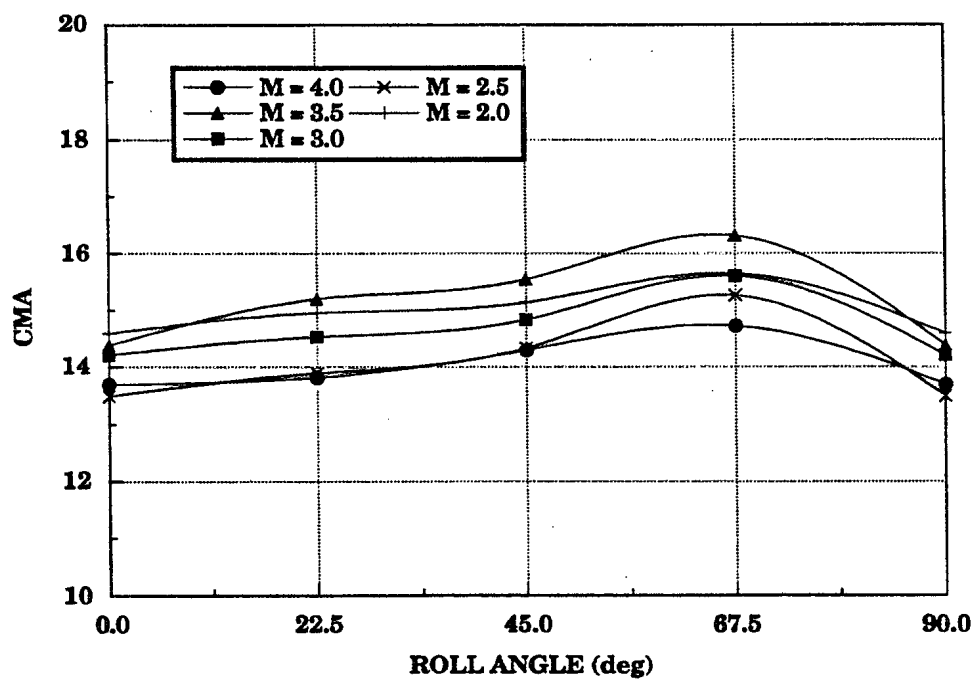


FIGURE 37 - Pitching moment coefficient slope vs. roll angle (Model B)

UNCLASSIFIED

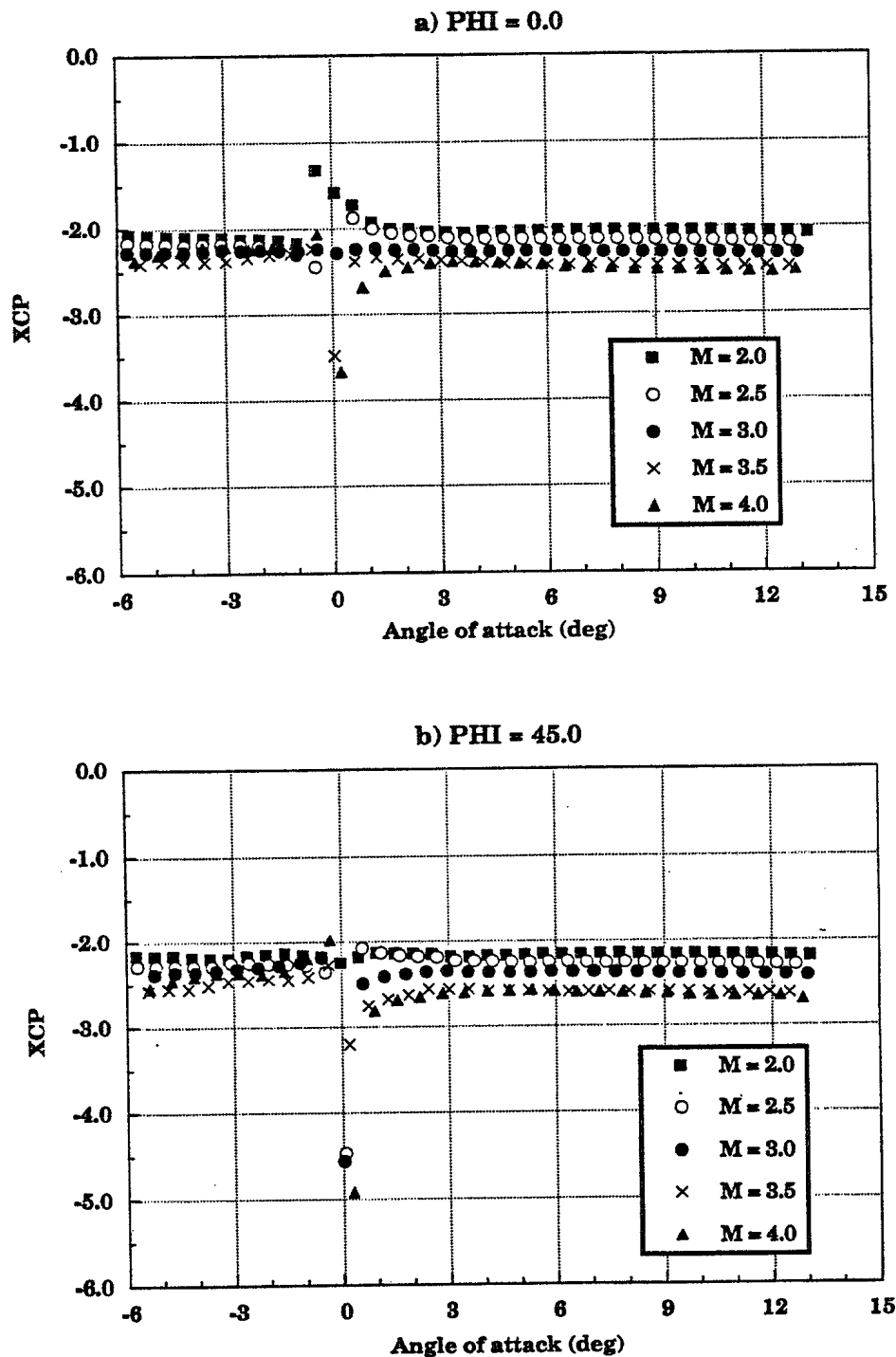


FIGURE 38 - Mach number effects on the center of pressure location  
(Model B)

a)  $\phi = 0^\circ$

b)  $\phi = 45^\circ$

UNCLASSIFIED

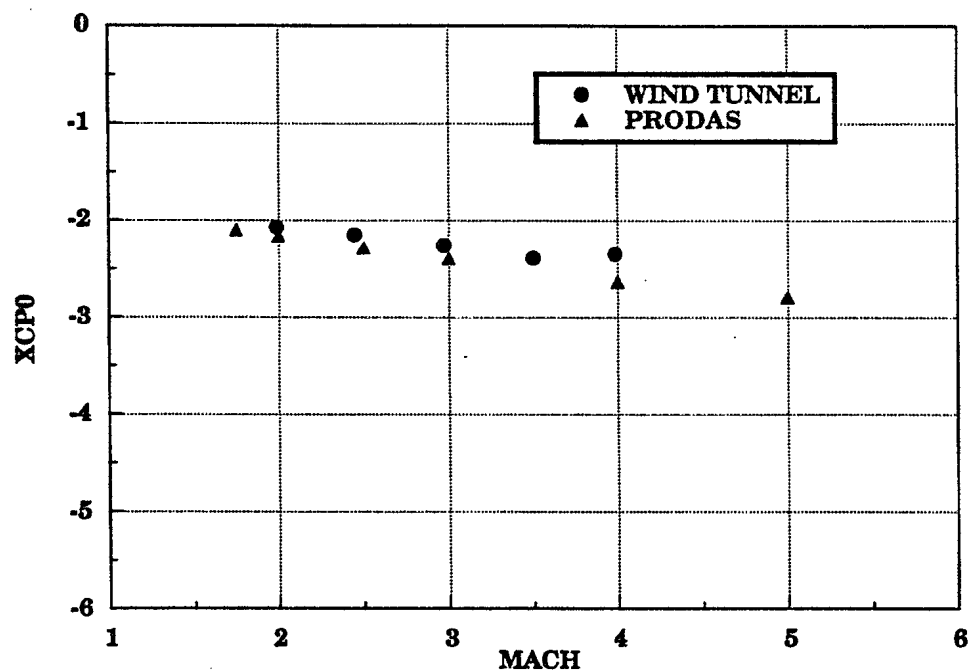


FIGURE 39 - Center of pressure location vs. Mach number (Model B)

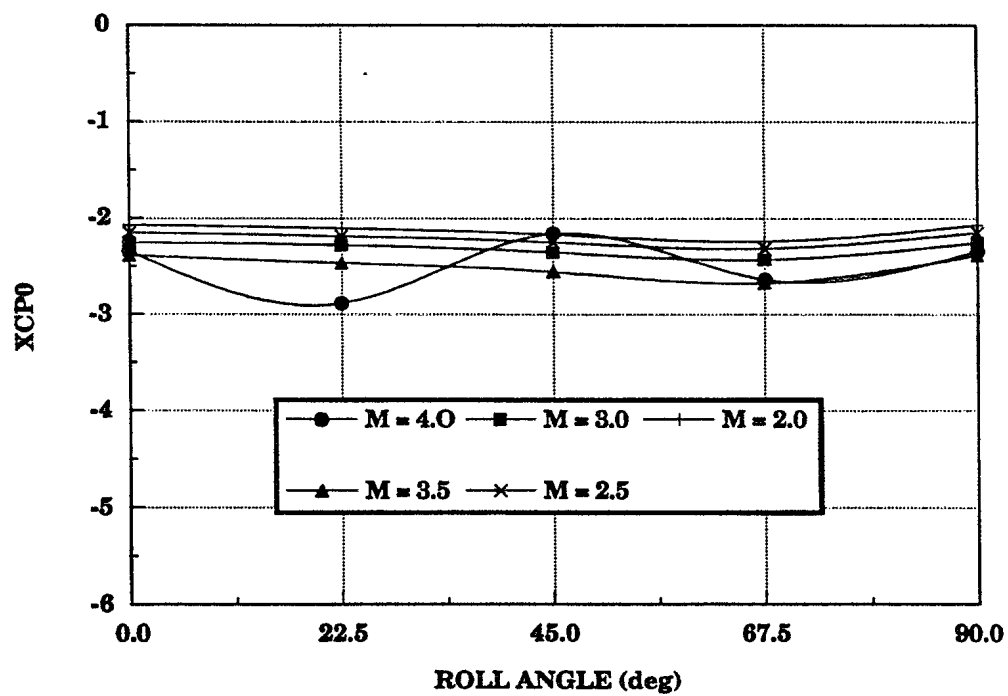


FIGURE 40 - Center of pressure location vs. roll angle (Model B)

UNCLASSIFIED

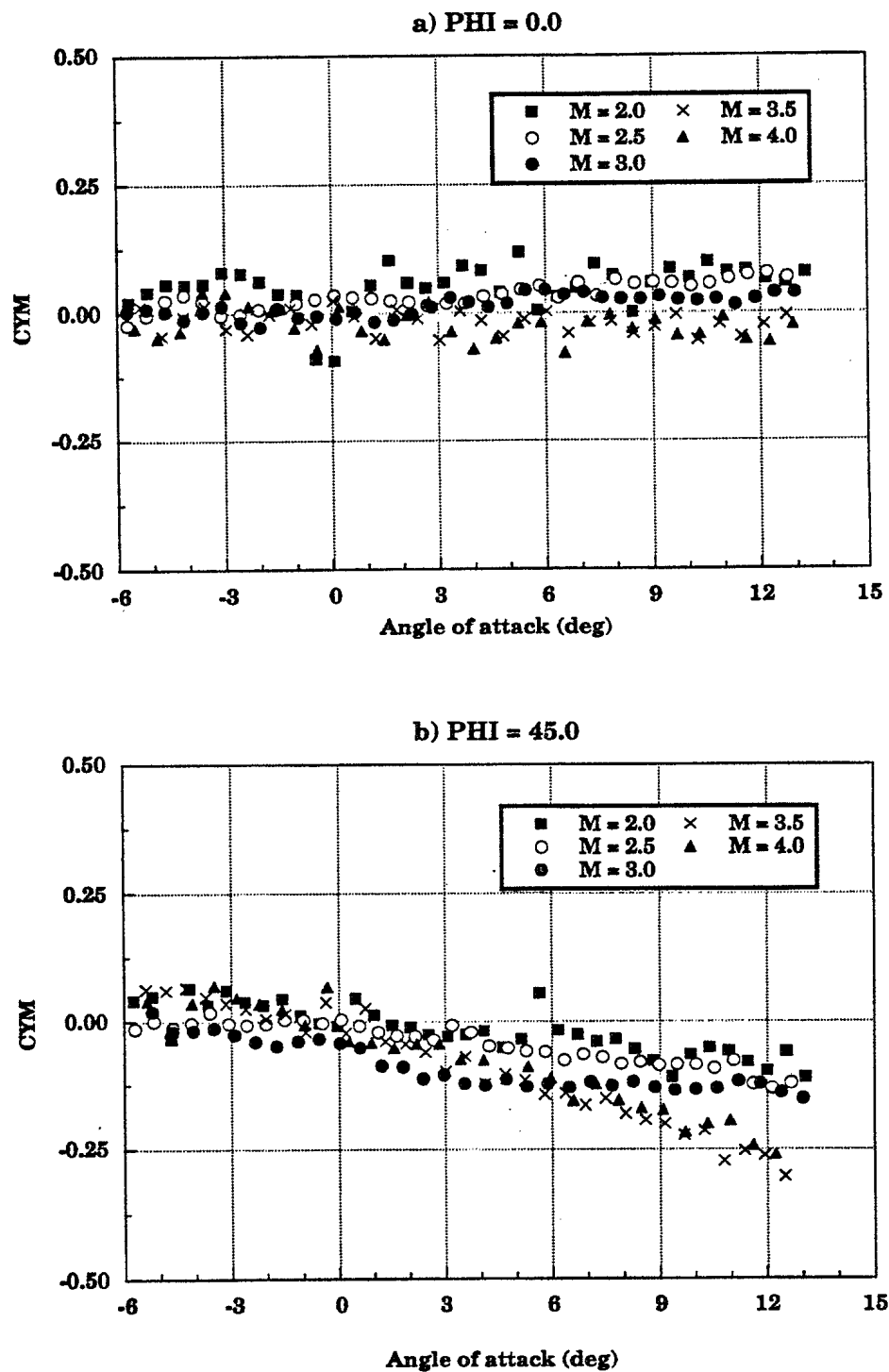
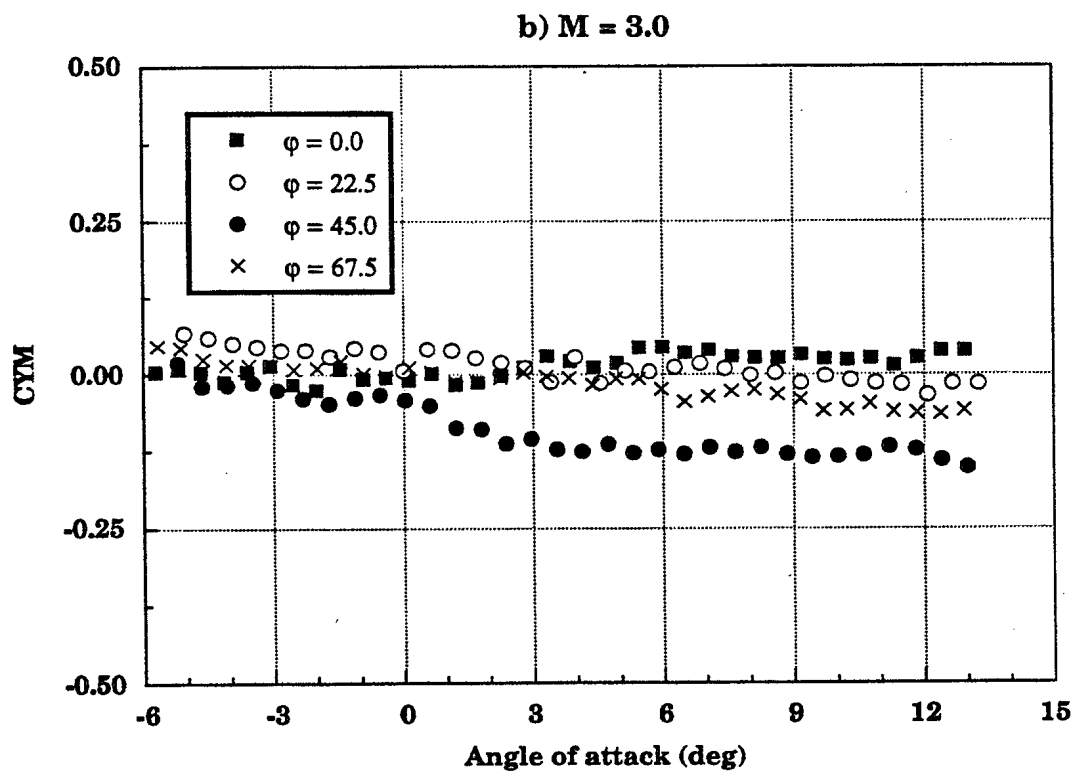
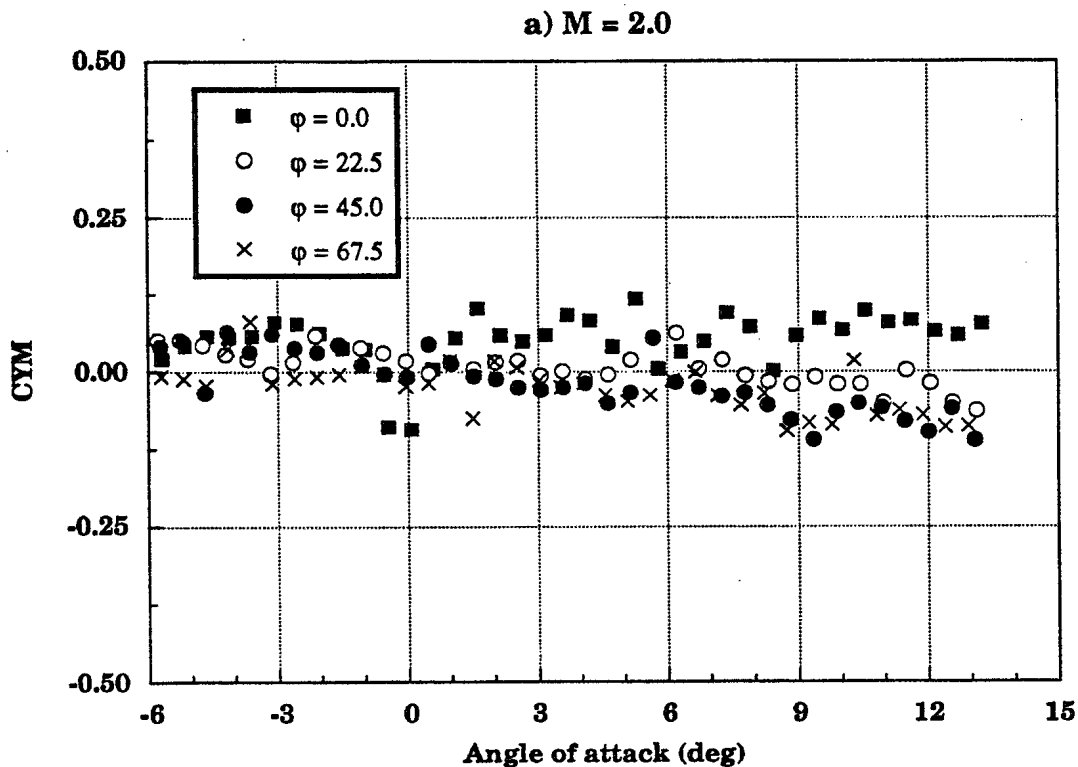


FIGURE 41 - Mach number effects on the yawing moment coefficient (Model B)

a)  $\phi = 0^\circ$

b)  $\phi = 45^\circ$

UNCLASSIFIED





UNCLASSIFIED

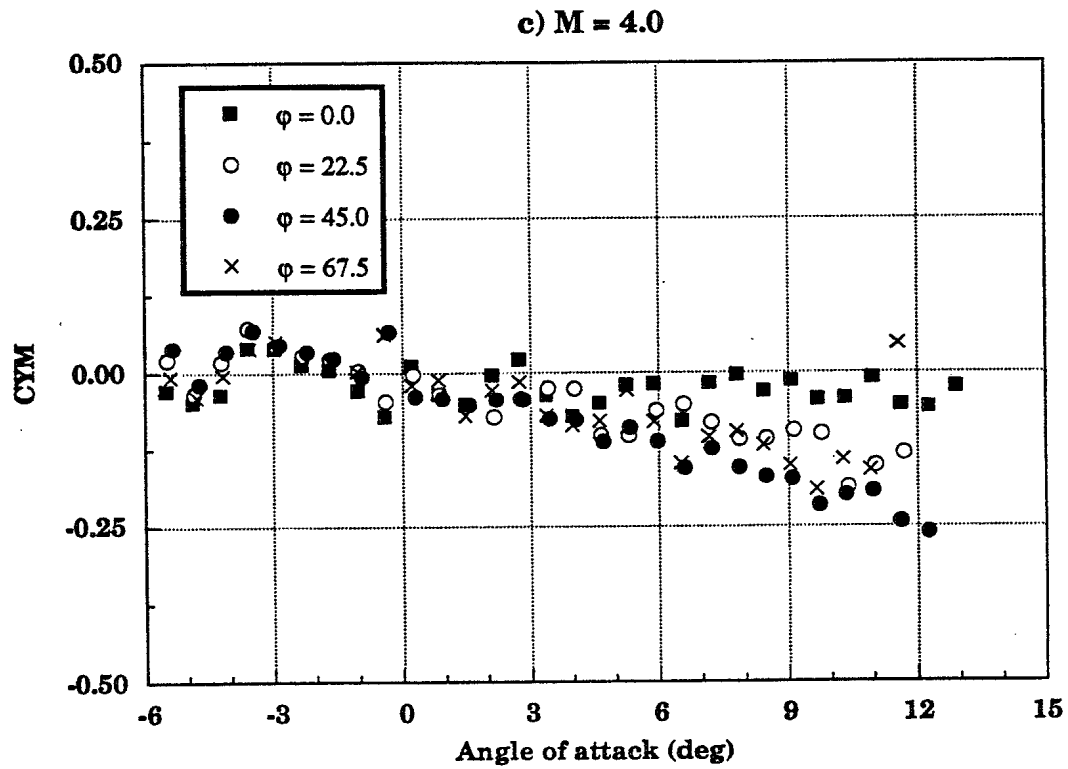


FIGURE 42 - Roll angle effects on the yawing moment coefficient (Model B)

a)  $M = 2.0$ b)  $M = 3.0$ c)  $M = 4.0$

UNCLASSIFIED

INTERNAL DISTRIBUTION

DREV R - 9520

1 - Deputy Director General  
1 - Chief Scientist  
1 - Head, Delivery Systems Section  
6 - Document Library  
1 - A. Dupuis (author)  
1 - F. Lesage  
1 - B. Girard  
1 - R. Bilodeau  
1 - É. Fournier  
1 - A. Jeffrey  
1 - J.-P. Cayouette  
1 - G. Dumas  
1 - R. Delagrave  
1 - G. Bérubé  
1 - M. Lauzon



UNCLASSIFIED

EXTERNAL DISTRIBUTION

DREV R - 9520

2 - DSIS

1 - CRAD

1 - DSAL

1 - DLR

1 - DAR

1 - DMR

1 - DSAA

1 - DSAM

1 - DFTEM

1 - DAES

1 - C. Berner (author)

1 - V. Fleck

1 - M. Giraud

Institut franco-allemand de recherches  
5, rue du Général Cassagnou  
B.P. 34  
68301 - Saint-Louis (France)

4 - Institut franco-allemand de recherches

Service de la Bibliothèque  
5, rue du Général Cassagnou  
B.P. 34  
68301 - Saint-Louis (France)

1 - G.L. Winchenbach

Weapon Flight Mechanics Division  
Wright Laboratory Armament Directorate  
Eglin AFB, FLA 32542-5434 (USA)

UNCLASSIFIED

3 - Direction des Recherches, Études et Techniques  
(DRET)

00460-ARMEES (France)

2 - Mr. J. Lutes

Les Technologies Industrielles SNC Inc.

Usine Le Gardeur

5, montée des Arsenaux

Le Gardeur, QC

J5Z 2P4

2 Bristol Aerospace Limited

P. O. Box 874

Winnipeg, Manitoba

R3C 2S4

1 - Dr. L. Chan

High Speed Aerodynamic Laboratory

Institute for Aerospace Research

National Research Council Canada

Montreal Road

Ottawa, Ontario

K1A 0R6

**UNCLASSIFIED**  
**SECURITY CLASSIFICATION OF FORM**  
(Highest classification of Title, Abstract, Keywords)

**DOCUMENT CONTROL DATA**

<b>1. ORIGINATOR (name and address)</b>  DREV	<b>2. SECURITY CLASSIFICATION</b> (Including special warning terms if applicable)  UNCLASSIFIED	
<b>3. TITLE</b> (Its classification should be indicated by the appropriate abbreviation (S,C,R or U) Wind Tunnel Investigation and Analysis of the DREV-ISL Reference Projectiles		
<b>4. AUTHORS</b> (Last name, first name, middle initial. If military, show rank, e.g. Doe, Maj. John E.)  C. Berner and A.D. Dupuis		
<b>5. DATE OF PUBLICATION</b> (month and year)  June 1996	<b>6a. NO. OF PAGES</b>  45	<b>6b. NO. OF REFERENCES</b>  11
<b>7. DESCRIPTIVE NOTES</b> (the category of the document, e.g. technical report, technical note or memorandum. Give the inclusive dates when a specific reporting period is covered.)  Technical Report		
<b>8. SPONSORING ACTIVITY</b> (name and address)  DREV		
<b>9a. PROJECT OR GRANT NO.</b> (Please specify whether project or grant)  O2E01-14	<b>9b. CONTRACT NO.</b>	
<b>10a. ORIGINATOR'S DOCUMENT NUMBER</b>  DREV R-9520	<b>10b. OTHER DOCUMENT NOS.</b>  N/A	
<b>11. DOCUMENT AVAILABILITY</b> (any limitations on further dissemination of the document, other than those imposed by security classification) <input checked="checked" type="checkbox"/> Unlimited distribution <input type="checkbox"/> Contractors in approved countries (specify) <input type="checkbox"/> Canadian contractors (with need-to-know) <input type="checkbox"/> Government (with need-to-know) <input type="checkbox"/> Defence departments <input type="checkbox"/> Other (please specify) :		
<b>12. DOCUMENT ANNOUNCEMENT</b> (any limitation to the bibliographic announcement of this document. This will normally correspond to the Document Availability (11). However, where further distribution (beyond the audience specified in 11) is possible, a wider announcement audience may be selected.)		

**UNCLASSIFIED**  
**SECURITY CLASSIFICATION OF FORM**

13. **ABSTRACT** ( a brief and factual summary of the document. It may also appear elsewhere in the body of the document itself. It is highly desirable that the abstract of classified documents be unclassified. Each paragraph of the abstract shall begin with an indication of the security classification of the information in the paragraph (unless the document itself is unclassified) represented as (S), (C), (R), or (U). It is not necessary to include here abstracts in both official languages unless the text is bilingual).

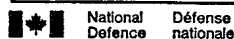
A comprehensive Wind Tunnel Investigation on a cone-cylinder body with and without fins was conducted over a Mach number range of 2 to 4. The experimental programme consisted of flow visualization, aerodynamic force and moments, static pressure and flow velocity measurements taken in the DREV Indraft Wind Tunnel. The tests were conducted as a function of angle of attack varying from -5 to +15 at different roll orientations. The wind tunnel had an upstream sting support system to conduct interference-free base pressure measurements. The surface and base pressure results are compared with similar tests that were conducted at the French-German Research Institute of Saint Louis (ISL), and the reduced aerodynamic coefficients are compared with estimated values from Projectile Design and Analysis System (PRODAS). Some differences were noticed between the results from the two wind tunnels and most of these were accounted for from the different boundary layer thicknesses.

14. **KEYWORDS, DESCRIPTORS or IDENTIFIERS** (technically meaningful terms or short phrases that characterize a document and could be helpful in cataloguing the document. They should be selected so that no security classification is required. Identifiers, such as equipment model designation, trade name, military project code name, geographic location may also be included. If possible keywords should be selected from a published thesaurus. e.g. Thesaurus of Engineering and Scientific Terms (TEST) and that thesaurus-identified. If it is not possible to select indexing terms which are Unclassified, the classification of each could be indicated as with the title.)

**WIND TUNNEL TESTS**  
**AERODYNAMIC COEFFICIENTS**  
**BASE PRESSURE**  
**SURFACE PRESSURE**  
**CONE-CYLINDER**  
**FINNED PROJECTILE**  
**BOUNDARY LAYER PROFILES**  
**UPSTREAM STING SUPPORT**  
**SUPERSONIC**

*\*498485*

NO. OF COPIES NOMBRE DE COPIES <i>1</i>	COPY NO. COPIE N° <i>1</i>	INFORMATION SCIENTIST'S INITIALS INITIALES DE L'AGENT D'INFORMATION SCIENTIFIQUE <i>JC</i>
ACQUISITION ROUTE FOURNI PAR <i>► DREV</i>		
DATE <i>► 28 May 1996</i>		
DSIS ACCESSION NO. NUMÉRO DSIS <i>►</i>		



**PLEASE RETURN THIS DOCUMENT TO THE FOLLOWING ADDRESS:** **PRIÈRE DE RETOURNER CE DOCUMENT À L'ADRESSE SUIVANTE:**

**DIRECTOR**  
**SCIENTIFIC INFORMATION SERVICES**  
**NATIONAL DEFENCE**  
**HEADQUARTERS**  
**OTTAWA, ONT. - CANADA K1A 0K2**

**DIRECTEUR**  
**SERVICES D'INFORMATION SCIENTIFIQUES**  
**QUARTIER GÉNÉRAL**  
**DE LA DÉFENSE NATIONALE**  
**OTTAWA, ONT. - CANADA K1A 0K2**